Microstructure Tailoring of Copper for Mild Tribological Conditions

Zur Erlangung des akademischen Grades einer

DOKTORIN DER INGENIEURWISSENSCHAFTEN (DR.-ING.)

von der KIT-Fakultät für Maschinenbau des
Karlsruher Instituts für Technologie (KIT)
angenommene

DISSERTATION

von

M. Sc. Roxane Lung

Tag der mündlichen Prüfung: 17.03.2026

Hauptreferent: Prof. Dr. rer. nat. Christian Greiner
Korreferent: apl. Prof. Dr.-Ing. Karl Günter Schell

Acknowledgment

I would like to express my deepest gratitude to those who have supported me throughout the course of this work.

First and foremost, I would like to thank my doctoral supervisor, Prof. Dr. Christian Greiner, for his unwavering belief in me and for giving me the opportunity to explore new ideas, which ultimately allowed me to find the focus of this work. His guidance and encouragement during challenging times were invaluable, and I am deeply grateful for the trust he placed in me. He always knew exactly when to step in and when to let me work independently, which gave me the opportunity to grow both personally and professionally. Thank you for the numerous insightful discussions we had and for the inspiring ideas. I also learned a lot through trial presentations and feedback on my manuscripts, and I deeply appreciate these unique opportunities that have contributed to my development.

I would like to thank Prof. Dr. Günter Schell for taking on the role of co-referee and for his great willingness to help me throughout my research. I am grateful to him for the fabrication of the FAST samples and for always offering his support when needed. His expert knowledge in the FAST process was invaluable and played an important role in the success of my work. I also greatly appreciate the discussions we had, which were very valuable for reflecting on the mechanisms underlying my results.

A special thank you goes to Dr. Iwiza Tesari for playing a crucial role in fabricating the GNG samples and for manufacturing the tools necessary for the process. I truly appreciate his patience during the demanding optimization of the SMGT process, as well as his valuable knowledge and creative problem-solving.

A big thank you goes to Dr. Johannes Schneider and Dr. Julia Rau for their thorough proofreading of my dissertation. Their constructive feedback was essential in refining my work.

I would like to extend my thanks to my colleagues Malte Flachmann, Dr. Antje Dollmann, Jonas Franke, and Dr. Yulong Li for the many engaging scientific discussions. Their expertise

and insights greatly supported me in the development of this work. Furthermore, I would like to express my gratitude to Dr. Amod Kashyap for his support during my exchange in India.

My sincere thanks go to all current and former colleagues of the tribology groups at IAM-ZM, especially Bonita Beichert, Olga Horvat, Carlos Barrera, Ines Kisch, Amelie Schiele, Zheng Zhong, and Jianjun Long for the fun work breaks during which we did plank sessions and played football, as well as for the enjoyable moments we shared during lunch breaks and after-work gatherings, which made me feel truly comfortable in the group.

Finally, I would like to thank my family and friends for always being there for me during my PhD journey, especially Alex, who has always supported me, for example through numerous snack surprise packages that seemed to appear out of nowhere during those late nights of research.

Abstract

Tribology plays an essential role in the performance and durability of components in relative motion, with material microstructures significantly affecting friction and wear. Although copper is widely used in industry for its thermal and electrical conductivity, a deeper understanding of its tribological behavior is essential to broaden its application in tribology-related fields. Such knowledge is crucial to optimize friction and wear, thereby promoting sustainability. In particular, the tribological performance of gradient nano-grained copper and porous copper under mild tribological loading conditions remains unexplored. This study hypothesized that gradient nano-grained structures have a greater effect on the tribological behavior of copper under mild loading conditions, especially in reducing the coefficient of friction, compared to porous copper. Samples with varying gradient structures and different porosities were tested under identical tribological conditions and characterized by density, hardness, surface, and microstructural analyses.

While previous investigations showed that gradient nano-grained copper reduces friction under severe tribological loading conditions, in this study, under mild dry conditions, they exhibited a high coefficient of friction regardless of gradient thickness or surface grain size. Tribological performance was mainly influenced by sliding speed and test duration, with longer tests and lower speeds increasing tribo-oxidation, plastic deformation at the surface, surface grain coarsening and roughening, and friction. If, however, the applied load was insufficient to distribute stress through the gradient layer, behavior resembled that of nano-grained copper, with tribo-oxidation inhibiting the formation of friction-reducing ultrafine-grained surface layers.

In contrast, copper with a porosity of 15 % reduced the coefficient of friction by more than 50 % compared to copper with a low porosity of around 4 % as well as gradient nano-grained copper samples. Low-porosity specimens showed extensive subsurface deformation, tribo-oxidation, cracking, delamination, and pile-ups. Conversely, high-porosity samples exhibited limited subsurface deformation and tribo-oxidation due to a reduced depth of high-stress regions within the material, a slightly larger real contact area, and reduced Hertzian contact pressure caused by the porosity-induced decrease in effective Young’s modulus. Regarding pore size, specimens with small pores exhibited less pronounced topographical deformation

and tribo-oxidation at both high and low porosity levels. Long-term tests confirmed stable low friction for high-porosity samples, whereas low-porosity ones showed progressive damage. Surface treatments also influenced tribological behavior: compared to vibropolished samples, electropolishing increased roughness and localized stresses, leading to greater deformation, tribo-oxidation, cracking, delamination and higher friction. These findings disprove the initial hypothesis, demonstrating that porosity plays a dominant role in influencing the tribological behavior and reducing friction under mild tribological loading conditions.

Kurzfassung

Tribologie spielt eine zentrale Rolle für die Leistungsfähigkeit und Lebensdauer von Bauteilen in Relativbewegung, wobei die Mikrostruktur des Werkstoffs maßgeblich Reibung und Verschleiß beeinflusst. Obwohl Kupfer aufgrund seiner hohen thermischen und elektrischen Leitfähigkeit in der Industrie weit verbreitet ist, ist ein tiefergehendes Verständnis seines tribologischen Verhaltens erforderlich, um sein Anwendungspotenzial in tribologischen Bereichen zu erweitern. Solches Wissen ist entscheidend, um Reibung und Verschleiß zu optimieren und damit zur Nachhaltigkeit beizutragen. Insbesondere das tribologische Verhalten von nanokristallinen Korngrößengradienten sowie von Porosität in Kupfer unter milden tribologischen Bedingungen ist bislang kaum untersucht. Ein fundiertes Verständnis dieser Systeme ist entscheidend, um Reibung und Verschleiß zu optimieren und damit nachhaltige Anwendungen zu fördern. Im Rahmen dieser Studie wurde die Hypothese formuliert, dass Strukturen mit nanokristallinen Korngrößengradienten unter milden Belastungsbedingungen einen stärkeren Einfluss auf das tribologische Verhalten von Kupfer ausüben und insbesondere den Reibungskoeffizienten stärker reduzieren im Vergleich zu porösem Kupfer. Für die Untersuchungen wurden Proben mit variierenden Korngrößengradienten sowie mit unterschiedlicher Porosität unter identischen tribologischen Prüfbedingungen getestet und anhand von Dichte-, Härte-, Oberflächen- und Mikrostrukturanalysen charakterisiert.

Während frühere Untersuchungen zeigten, dass nanokristalline Korngrößengradienten in Kupfer unter extremen tribologischen Belastungsbedingungen die Reibung reduzieren, wiesen die Proben in dieser Studie unter milden Beanspruchungsbedingungen einen hohen Reibungskoeffizienten auf, unabhängig von der Schichtdicke der Gradienten oder der Oberflächenkorngrößen. Das tribologische Verhalten wurde hauptsächlich von der Gleitgeschwindigkeit und der Testdauer beeinflusst, wobei längere Tests und niedrigere Gleitgeschwindigkeiten zu verstärkter Tribooxidation, plastischer Deformation an der Oberfläche, Kornvergröberung, Oberflächenrauheit und erhöhter Reibung führten. Falls die aufgebrachte Last jedoch unzureichend war, um die Spannung über die Korngrößengradienten zu verteilen, ähnelte das Verhalten dem von nanokörnigem Kupfer, wobei die Tribooxidation die Bildung reibungsreduzierender ultrafeinkörniger Oberflächenschichten hemmte.

Im Gegensatz dazu reduzierte Kupfer mit einer Porosität von 15 % den Reibungskoeffizienten um mehr als 50 % im Vergleich zu Kupfer mit einer geringen Porosität von etwa 4 % sowie zu Kupferproben mit nanokristallinen Korngrößengradienten. Proben mit geringer Porosität zeigten ausgeprägte plastische Verformungen unterhalb der Oberfläche, Tribooxidation, Rissbildung, Delamination und Materialanhäufungen. Proben mit hoher Porosität hingegen wiesen nur geringe Tribooxidation und plastische Verformungen unterhalb der Oberfläche auf, was auf die geringere Tiefe der Bereiche hoher Spannungen im Material, die etwas größere reale Kontaktfläche sowie die reduzierte Hertzsche Kontaktpressung infolge der porositätsbedingten Verringerung des effektiven E-Moduls zurückgeführt werden kann. Hinsichtlich der Porengröße zeigten Proben mit kleinen Poren sowohl bei hohem als auch bei niedrigem Porositätsgrad eine geringere topographische Deformation sowie eine weniger ausgeprägte Tribooxidation. Langzeittests bestätigten einen stabil niedrigen Reibungskoeffizienten bei hochporösen Proben, wohingegen Proben mit geringer Porosität zunehmende Schäden zeigten. Auch Oberflächenbehandlungen beeinflussten das tribologische Verhalten: im Vergleich zu vibropolierten Proben erhöhte das Elektropolieren die Rauheit und lokale Spannungskonzentrationen, was zu stärkerer Verformung, Tribooxidation, Rissbildung, Delamination und höherer Reibung führte. Diese Ergebnisse widerlegen die Anfangshypothese und zeigen, dass die Porosität unter milden tribologischen Belastungsbedingungen eine dominierende Rolle bei der Beeinflussung des tribologischen Verhaltens und insbesondere der Reibungsreduzierung darstellt.

Publications

Parts of the present study have already been submitted in the following publications:

Roxane Lung, Karl Günter Schell, Christian Greiner, **Porosity Matters: Exploring its Impact on the Unlubricated Tribological Behavior of Copper**, under review (2025). DOI: 10.35097/q9q7nbnb7ggazf4m.

Roxane Lung, Karl Günter Schell, Christian Greiner, **How Surface Treatment of Porous Copper Samples Dictates Dry Friction and Wear**, Materials & Design (2025), 114584. DOI: 10.1016/j.matdes.2025.114584.

Table of Contents

List of Abbreviations

GNG	Gradient nano-grained
SEM	Scanning electron microscopy
SMGT	Surface mechanical grinding treatment
FAST	Field assisted sintering technology
CIP	Cold isostatic pressing
CG	Coarse-grained
WC-Co	Tungsten carbide-cobalt
DC	Direct current
Cu	Copper
DTL	Dislocation trace line
SAGB	Small angle grain boundary
Cu_2O	Cuprous oxide
CuO	Cupric oxide
DRX	Dynamic recrystallization
NG	Nano-grained
MML	Mechanically mixed layer
FSP	Few small sintering pores
MSP	Many small sintering pores
FBP	Few big sintering pores
FSPC	Cold-isostatically pressed sample with few small sintering pores
FBPC	Cold-isostatically pressed sample with few big sintering pores
MBP	Many big sintering pores
ND	Normal direction
SD	Sliding direction
TD	Transversal direction
FIB	Focused ion beam
EBSD	Electron backscatter diffraction
BSE	Backscattered electrons
vp	Vibropolished

ep	Electropolished
CP	Circular patterns
HPT	High-pressure torsion

List of Symbols

Ra	[m]	Arithmetic mean surface roughness from profile measurement
P	[W]	Joule heating power
I	[A]	Electric current
R	[Ω]	Electrical resistance
T_m	[°C]	Melting temperature
F_R	[N]	Friction force
F_N	[N]	Normal load
μ	[-]	Coefficient of friction
A_R	[m^2]	Real contact area
s	[N]	Force required to shear off metallic junctions
F_{adh}	[N]	Adhesive component of the friction force
$m_{s(A)}$	[kg]	Specimen mass in air
$m_{s(W)}$	[kg]	Specimen mass in deionized water
ρ_W	[kg m^{-3}]	Water density
ρ_A	[kg m^{-3}]	Air density
l_e	[m]	Evaluation length of the roughness measurement profile
$z(x)$	[m]	Surface height values at position (x) within the measurement profile
Sa	[m]	Arithmetic mean surface roughness from area measurement
A	[m^2]	Evaluation area of the roughness measurement
$z(x,y)$	[m]	Surface height values at position (x,y) within the measurement area
p	[N m^{-2}]	Indentation hardness
μ_P	[-]	Plowing contribution of the coefficient of friction
F_P	[N]	Plowing friction force
ρ_a	[N m^{-2}]	Mean contact pressure
A_{SD}	[m^2]	Projected area in sliding direction
A_{ND}	[m^2]	Projected area in normal direction
p_N	[N m^{-2}]	Nominal pressure
v	[m s^{-1}]	Sliding speed

1 Motivation

Tribology is omnipresent, extending from micro- and nanotechnological systems, such as micro- and nano-electromechanical systems to macro-scale engineering in machines and technical systems including body joints, gas turbine engines in the aerospace industry, as well as brakes and clutches in the automotive industry [1–4]. While in macroscopic sliding contacts millions of asperities interact with each other, in microtribology only a few asperities are in contact [2]. On the nanoscale, on the other hand, each individual asperity represents the contact. Tribology affects numerous sectors including automotive engines and brake systems, aerospace jet engines, energy wind turbines, and biomedical applications such as prosthetics. Approximately 23 % of global energy consumption is attributable to tribological losses, with 20 % spent to overcome friction [5]. About 70 % of device failures stem from lubricant failure and wear [6]. Optimizing tribological systems, such as in vehicles and machines, could reduce energy consumption by up to 8 %. With regard to climate change, such improvements are crucial. Reducing frictional losses in Germany alone could save around 208 Mt of carbon dioxide, corresponding to 60 % of the country's greenhouse gas emission reduction target for 2030 [7]. Fundamental knowledge is essential to optimize tribological systems in order to extend service life, enable maintenance-free operation, increase the rotational speed of components, and improve efficiency [1]. Copper and its alloys, with its high thermal and electrical conductivity, is a promising material for components in relative motion including bearings, seals, sliding elements, electrical contacts, and heat exchangers involving moving components [8–10].

Tribological performance strongly depends on material properties. Accordingly, this study systematically investigates the effects of grain size, particularly gradient nano-grained (GNG) microstructures and porosity. The tribological behavior is analyzed under mild tribological loading conditions, consistent with prior studies focused on fundamental mechanisms [11]. These results contribute to a better understanding of complex microstructures. The analysis in this study includes wear track characterization using surface profilometry and light microscopy, as well as microstructural examination by exposing the microstructure with a

focused ion beam (FIB), followed by subsequent scanning electron microscopy (SEM) imaging.

Prior research shows that GNG structures substantially reduce friction and wear loss under severe tribological loading conditions (high sliding speeds and elevated loads) as well as at short stroke lengths [12–15]. This study explores whether GNG structures similarly influence friction and wear under mild tribological loading conditions and at longer strokes, and if these tribological effects depend on GNG layer depth or surface grain size. GNG microstructures are produced via surface mechanical grinding treatment (SMGT) and tribologically tested after surface post-treatments.

Porosity is investigated due to its growing relevance in applications that require low weight, high conductivity, and reliable tribological performance, used especially in aerospace, automotive, and railway industries [16, 17]. Reduced mass enables material savings and improves energy efficiency, lowering fuel consumption and emissions [18, 19]. Though often unavoidable in processes such as additive manufacturing and sintering, porosity is usually minimized, as it can degrade mechanical and physical properties such as thermal and electrical conductivity [20–24]. Previous studies indicate that the tribological effect of porosity is material-dependent: it improves wear resistance in stainless steel, but increases both wear and friction in aluminum and its alloy 6061 [25, 26]. Its effect under lubrication also varies with material pairing, making generalizations difficult [27]. To date, no studies have addressed the tribological behavior of porous copper under dry mild sliding conditions, emphasizing the relevance of this work. If porosity proves beneficial, post-treatment to remove it could be omitted, potentially enabling further energy savings [28]. Therefore, porous copper specimens are produced using the field assisted sintering technology (FAST) with varying porosity and pore sizes. Some specimens are subsequently subjected to an additional cold isostatic pressing (CIP) step. The influence of pore size and porosity on tribo-oxidation, grain refinement, and wear mechanisms is analyzed. Long-term performance is assessed by significantly increasing sliding cycles. The study also evaluates how surface finishing methods, specifically chemical-mechanical vibropolishing and electropolishing, affect friction and wear behavior of porous copper samples.

2 State of the Art

2.1 Microstructure Tailoring Processes

There are various approaches to modify the microstructure of metals. This work focuses on a surface treatment through severe plastic deformation inducing grain size gradients, as well as on the fabrication of porous components by sintering.

2.1.1 Surface Mechanical Grinding Treatment (SMGT)

The copper substrate used for the SMGT process is first annealed to produce a homogeneous coarse-grained (CG) microstructure [12, 29]. Subsequently, the surface of the copper specimen is subjected to SMGT, as illustrated in Figure 2.1. To avoid annealing during the process, it is carried out under cryogenic conditions using liquid nitrogen. Multiple sliding passes are applied using a tungsten carbide-cobalt (WC-Co) sphere, with each pass increasing the indentation depth by 40 µm, resulting in a total depth of 240 µm. This procedure leads to the formation of a gradient nano-grained microstructure, as shown in Figure 2.2, and an average surface roughness *Ra* of around 0.2 µm. The top surface of the SMGT-processed copper rod contains no detectable tungsten, and carbon was limited to the outermost 24 nm [30]. These findings suggest that surface contamination from the sliding sphere is minimal, likely due to the suppression of elemental interdiffusion by the cryogenic processing temperatures. During the plastic deformation prevailing under these conditions of high strain rates and low temperatures, deformation twinning plays a major role in achieving nanometer-scale grain refinement [30]. A hardness gradient with respect to depth is evident, ranging from 1.8 GPa at the surface to 1.1 GPa at 150 µm depth, and decreasing to 0.75 GPa in the coarse-grained region [12, 14]. This reduction in hardness is consistent with the observed structural coarsening, in accordance with the Hall-Petch relationship.

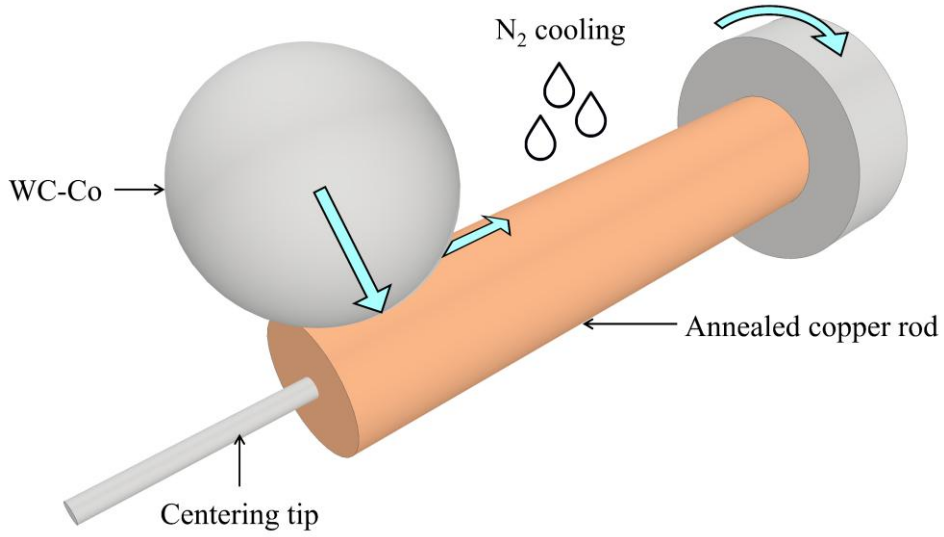

Figure 2.1: Illustration of SMGT according to Chen et al. [12, 29]: A copper rod undergoes repeated sphere sliding with increasing indentation depth, forming a gradient nano-grained surface layer.

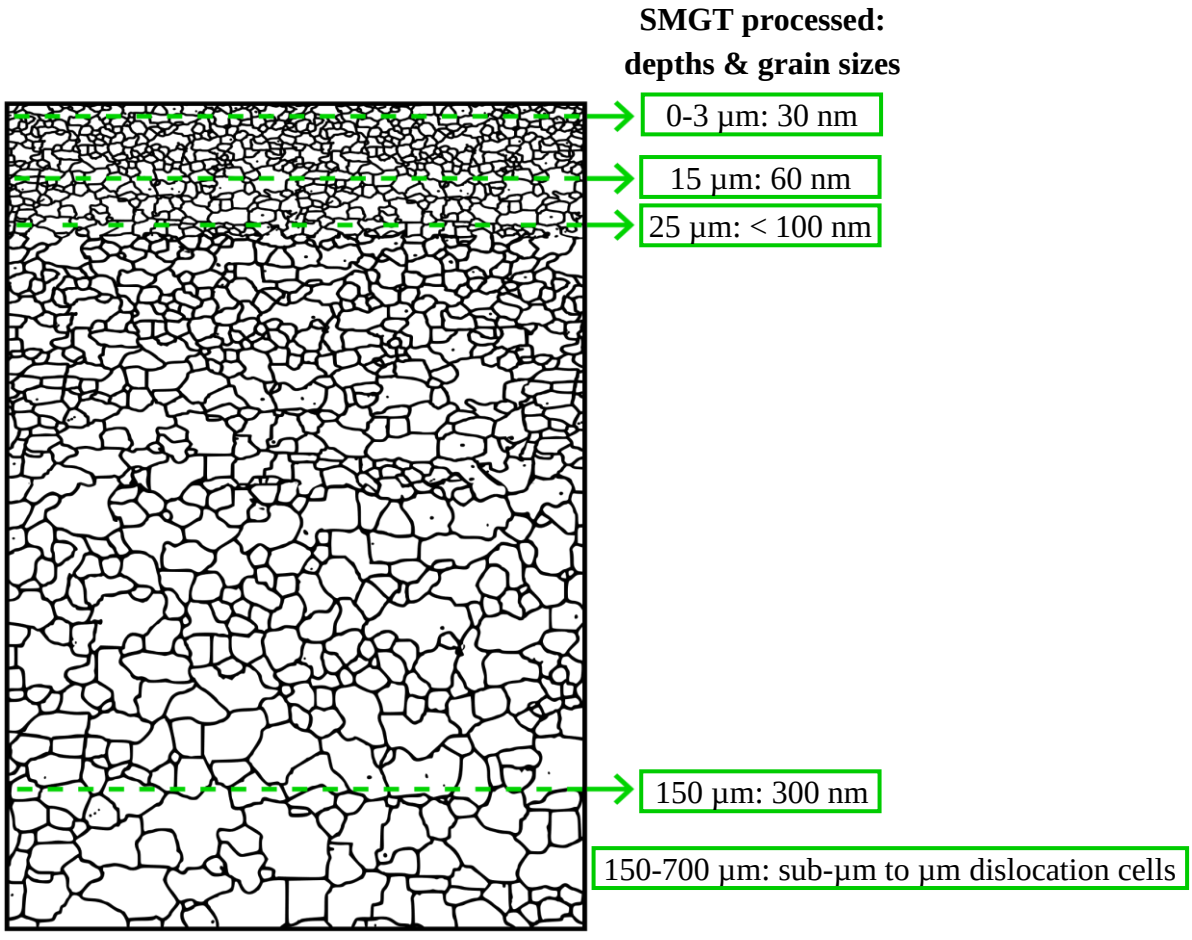

Figure 2.2: Microstructure of a SMGT-processed copper sample according to Chen et al. [12].

2.1.2 Field Assisted Sintering Technology (FAST)

FAST is a low-voltage, pulsed direct current (DC) sintering method that combines mechanical pressure with electrical current flow through the sample, generating heat by the Joule effect [22]. The setup is shown in Figure 2.3. If the green body is electrically non-conductive, heating takes place in the electrically conductive die, and the generated heat is transferred to the sample via thermal conduction. In contrast, for conductive powders, Joule heating occurs directly within the sample and the conductive tool components. In this case, sintering is not driven by heat supplied from the die; instead, as the temperature increases, heat generation occurs predominantly within the powder and the conductive punch-foil assembly. Consequently, the die does not require materials capable of maintaining mechanical strength at high temperatures, thereby overcoming one of the main challenges of conventional hot pressing [31]. Another advantage is the achievement of full density while retaining the initial grain size, at significantly lower homologous temperatures, reduced pressure, and shorter processing times compared to conventional methods [32].

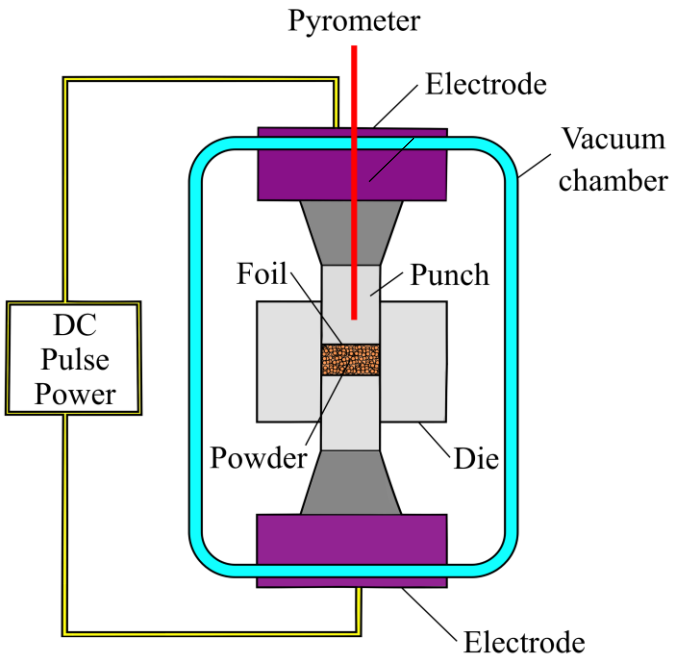

Figure 2.3: Schematic illustration of FAST adapted from [22, 32]. The powder, inserted into a die, is sintered under vacuum using Joule heating induced by electric current and uniaxial pressure applied through punches.

During the FAST process, a pulsed current is applied, causing micro-discharges at the particle contact points [22, 33]. The resulting electrical breakdown cleans the particle surfaces, thereby

reducing impurities at the grain boundaries. Pulse discharges are typically initiated using a low voltage of about 10 V in combination with a high current ranging from 600 to 1000 A [34]. DC is preferred over alternating current (AC) as it enables uniform current distribution. AC induces the skin effect, whereby the current density is concentrated near the surfaces of the particles and decreases with increasing depth. This inhomogeneous current distribution may result in uneven heating and unwanted microstructural properties in the sintered sample [35]. The temperature rise during sintering is primarily driven by Joule heating, where the power

$$P = I^2 \cdot R \qquad \text{Equation 1}$$

depends on the magnitude of the electric current I and the electrical resistance R [32, 36]. Chawake et al. [32] demonstrated that in the initial stages of sintering, the resistance to the electrical path is highest, which may be attributed to the presence of pores and the high amount of particle-particle contacts covered with thin surface oxide layers. The contact resistance between particles is further influenced by the applied pressure and particle size distribution [37]. At this stage, a resistance of $2 \cdot 10^{-2}$ Ω is observed for copper powder sintered using a graphite die and graphite punch with a height and diameter of 20 mm, along with a 0.2 mm thick graphite foil [32]. Upon exceeding 30 % of the melting temperature T_m, the electrical resistance in the current path, which arises from the punch, the foil between punch and powder, as well as from their contact points, contributes significantly to the overall resistance. As a result, at temperatures above 0.3 T_m, the amount of Joule heat generated in the graphite foils and punches is significantly higher than in the sample. This is due to the dielectric breakdown of the thin oxide layers on the particle surfaces. In the case of copper, two densification stages are observed, which are likely related to the dielectric breakdown of the CuO and Cu_2O oxide layers. Consequently, the formation of conductive paths leads to a saturation of the electrical resistance at $3 \cdot 10^{-3}$ Ω, which is almost an order of magnitude smaller than the initial resistance and is mainly determined by the resistance of the punches and the interfacial foils. With increasing density and decreasing electrical resistance of the sample, the current flowing through the die becomes minimal. While particle-particle necks begin to form at around 0.3 T_m, the neck area increases rapidly and eventually saturates at a constant value once a relative density greater than 0.65 is reached.

According to Chawake et al. [32], maximum densification of iron, nickel and copper (Cu) powders occurs at temperatures between 0.4 and 0.6 T_m. In their work, a relative density greater than 85 % was obtained by sintering at a pressure of 10 MPa, a maximum temperature of 0.7 T_m and a heating rate of 100 K min^{-1}. While the early application of pressure at low temperatures in ceramics leads to inter-particle bonding that hinders subsequent particle rearrangement, it promotes both densification and a more favorable pore shape in metals with high plasticity [38].

The temperature distribution during field assisted sintering is schematically shown in Figure 2.4. In this setup, iron powder was used together with a die, that was insulated from the powder by a ceramic liner, along with wafers between the punches and the powder [37]. The wafer selection was based on its high electrical resistivity, low thermal conductivity, and high melting point, in order to achieve a more uniform heat distribution within the sample. Despite the presence of wafers, the highest temperature occurred in the center of the sample. Without wafers, heat can directly dissipate through the punches, potentially leading to insufficient sintering at the top and bottom ends of the cylindrical sample. A lower temperature than at the sample center was also measured at the compact-liner interface, as the non-conductive liner is not heated by the electric current but instead conducts heat away from the sample [31]. Although, on the one hand, this reduction in temperature prevents the compact from reacting with the liner material during sintering, on the other hand, it may also lead to insufficient sintering of the sample edges.

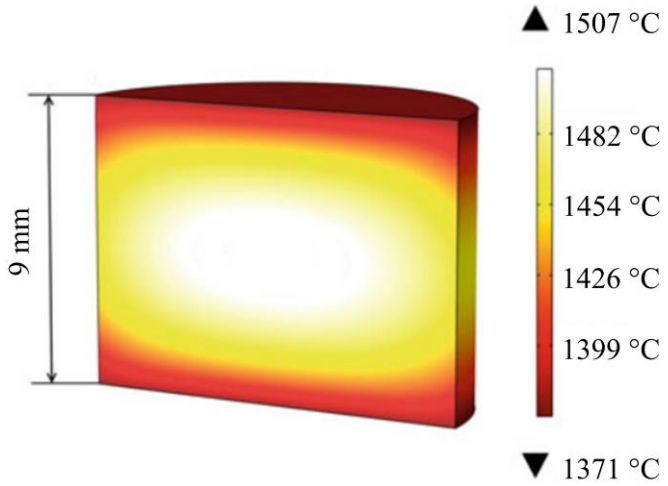

Figure 2.4: Schematic representation of the temperature distribution in a compact during the field assisted sintering of iron powder, adapted from Olevsky and Dudina [37].

2.2 Surface Treatments

In many application fields, the surface of workpieces is processed to achieve a high-quality surface finish. Both electropolishing and chemical-mechanical vibropolishing are widely used for this purpose.

2.2.1 Electropolishing

During electropolishing, the workpiece is made anodic in a usually high-viscosity concentrated acid solution, which may contain phosphoric acid [39–42]. Due to the applied voltage, a significant portion of the electric charge accumulates at the asperities of the surface roughness, causing the edges to dissolve first [43]. Electropolishing is widely used in industrial applications to achieve very smooth surfaces, due to its simplicity, and because it can be applied to complex structures [40, 44–47]. It is employed in various industries, including the food industry, medical technology, such as in stainless steel surgical devices, as well as in the semiconductor industry for optical, electrical and ultra-high vacuum components, and in the pharmaceutical industry. Additionally, it is used to remove preparation-induced deformation layers before examining specimens, such as those analyzed with electron backscatter diffraction.

2.2.2 Chemical-Mechanical Vibropolishing

During chemical-mechanical polishing, both a chemical reaction and mechanical material removal occur [48, 49]. According to Steigerwald et al. [50], clusters of atoms are first mechanically removed by abrasive particles from the specimen surface and then chemically dissolved. While an insufficient chemical polishing may cause the sample surface to be scratched again, a more intense chemical reaction can lead to both increased surface roughness and difficulty in achieving planarity. In contrast, Zhao and Lu [51] assume that the chemical reaction softens the surface, making it easier for the material to be mechanically removed by particles in the slurry. Similarly, Paik and Park [52] assume that the oxide polishing suspension, which contains abrasive colloidal silica particles, chemically reacts with the specimen's surface. Vibropolishing is described by Brust [53] as a combination of peening, burnishing, and microcutting, whereas Domblesky et al. [54] characterize it as a sequence of

randomized grinding processes. By using ultrasonic vibrations, the agglomeration of abrasive particles in the slurry can probably be prevented [55]. Chemical-mechanical polishing is considered the most effective method in the semiconductor industry for surface planarization, such as in the thinning and smoothing of thin films during the production of integrated circuits [51, 56]. Vibropolishing is used for fine finishing and deburring, among other industries, in the aviation jet engine sector to polish components, including turbine and fan blades, as well as blisks, to reduce fuel consumption and lower costs [57].

2.3 Tribology

The study of interacting solid surfaces in relative motion, which includes friction, lubrication and wear, is known as tribology, a term derived from the Greek word *tribos* meaning "rubbing" [3, 58]. As an interdisciplinary field, tribology draws on knowledge from materials science, chemistry, physics, engineering, and computational science, among others [3]. Tribological properties result from the interaction between the elements of a tribo-system, comprising a body, a counterbody, a surrounding medium, and an optional interfacial element, as well as the applied load spectrum and the environmental conditions [1, 59]. Tribological research aims to minimize or eliminate losses caused by friction and wear, thereby improving system efficiency, performance, reliability, and cost-effectiveness [3].

2.3.1 Friction

The mechanical resistance acting tangentially at the interface between two contacting bodies and opposing their relative motion is known as friction. According to Amonton's second law, the friction force

$$F_R = \mu \cdot F_N \qquad \text{Equation 2}$$

is directly proportional to the applied normal load F_N, with the proportionality factor μ corresponding to the dimensionless coefficient of friction [60]. Subsequently, Coulomb demonstrated that this proportional relationship applies to both static and sliding friction. Bowden and Tabor [60] assumed that the frictional force consists of two components: adhesion and deformation. Due to adhesion, resulting in cold welding, junctions form in the

real contact area A_R between the specimen and the counterbody. When the counterbody slides over the specimen's surface, a certain force *s*, acting tangentially to the interface, is required to shear off these metallic junctions, so that according to Amonton's first law, the adhesive component of the friction force can be expressed as [60]:

$$F_{adh} = A_R \cdot s \qquad \text{Equation 3}$$

Following Bowden and Tabor, the adhesion component of the coefficient of friction can be calculated from the ratio of the shear strength to the indentation hardness of the softer material [61].

2.3.2 Wear

Reduced tolerances, degraded surfaces, and even component failure are often traced back to wear processes arising from surface interactions [62]. When two materials are in contact, mechanical and/or chemical degradation may occur. Wear is characterized by surface damage, material loss, or a combination of both [61]. While friction is involved in such contacts, there is no direct correlation between the coefficient of friction and the wear volume [60]. However, processes such as the plastic deformation of asperity contacts contribute to both friction and wear [63]. Wear is most commonly classified into four main mechanisms:

Adhesive wear is the dominant mechanism in contacts between metallic materials of similar hardness [63]. Under load, high local stresses at asperities can cause microscopic cold-welding [61, 63]. Relative sliding of the contacting surfaces then leads to junction rupture potentially causing material transfer or the detachment of wear particles, especially if the stored elastic energy exceeds the adhesion energy. Adhesion depends on the true contact area. Under ambient conditions, metallic surfaces are covered by oxide films or adsorbed layers, which reduce adhesion through weak van der Waals forces in the nonmetallic contact. However, these films can break due to the different elastic or plastic deformation behavior of the oxide and the substrate. Generally, decreasing material hardness, increasing normal force, and increasing sliding distance contribute to higher adhesive wear.

Abrasive wear occurs when a significantly harder surface or hard third-body particles, such as dirt or work-hardened wear fragments, interact with a softer material [60, 61, 63]. In this

process, hard asperities or particles cut into the softer surface and can remove material, forming grooves in the direction of sliding. Dominant mechanisms include *microplowing*, where the plastically deformed material is displaced sideways, forming ridges along the sides of the groove; *microfatigue*, which occurs when many abrasive particles, or a single particle acting repeatedly, plow material aside multiple times, eventually causing it to break off due to low-cycle fatigue; *microcutting*, which involves the complete removal of the plastically deformed material; and *microcracking*, typically observed in brittle materials, as large wear debris may detach from the surface due to crack initiation and propagation [61, 62, 64]. As the hardness of the worn material increases, microcutting becomes more dominant, and at even higher hardness levels, a transition to microcracking may occur. In ductile materials, the balance between microplowing and microcutting depends on the attack angle of the abrasive [61]. Higher angles lead to more cutting and increased wear. According to Archard's law [65], the abrasive wear volume is proportional to the normal load and the sliding distance, and inversely proportional to the hardness of the worn material. While the hardness of the abrasive plays a minor role, its ability to form sharp cutting edges is crucial, as this is typical of very hard and brittle materials [61]. In the presence of surface layers, the risk of abrasive wear further depends on their hardness, brittleness, and adhesion to the substrate, as well as on the properties of the substrate material itself.

Surface fatigue is a wear mechanism caused by repeated mechanical loading of surface regions due to tribological stress cycles [61, 63]. While each individual loading event may not cause visible damage, the repeated sliding of hard asperities induces localized fatigue, which progresses over time through elastic and plastic deformation, work softening or hardening, and ultimately leads to crack initiation and propagation, resulting in the separation of material, for instance, in the form of pits or flaking. Cracks may initiate at or beneath the surface, depending on stress distribution and material behavior. As shown by Suh and Fleming [66, 67], subsurface cracks tend to propagate parallel to the surface and release wear particles upon breakthrough, resulting in surface delamination. The driving forces for surface fatigue include both normal and frictional stresses at the contact interface, with the friction component resulting from adhesive and/or abrasive interactions between asperities and the opposing surface [61].

Tribochemical wear is characterized by tribochemical reactions between the components of a tribo-system and a gaseous or liquid environment under tribological loading, leading to the formation of chemical reaction products in the contact interface of two surfaces under relative motion [61, 63]. During this process, reaction layers continuously form and are subsequently removed by mechanical loading, which leads to surface damage and material loss. For instance, exposure to air during tribological loading can lead to *tribo-oxidation* [68]. The resulting oxides may be worn off during sliding, thereby contributing to the generation of wear debris. Tribochemical wear is largely based on the kinetics of surface layer formation and their resistance to removal, which is determined by the strength, ductility, and adhesion of the layers to the substrate, as well as by the strength of the substrate itself, affecting the resistance of the surface layer to cracking. If the hardness of the reaction layer and substrate is similar, the abrasive effect of nonmetallic wear debris on the substrate is significantly reduced.

Tribo-oxidation results from the interplay of mechanical loading and oxidative environment at sliding interfaces, leading to oxide growth rates that exceed those of native or thermal oxidation by orders of magnitude [69, 70]. It has been shown that, under mild contact conditions, interfacial shear and pressure can accelerate the rate of tribofilm formation [71]. When loading is accompanied by a temperature increase in the contact zone, oxide formation is thereby promoted [72]. At low temperatures, the dissociation of oxygen molecules and subsequent diffusion into the material occur only at particularly energetic surface sites [73]. A variety of complex mechanisms may take place under tribological loading conditions: The generated oxide film can serve as protective glaze layer, preventing direct metal–metal contact and thus reducing friction and wear [74, 75]. However, if the oxide layer becomes sufficiently thick, its microstructure tends to become porous, leading to reduced hardness [76]. Once a critical oxide thickness, usually between 1 and 3 µm, is reached, the brittle oxide becomes prone to fracture and eventually forms wear particles [77]. Wear debris may cause abrasive damage, and the oxide layer itself can be worn away, exposing fresh surfaces to reoxidation [69]. The brittle nature of the oxide thereby contributes to both tribochemical and abrasive wear [76].

Different wear mechanisms can occur in combination, and reducing one type of wear can promote another. For instance, while harder protective surface layers may reduce adhesive or tribochemical wear, their fracture under high contact pressures or microfatigue can produce

hard wear debris that encourages abrasive wear [61]. An increased thickness or coverage of brittle surface layers, resulting from higher chemical reactivity, is more prone to cracking or spalling during sliding, which can generate significant amounts of hard wear debris. This promotes a transition from adhesive wear to tribochemical and potentially abrasive wear.

2.3.3 Tribologically Induced Microstructural Layers

In the subsurface region a tribologically modified microstructure consisting of distinct layers, commonly referred to as tribolayers, can usually be observed [11, 78, 79]. The size and subsurface localization of the tribolayer are influenced by the crystallographic orientation relative to the loading direction [80]. If these surface layers are significantly harder than the underlying bulk material, stress concentrations may arise at the interface, promoting crack initiation [81]. This can result in an increased wear rate and potentially high friction. Tribolayers consisting of material from the substrate, counterbody and/or the environment, including tribo-oxides, are commonly referred to as mechanically mixed layers (MMLs) [82]. According to Li and Tandon [83], the composition of the MML in Al-Si alloys depends significantly on the applied load. In their work the layer formed under low loads, primarily consisting of the substrate material, is still referred to as the MML. In contrast, in the following, the term MML is exclusively used to denote the tribolayer consisting of subsurface nano-grained copper, already present in the gradient nano-grained (GNG) specimens prior to tribological loading, together with copper tribo-oxides. The different types of tribolayers occurring within the GNG microstructures are summarized in Figure 2.5. According to Chen and Han [13], a dynamic recrystallization (DRX) layer may form as a result of accumulated frictional heat. While Chen and Han [13] identified a tribologically induced grain coarsening layer at high contact pressures and high sliding speeds, Prasad et al. [84] observed that, during tribological tests on nano-grained nickel in dry nitrogen, an ultrafine-grained surface layer forms under low contact pressures and low sliding speeds.

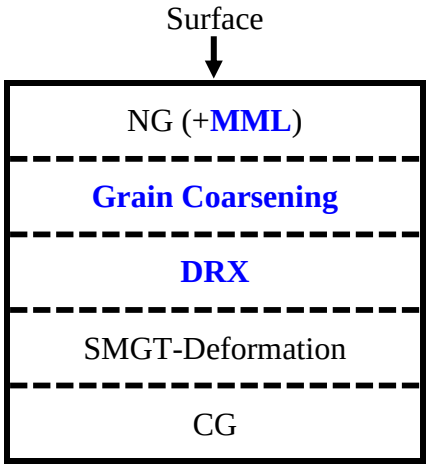

Figure 2.5: Overview of the different tribolayers, highlighted in blue, within the gradient nano-grained (GNG) microstructure beneath the surface after tribological loading (normal load: 30 N, sliding speed: 10 mm s^{-1}, stroke: 1 mm, counterbody: WC-Co sphere), according to Chen et al. [12]. NG denotes the nano-grained region, MML the mechanically mixed layer, DRX dynamic recrystallization, and CG the coarse-grained region.

2.3.4 Tribological Behavior of Copper

2.3.4.1 Coarse-Grained Copper

In copper, significant changes in the microstructure have been observed under tribological loading. During the first loading pass of a counterbody on a coarse-grained copper specimen, a dislocation trace line (DTL), characterized by a high density of accumulated dislocations, forms at a depth of 100-150 nm parallel to the surface, indicating a self-organization of dislocations [11, 85]. The DTL remains at a constant depth of 150 nm during the initial cycles, with no measurable change after ten loading cycles. This process is initiated by the generation or mobilization of pre-existing dislocations, followed by their emission from the surface region beneath the sliding sphere and their subsequent propagation into the bulk material [11]. In the region above the DTL, dislocations are either incorporated into the DTL or leave the material again through the surface. In contrast, the region beneath the DTL contains a significantly higher dislocation density. With continued reciprocating loading, the resulting plastically deformed surface layer extends deeper into the bulk material. The repeated sign changes in the stress field caused by the passing sliding sphere promote the development of the DTL. With an increasing number of cycles, more dislocations accumulate within the DTL, leading to a rise in the misorientation angle until it most probably evolves into a small angle grain boundary (SAGB) [11]. At this stage, after 100 cycles, the DTL can be found at a depth

of 200 nm. With a further increase in cycle number, a network of geometrically necessary dislocations forms and extends several micrometers into the material, creating cell walls with adjacent regions of lower dislocation density, which gradually develop into SAGBs [11, 82]. In highly strained copper, dislocation densities exceeding 10^{15} m^{-2} can be anticipated [86]. At even higher strains, the dislocation cells become smaller and their walls more defined. As stated by Huge and Hansen [87], the grain boundaries are aligned parallel to the surface, and at a strain of 12 MPa, grain sizes of about 10 nm form in the near-surface layers and coarsen with increasing depth from the surface. Ultimately, at maximum plastic strain, they evolve into subgrains and are progressively displaced deeper below the surface [86, 87]. After 500 cycles, the SAGB that evolved from the initial DTL is located at a depth of approximately 340 nm [11]. The thickness of the deformed layer follows a square root growth law with increasing cycle number, reaching a depth of 10 µm after 5000 cycles. During the evolution of the microstructure, dynamic recrystallization is unlikely to occur, given the observed increase in hardness toward the surface. Plastic deformation is locally enhanced near grain boundaries, as they act as obstacles to dislocation motion, leading to dislocation accumulation. According to Argibay et al. [88], a pure copper single crystal subjected to normal loads up to 100 mN exhibits a coefficient of friction below 0.5 during the first 10-20 sliding cycles in dry nitrogen. In this low friction regime grain sizes of 10-20 nm are present directly below the surface, allowing for shear accommodation through grain boundary sliding. Under these tribological conditions, a copper sphere with a radius of 1.19 mm in contact with a copper substrate corresponds to a Hertzian contact pressure of approximately 422 MPa at a normal load of 100 mN. In contrast, for coefficients of friction exceeding 0.5 under higher normal loads or longer test durations, larger grains are observed below the surface, and dislocation-based plasticity occurs.

Tribo-Oxidation in Copper. Before grain refinement, tribo-oxidation in copper occurs under tribological loading in air. In contrast to conventional oxidation, which typically follows a parabolic rate law indicating a decreasing oxidation rate over time, tribo-oxidation of copper shows a quasi-linear dependence on tribological test duration [89, 90]. Tribo-oxidation is initiated at surface defects like surface steps and roughness, where the energy barrier for oxidation is reduced. During this process, small islands of amorphous cuprous oxide (Cu_2O) begin to form at randomly distributed locations across the sample surface [91]. Since the

sapphire spheres used as counterbody are both hard and chemically inert, their contribution to mechanical mixing and microstructural evolution can be excluded [11, 91]. After ten sliding cycles, a discontinuous layer with a thickness of less than 10 nm forms at the surface. As sliding progresses, the oxide islands grow into semicircular features at and beneath the surface. This characteristic shape results from oxidation occurring predominantly at the copper-oxide interface, where oxygen diffusion is significantly faster than in pure copper, making it the primary diffusion pathway [91–93]. After 50 cycles, a wavy and discontinuous surface layer composed of these oxides appears, with a thickness of approximately 30 nm. Unlike native oxidation, where oxides typically form on the surface, tribo-oxides grow into the underlying material [70]. According to Liu et al. [91], the formation of copper oxide occurs during the passage of the sphere, indicating a tribologically induced mechanical process. However, Rau [94] found that dislocations are transported during the passage of the sphere but become stationary once the stress field moves too far away, allowing oxygen to diffuse along them before and after the sphere passes. With progressing oxidation and the consequent enlargement of oxide, the thermodynamic instability of the amorphous matrix promotes the nucleation and growth of Cu_2O nanocrystals within the amorphous phase, while the coalescence of the semispherical features leads to the formation of a continuous oxide layer [91].

Oxide growth under mild tribological loading conditions is assumed to be primarily driven by oxygen diffusion within and along the copper surface and, most significantly, at the interface between copper and its oxide [91]. The underlying driving forces for the diffusion include the concentration gradient between the high-purity copper substrate and the surrounding atmosphere, local differences in oxide composition such as compositional differences between nanocrystalline Cu_2O and the surrounding amorphous matrix, as well as strain resulting from plastic deformation [90, 91]. High defect densities can accelerate oxygen penetration into the material even under ambient conditions, through pipe diffusion along dislocation cores formed during plastic deformation, as well as phase boundary and grain boundary diffusion, eventually leading to supersaturation of the copper bulk with oxygen [90]. As oxidation progresses, diffusion pathways within the growing complex oxide become dominant. These include the metal-oxide interface and dislocations. Even though it remains uncertain which species diffuses due to the transition from metallic copper to an ionic oxide, Rau et al. [90]

suggest that copper atom diffusion is likely to dominate during the early stages of oxidation when metallic copper is still present, whereas copper ion diffusion may become increasingly important as the oxidation progresses. According to the Kirkendall effect, the outward diffusion of copper ions exceeds the inward diffusion of oxygen ions into the bulk material [95]. The resulting imbalance is compensated by an inward flux of copper vacancies, leading to the formation and reorganization of nearly spherical Kirkendall pores with a diameter below 50 nm. Kirkendall pores are considered temperature-independent and form as a result of diffusion along high-diffusivity pathways such as grain boundaries, phase boundaries and dislocations [70]. Their presence provides additional diffusion paths, that facilitate rapid oxygen penetration into the material. As a consequence, oxides are expected to either grow deeper into the sample or form more cupric oxide (CuO) at elevated temperatures. At the pore surfaces, oxygen from the surrounding environment can directly react with copper, resulting in oxide formation at the pore-metal interface. Apart from accelerated oxidation, Kirkendall pores may contribute to the delamination of wear particles from the sample surface [91, 96].
During oxidation of copper at temperatures between 200 and 300 °C, a layered oxide structure typically forms [93]. At the outer surface, a CuO layer with an oxygen concentration of around 50 at% is observed. Beneath this, a Cu_2O layer forms with an oxygen content of approximately 30 at%. Further below, a diffusion zone extends into the substrate, where the oxygen content gradually decreases to 0 at%. Cu_2O typically forms in the cubic crystal structure during native oxidation, and its color varies with the oxide thickness, shifting from brown to purple as the oxide layer becomes thicker [97, 98]. The formation of Cu_2O results in a volume expansion to 1.7 times that of copper [99]. In contrast, CuO exhibits a monoclinic structure and appears black [98, 100]. Furthermore, CuO has a volume 1.8 times that of copper [99]. While both oxides exhibit a lower coefficient of friction compared to high-purity copper, primarily due to their increased hardness and altered shear strength, tribo-oxides formed on copper have a higher coefficient of friction than pure Cu_2O or CuO [69].

Several factors can influence the tribological performance of copper, such as grain size, porosity, and surface roughness. The influence of **pores** on the tribological behavior under unlubricated conditions can result in either an increase or a decrease in friction and wear. Ordoñez et al. [101] found that although a higher sintering porosity in Fe-Mo-C steel leads to an increased wear rate, it also results in a slight reduction of the coefficient of friction. In

contrast, Sinha and Farhat [26] showed that higher porosity in both aluminum and aluminum alloy 6061 leads to increased friction, due to enhanced asperity–asperity contact, as well as increased wear, due to porosity-induced higher surface roughness and a reduction in hardness. On the other hand, Martin et al. [25] demonstrated that increasing the porosity of stainless steel can improve wear resistance under unlubricated conditions, as they assumed that during the initial stages of sliding, the pores are filled with wear debris and by plastic deformation. Chen et al. [17] showed that nanopores in gold can enhance strength without compromising ductility by trapping dislocations at the nanopores.

Similarly, no general relationship can be established between **surface roughness** and tribological behavior. While Al-Samarai et al. [102] found that friction increases with higher roughness on aluminum-silicon casting alloys, Kubiak et al. [103] observed that in both plain carbon steel (AISI 1034) and titanium alloy (Ti-6Al-4V), lower friction prevails at high roughness under fretting conditions. Liang et al. [104] revealed that an increased roughness on AISI 1045 steel specimens leads to an unstable coefficient of friction with greater fluctuations. According to Popov [63], under dry sliding conditions, surfaces should be as smooth as possible, in order to reduce wear. In order for the contacting bodies to deform only elastically, the mean slope of the surface profile must not exceed a value of 0.01, and the roughness wavelength should be kept as small as possible. This ensures that the diameter of the microcontacts remains too small to enable adhesive wear. If the mean slope exceeds 0.01, local plastic deformation can occur. In such cases, the resulting wear behavior is strongly influenced by the mechanical properties of the outermost surface layers.

2.3.4.2 Gradient Nano-Grained (GNG) Copper

During the tribological loading of gradient nano-grained (GNG) copper samples, the gradient distribution of the applied stress in the GNG structure aligns with the depth-dependent yield strength and enables effective accommodation of plastic strain beneath the surface without localization [12]. The GNG layer exhibits a yield strength that is around ten times higher than that of the underlying coarse-grained (CG) structure [105]. Consequently, the overall yield strength of the surface mechanical grinding treated (SMGT) specimen is about two times higher than that of a pure CG sample. The GNG layer significantly increases strength without compromising plasticity, resulting in SMGT samples exhibiting plasticity comparable to that

of CG samples. Tribological experiments with normal loads ranging from 5 to 90 N demonstrate that the GNG structure enables a low steady state coefficient of friction in the range of 0.25 to 0.32, according to Li et al. and Chen et al. [14, 29]. The low coefficient of friction is attributed to the suppression of surface roughening and the prevention of cracking and delaminating tribolayer formation typically caused by sliding-induced plastic deformation [12]. This promotes a mild plowing wear mechanism with minimal wear loss. The wear depth is comparable to that in nano-grained (NG) samples, and no transfer layer is observed on the WC-Co counterbody [29]. According to ISO 80004-1:2023 [106], the nanoscale is defined as a length range from 1 to 100 nm, so grain sizes up to 100 nm are to be expected in NG samples.

The subsurface microstructure evolves during tribological loading in the low-friction regime, as shown in Figure 2.6. This includes grain coarsening and, after 3000 cycles, the formation of numerous elongated submicron-sized grains oriented parallel to the sliding surface. The sharp interface is observed between the grain coarsening and dynamic recrystallization (DRX) layer, while the transition from the DRX to the deformation layer caused by the SMGT process is more gradual [12, 13]. The top surface layer exhibits slower grain growth and reaches a smaller saturated grain size compared to the subsurface region [105]. This behavior is likely attributed to the depth-dependent variations in grain morphology and grain boundary characteristics. While in the top GNG layer, a large proportion of grain boundaries originate from deformation twins, the subsurface layer subjected to much lower strain rates, predominantly features conventional high-angle grain boundaries resulting from dislocation activity. The formation of deformation twins is commonly observed in metals with low to medium stacking fault energy, as is the case for copper with a stacking fault energy of approximately 40 mJ m^{-2}, particularly under conditions where dislocation activity is suppressed, such as at the high strain rates and cryogenic temperatures prevailing during the SMGT process [107, 108]. As confirmed by diffusivity measurements, the grain boundaries in the subsurface layer exhibit higher excess energy than the twin boundary like grain boundaries in the top NG layer, making them more resistant to grain coarsening [109]. Further suppression of grain growth in the NG layer can be achieved by increasing the strain rate during tensile testing, indicating that the occurring grain growth is predominantly driven by mechanical stress, similar to the behavior found in NG microstructures [105, 110]. Thus, a high strain rate resulting from an elevated sliding speed during the tribological tests likely

plays a crucial role in stabilizing the fine NG structure [12]. As a result, neither microstructural changes nor oxidation occur in the topmost layer of the GNG structure due to tribological loading. Notably, strain softening and dislocation hardening act as competing mechanisms in this context. Microstructural saturation at the submicron scale occurs when dislocation activity and grain boundary interactions are balanced with grain boundary migration and dislocation annihilation [29]. Under tensile loading, deformation mechanisms operating withing the GNG layer include dislocation slip and diffusion-controlled processes [105]. At room temperature, substantial grain boundary motion is enabled by the release of energy through defect annihilation in the nanostructure, which effectively accommodate the large plastic strains.

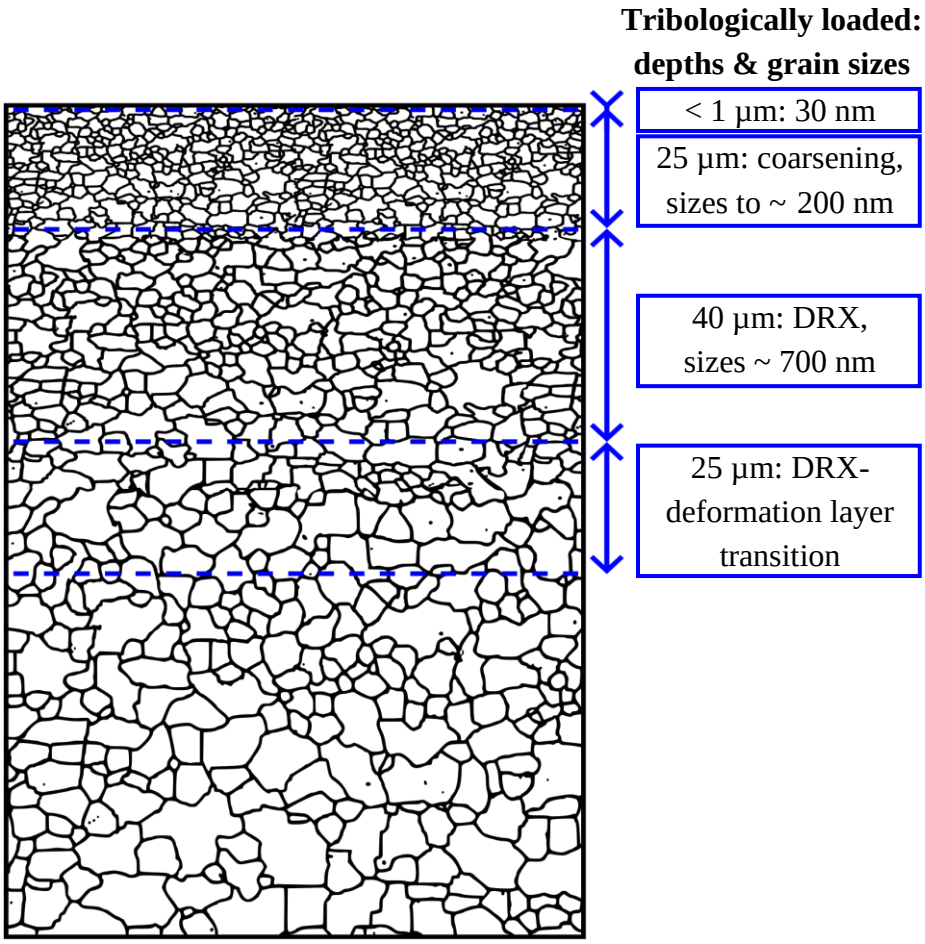

Figure 2.6: Microstructure of a surface mechanical grinding treated specimen after tribological loading (normal load: 30 N, sliding speed: 10 mm s^{-1}, stroke: 1 mm, counterbody: WC-Co sphere), as reported by Chen et al. [12]. The DRX represents the dynamic recrystallization.

Behavior of NG and CG under Identical Tribological Conditions. In contrast to GNG, NG and CG microstructures exhibit a uniform yield strength across the depth. Consequently, once the plastic strain in the surface layer becomes too high to be accommodated, it induces strain localization and surface damage [12]. Repeated sliding results in the formation of cracks perpendicular to the sliding direction and particle detachment, which are subsequently cold-welded back onto the surface [29]. This process leads to the formation of a brittle, nanostructured MML beneath the surface, as shown in Figure 2.7 [12, 29]. The MML, composed of Cu_2O and Cu grains approximately 15 nm in size and containing a significant amount of oxygen from the environment, contributes to the high coefficient of friction and increased surface roughness. With increasing sliding cycles, the MML thickens, eventually reaching a thickness of several micrometers. The DRX zone is located directly beneath the MML, with the interface marked by a sharp transition in both grain size and chemical composition. While the coefficient of friction remains at 0.35, plowing is the dominant wear mechanism. Upon oxidation and delamination, the coefficient of friction increases to a steady-state value of 0.63, accompanied by a transition from a WC-Co/Cu contact to a WC-Co/MML wear pair [14]. During the steady-state regime, the tribological behavior is primarily controlled by the surface condition, with the initial microstructure playing a negligible role. The observed variations in steady-state coefficient of friction for NC and CG are linked to delamination at the wear surface, resulting in an *Ra* increase from 0.03 to 0.18 µm [12, 14]. The underlying microcracks are commonly observed within the MML as well as at the interface with the DRX layer [12, 29].

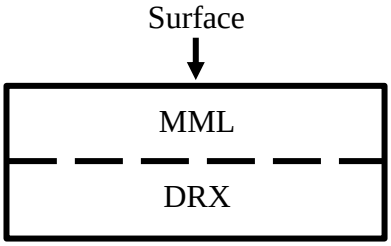

Figure 2.7: Tribologically induced formation of a mechanically mixed layer (MML) and a dynamic recrystallization (DRX) layer within the nano-grained and coarse-grained microstructures under severe tribological loading conditions (normal load: 30 N, sliding speed: 10 mm s^{-1}, stroke: 1 mm, WC-Co sphere as counterbody), as reported by Chen et al. [29].

The enhanced wear resistance of **NG** copper compared to CG copper, can be primarily attributed to its higher hardness, which suppresses the formation of a MML [14]. Even when

delamination occurs in NG copper, the thickness of the delaminated layer remains much smaller than in CG. This behavior results from a less pronounced MML and a thinner sliding-induced, work-hardened tribolayer in NG copper. Since delamination originates from poor strain compatibility between the metallic matrix and the MML, the reduced MML formation in NG copper favors a plowing-dominated wear mechanism rather than delamination, leading to a wear resistance that exceeds that of CG by at least one order of magnitude under increasing loads. However, high-load sliding may lead to rapid MML detachment and even cracking in the adjacent deformation layer [13]. Although the crack density in NG is lower, the individual cracks tend to be longer than those in CG [29]. These cracks, along with pile-up formations, result from high localized plastic strains in the surface layer with limited deformability, where the stress exceeds the yield strength. Below the DRX layer, which consists of randomly oriented grains of around 700 nm in size, the original microstructure of NG samples remains preserved at depths greater than 40-50 µm.

In **CG** copper, pronounced pile-up formations indicate significantly greater plastic deformation than in NG copper, along with the accumulation of wear debris and a considerably rougher wear scar interior [14]. The considerable plastic deformation in the subsurface region facilitates delamination and further contributes to increased surface roughness.

Low to High Friction Transition. The transition from low to high friction in GNG microstructures during sliding, which means an increase in the coefficient of friction from approximately 0.35 to 0.65, is governed by the subsurface stability and the applied sliding conditions [13]. Under a normal load of 30 N, the coefficient of friction of GNG copper begins to increase after 10000 sliding cycles. During this stage, vertical plastic flow initiates in the grain coarsening layer, the position of which within the microstructure is schematically illustrated in Figure 2.5. Once plastic strain can no longer be uniformly accommodated, it extends into the uppermost NG layer leading to local variations of its thickness. Laminar cracks at 1-2 µm depth are attributed to the detachment of saturated coarsened grain regions. Upon entering the high-friction regime at a coefficient of friction of approximately 0.6 after 15000 cycles, a sharp interface develops between the surface NG layer and the underlying grain coarsening layer, as the NG layer contains not only copper but also oxides, thus forming

a MML, as depicted in Figure 2.5, analogous to those formed in NG and CG microstructures. Meanwhile, the underlying grain coarsening region, which previously showed grain sizes of up to 200 nm during the low-friction stage, exhibits grain refinement to below 100 nm. As the increase in the coefficient of friction precedes the onset of MML formation, surface roughening caused by shear instability, which leads to local thickness variations in the NG layer, is considered the primary cause [13, 111]. The roughened surface not only increases friction but also promotes crack formation, potentially resulting in delamination at the surface. This rise in the coefficient of friction, along with changes in the subsurface microstructure, indicates that the nanoscale grains in the topmost layer are essential for maintaining low friction.

Apart from the transition from low to high friction with increasing sliding cycles, the tribological test conditions also significantly affect the frictional behavior. Low coefficients of friction and a mild plowing wear mechanism have been observed in a few NG metals under low tribological stress, namely at low sliding speeds, low normal loads, or under lubricated conditions [12]. The increase in the coefficient of friction with sliding speed observed in NG microstructures indicates a significant strain-rate sensitivity of the delamination process [12, 112]. This is consistent with the behavior of NG Ni, which exhibits greater strain-rate sensitivity compared to CG Ni [113]. The enhanced sensitivity is partly attributed to the increased contribution of grain-boundary-mediated plasticity at reduced grain sizes [113]. For grain sizes below 20 nm, plastic deformation in both Cu and Ni is dominated by grain-boundary shear, rather than dislocation activity within the grain interior.

In addition to sliding speed, the normal force plays a key role in the transition from low to high friction, not only in GNG, but also in CG microstructures. Under a load of 5 N and identical experimental conditions as described above, both GNG and CG copper exhibit a low steady-state coefficient of friction around 0.3 during 18000 cycles [14]. However, the wear behavior differs significantly as the wear volume of CG copper is approximately 20 times greater than that of GNG copper and remains more than one order of magnitude higher even at 25 N, where GNG copper still exhibits a smaller wear depth than CG copper tested at 5 N. In both cases, wear increases with rising load. The increased wear resistance of GNG microstructures can be attributed to their higher hardness, which favors wear behavior dominated by plowing. While GNG microstructures maintain a low coefficient of friction of

< 0.4 even at increased normal loads of 10 and 15 N, CG microstructures already exhibit a high coefficient of friction of around 0.6 at 10 N. A further increase in load reveals that at 25 N, however, the coefficient of friction of GNG copper progressively increases over the sliding cycles, reaching a value of 0.6 after 18000 cycles. At reduced loads, where the coefficient of friction is low, wear scars are shallow and the amount of wear debris is minimal. This allows most debris to be removed from the contact zone, thereby preventing oxidation. However, as the normal load increases and the wear scar deepens, a MML forms that exhibits poor strain compatibility with the underlying metallic matrix, leading to delamination, a change in the wear pair, and an increase in the coefficient of friction. The formation of a MML is favored in CG copper samples due to its lower hardness, which contributes to the observed increase in the coefficient of friction at lower loads compared to GNG copper.

2.4 Objective and Content of this Work

Copper is not only a material with outstanding properties for a wide range of applications but has also been extensively investigated for its tribological behavior. These studies revealed that single-crystalline and coarse-grained copper exhibit a steady-state coefficient of friction exceeding 0.5 under mild tribological loading conditions at macroscopic normal loads [69, 88, 114]. In addition to the low coefficients of friction observed during tribological tests on single-crystalline copper in nitrogen under microscopic normal loads, it was found that a gradient nano-grained (GNG) surface layer in coarse-grained copper can also reduce friction under severe tribological loading conditions [13, 88]. However, it remains unclear whether this is also the case under mild tribological loading conditions relevant for many practical applications, where low macroscopic loads and sliding speeds prevail. This understanding is essential for determining whether GNG microstructures can serve as an effective and energy-efficient surface modification strategy beyond the severe loading regimes investigated so far. Furthermore, the influence of pores on the tribological behavior of copper under mild loading conditions has not yet been systematically investigated, even though pores are inherent to many manufacturing routes. Understanding how pore size and porosity affect friction and wear is crucial for evaluating the tribological potential and limitations of sintered or additively manufactured copper and for identifying how microstructural features influence tribological performance to guide future process optimization. This could be particularly relevant for

lightweight applications if porosity proves advantageous, as it may enable both improved tribological performance and mass reduction, thereby increasing energy efficiency. Consequently, there remains a lack of understanding about which copper microstructure contributes to friction reduction under mild tribological loading conditions, as defined in this study by low macroscopic load and low sliding speed.

In order to contribute to global energy reduction, this work investigates the tribological behavior of different copper microstructures under mild tribological loading conditions, with the primary objective of investigating the influence of the microstructure on the friction behavior. Building upon the insights from multiple previous studies, the tribological testing conditions were selected accordingly. While earlier investigations have found a substantial friction reduction effect of the GNG copper microstructure under severe tribological loading conditions, only an increase or a slight decrease in the coefficient of friction due to porosity under dry conditions has been observed in metals so far [26, 101]. Therefore, the leading hypothesis of this work assumes that GNG microstructures exert a stronger influence on the tribological behavior of copper under mild loading conditions and can reduce friction more effectively than porous copper samples. The study focuses on evaluating whether grain size or porosity, often unavoidable in some manufacturing processes, predominantly governs the tribological performance of copper. Accordingly, the first guiding question arises: To what extent can a GNG surface layer reduce the coefficient of friction under mild tribological loading conditions, and how do the layer thickness and surface grain size influence the resulting tribological performance? As GNG microstructures have demonstrated friction reduction under severe loading conditions, the influence of different GNG microstructures, characterized by varying layer depths and surface grain sizes, was first analyzed under both severe and mild tribological conditions to determine the key microstructural features required for lowering the coefficient of friction. Since the effect of pores on the tribological performance of copper remains unexplored, the second guiding question is: How do pore size as well as overall and surface porosity influence the tribological behavior? The second part of this work therefore examines how the amount and size of pores in sintered samples affect their friction and wear behavior. Additionally, by significantly increasing the test duration, the study assesses the long-term evolution of the coefficient of friction depending on porosity and pore size. Finally, the impact of various surface treatments, such as chemical-mechanical

vibropolishing and electropolishing, on the tribological behavior of porous samples was investigated to directly evaluate the effect of surface porosity. This approach enables an isolated evaluation, as subsurface porosity remains unchanged, and only the surface porosity is modified. In contrast, variations in manufacturing conditions would also affect subsurface porosity, overlapping the surface porosity effects.

3 Materials & Methods

In the following, the materials used in this work, the manufacturing conditions, the tribological experimental parameters, and the characterization methods for surface and microstructure analysis are described. The selected tribological experimental parameters are based on previous studies to ensure comparability and to utilize previously gained insights for interpreting the results.

3.1 Materials, Sample Fabrication and Preparation

Copper was chosen for the investigations in this study, as its tribological behavior under mild loading conditions has already been thoroughly analyzed, providing a solid basis for the interpretations of the results. Moreover, copper exhibits high electrical and thermal conductivity combined with pronounced ductility, which promotes uniform heat distribution and facilitates the densification of powder particles during the sintering process [115–118]. Samples with a gradient nano-grained (GNG) microstructure were prepared from a copper rod with a purity of 99.95 %, a diameter of 10 mm ± 0.25 mm and a length of around 600 mm provided by Goodfellow GmbH, Hamburg, Germany. As the procedure is based on Chen et al. [12], the samples were prepared to closely match their specifications, which include a purity of 99.97 wt% and comparable dimensions.

Porous samples were produced using two different copper powders, each with a purity of 99.95 %. The remaining impurities comprised 17 ppm silver and other elements, each below 10 ppm. Both powders were supplied by Inopowders S.A.S, Paris, France. The particle size distribution of the fine powder exhibited a d90 value of 20 µm, while the coarse powder had a d90 value of 36 µm. To prevent oxidation, the powder was stored in argon and, after filling the die for the sintering process, kept under vacuum. The tribological experiments were conducted using a polished, single-crystalline sapphire sphere as the counterbody, with a diameter of 10 mm, manufactured by Saphirwerk AG, Brügg, Switzerland. Sapphire was chosen as the counterbody in the tribological experiments because of its chemical inertness and its high hardness of about 29 GPa in the hexagonal close-packed plane, as measured by Berkovich nanoindentation, making it one of the hardest known materials [119, 120]. This

ensured that tribochemical interactions were minimized and that the tribologically induced plastic deformation predominantly occurred within the copper specimens. Additionally, tribological tests were conducted on GNG copper using WC-6Co spheres from TN United Kingdom LTD, Worthing, United Kingdom, with a diameter of 10 mm following the approach of Chen et al. [12]. This ensured consistent testing conditions and comparability of results.

Gradient Nano-Grained Sample Preparation. To analyze the effect of GNG microstructures, particularly with different layer thicknesses and surface grain sizes, on the tribological behavior under mild loading conditions, copper rods were first cut using a metal-cutting band saw type HY 180-4 from ELMAG Entwicklungs und Handels GmbH, Tumeltsham, Austria. The rods measured 7 cm in length for the sample hereafter referred to as GNG2, and 20 cm for the sample hereafter called GNG1. In comparison, the copper samples used by Chen et al. [12] were 15 cm long. In this study, the samples were heat-treated under vacuum in a tube furnace type TF1-1200 from Carbolite Gero GmbH & Co. KG, Neuhausen, Germany. They were heated to 550 °C over a period of 2 h and held at this temperature for another 2 h before being cooled down. In comparison, Chen et al. [12, 29] annealed the samples at 450 °C for 2 h to produce a homogeneous coarse-grained (CG) microstructure with an average grain size of approximately 20 μm. Subsequently, the pieces were manually sawed into smaller parts, with the cut side then being clamped into a lathe type LZ Primus from Weiler Werkzeugmaschinen GmbH, Emskirchen, Germany. Prior to the SMGT process, the samples were stabilized by turning in the centering tip. Then, the specimens were cooled in a liquid nitrogen bath for 5 min before the first chip was cut using a cutting tool operating at 2200-3000 rpm. Material was removed to a depth of approximately 0.2-0.3 mm to achieve a good and homogeneous surface quality for the surface mechanical grinding treatment (SMGT). Afterwards, the samples were cooled again in a liquid nitrogen bath for 5 min. The SMGT process followed the procedure described by Chen et al. [12]. In this process, a WC-Co sphere with a radius of 8 mm was brought into contact with the sample surface. In contrast to Chen et al., where the sphere moved at 3 mm min^{-1} and the copper rod rotated at 600 rpm, the present study used a sphere speed of 18.9 mm min^{-1} and a rod rotation speed of 660 rpm. Table 3.1 presents the different sample types used for the tribological experiments along with the respective indentation depths. It should be noted that both GNG-0(Chen) and GNG-30(Chen) are reference samples taken from the work of Chen et al. [12]. Furthermore, the

GNG2-10 and GNG2-160 microstructures originate from the same specimen GNG2 but differ in the amount of material removed from the surface prior to the tribological experiments. All samples underwent six sphere passes. For the samples prepared in this study, continuous liquid nitrogen flooding was applied during each pass, followed by an additional 5 min cooling step in a liquid nitrogen bath after each pass to prevent annealing during the severe plastic deformation. Due to elastic deformation recovery after each pass, GNG2 exhibited a greater total indentation depth of the sphere after the six passes compared to GNG1, as shown in Figure 3.1. While in GNG1 the sphere indented 40 µm into the current surface with each pass, in GNG2 an additional indentation depth of 40 µm was added to the position of the initial surface with every pass. As a result, despite cooling, the GNG2 sample showed an orange discoloration after the fourth pass. With a processing length of around 20 mm, a single pass took about 60 s, followed immediately by cooling. Since oxidation at elevated temperatures can therefore only occur for a maximum of 60 s, an orange oxide can form in this time period at temperatures between 300 °C and 350 °C [98]. Therefore, the fifth and the sixth passes of the sphere on the GNG2 specimen were each interrupted halfway through to cool the sample again in a liquid nitrogen bath for 5 min before continuing the process. This approach helped to prevent annealing of the sample. The maximum processing length before the sample began to anneal during the sixth pass was 1 cm. For GNG1, due to the lower overall indentation depth of the sphere, a processing length of 2 cm could be achieved.

Table 3.1: Overview of the various gradient nano-grained (GNG) specimen types relevant to this study, differing both in SMGT processing conditions and in subsequent surface finishing procedures. GNG is a reference sample from Chen et al. [12, 29], whereas GNG1 and GNG2 were prepared in the present study.

Base sample & SMGT parameters	**Sample type including post-treatment**
GNG [12]	
Indentation depth per pass: 40 µm Total indentation depth: 240 µm	**GNG-0(Chen)** (no surface removal) **GNG-30(Chen)** (20-30 µm surface removal)
GNG1	
Starting position: *current* surface contact Indentation depth per pass: 40 µm	**GNG1-60** (60 µm surface removal)
GNG2	
Fixed starting position: x_0 = 0 µm Indentation depth per pass i: $x_i = x_{i-1}$ + 40 µm	**GNG2-10** (10 µm surface removal) **GNG2-160** (160 µm surface removal)

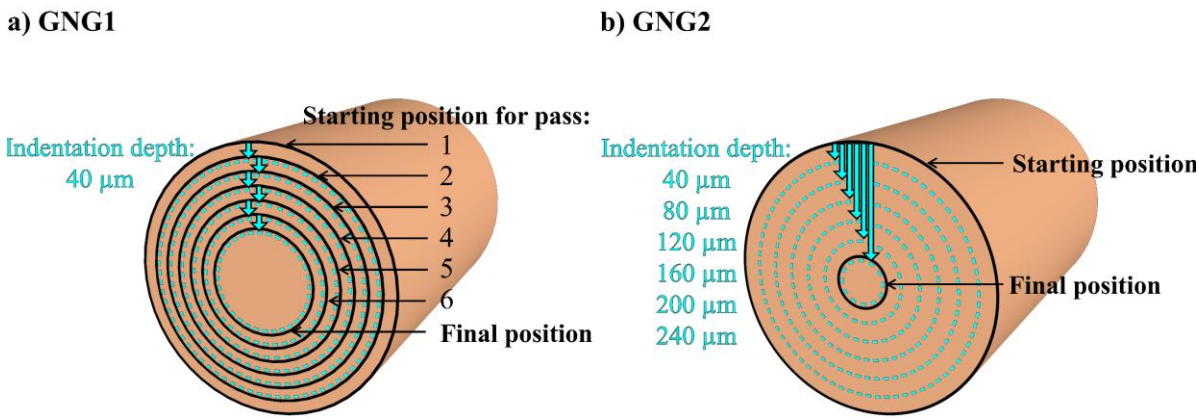

Figure 3.1: Schematic representation of the different starting positions (black arrows) and indentation depths (blue arrows) of the WC-Co sphere during the surface mechanical grinding treatment of a) GNG1 and b) GNG2. The dashed line indicates the indentation depth during the different passes, causing elastic-plastic deformation. Upon unloading, elastic recovery results in the new surface being positioned less deep than during indentation.

After surface processing, the GNG-30(Chen) sample was obtained by removing 30 µm from the surface through grinding and subsequent polishing. Both GNG-0(Chen) and GNG-30(Chen) samples were electropolished prior to the tribological tests. The GNG2 sample was cut into two halves using a wire electrical discharge machining system type BA24 from

Mitsubishi Electric Europe B.V., Ratingen, Germany, in order to both enable a more stable support of the specimen during the tribological test and to allow a larger surface area to be used for further tribological experiments, as shown in Figure 3.2. Subsequently, surface post-treatments were performed parallel to the plane of the eroded section, as demonstrated in Figure 3.2c), removing 60 µm from the surface of GNG1-60, 160 µm from GNG2-160 and 10 µm from GNG2-10. To facilitate better handling, the specimens were embedded using Epoxy 2000 resin and hardener from Cloeren Technology GmbH, Wegberg, Germany. For surface preparation, they were initially ground for a few seconds using SiC papers with grit sizes of #800, #1200, #2500, and #4000 on a Saphir 320 grinding machine at a rotation speed of 150 rpm, both supplied by QATM GmbH, Mammelzen, Germany. Afterwards, the specimens were manually polished using diamond suspensions Mono 3 µm and Mono 1 µm from Cloeren Technology GmbH, together with a lubricant consisting of 1000 ml distilled water, 10 g detergent, and 250 ml isopropanol. Polishing was carried out on MD-Dur polishing discs with a LaboPol-30 polishing machine, both from Struers GmbH, Fellbach, Germany. After mechanical removal of the embedding material, electropolishing was performed on 1 cm^2 of the prepared surfaces of GNG2-160 and GNG2-10 for 20 s at 24 V with a flow rate of 8, whereas 0.5 cm^2 of GNG1-60 was electropolished for 20 s at 28 V with a flow rate of 16. The electropolishing was performed using the LectroPol-5 electropolishing device and the D2 electrolyte from Struers GmbH. Both parameter settings ensured the removal of the Beilby layer without causing significant attack on the grain boundaries. Following electropolishing, the specimens were rinsed with 200 ml of deionized water and subsequently cleaned ultrasonically in isopropanol for 10 min. Since several tribological experiments were conducted on the sample surfaces and a comparable native oxide layer thickness was required, the samples were aged in air for 24 h before the first test to allow the oxide layer to stabilize, as the oxidation rate decreases significantly after the first few hours of exposure to air [121].

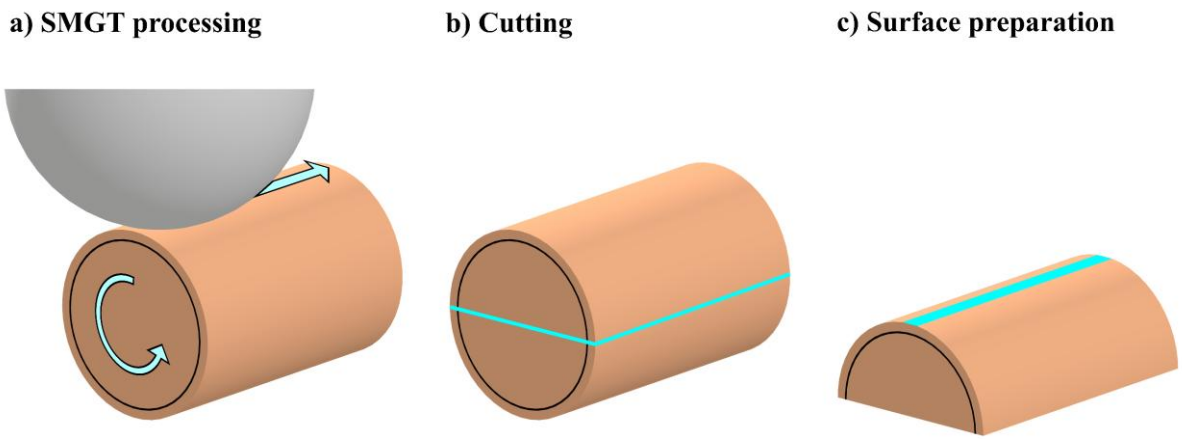

Figure 3.2: Overview of the gradient nano-grained sample preparation, from surface mechanical grinding treatment (SMGT) to surface preparation for tribological testing. The black inner circle represents the depth of the deformed gradient layer.

Porous Sample Fabrication. To investigate the influence of porosity on the tribological behavior, various specimens with different pore sizes and porosities were first fabricated using field assisted sintering technology (FAST). For this purpose, a CT HP D 25/1 from FCT Systeme GmbH, Frankenblick, Germany, was employed. While the fine powder was used to produce specimens with few small sintering pores (FSP) and many small sintering pores (MSP), the coarse powder was processed to fabricate specimens with few big sintering pores (FBP) and many big sintering pores (MBP). In order to investigate the effect of surface treatment, another MSP specimen was produced to treat its surface in a different manner before performing the tribological testing. Before the sintering process, the powder was filled into a graphite mold lined with a 0.3 mm thick graphite foil, with a diameter of 20 mm and a filling height of 18 mm, and manually pre-compacted with a force between 3 and 5 kN. During the entire FAST process, a pulsed direct current with a pulse duration of 25 ms and a pause of 5 ms was used. At the beginning of the FAST process, the specimens were subjected to a force of 5 kN, while a vacuum of < 1 mbar was drawn within 3 min. The chamber was then flushed with argon for 45 s before being evacuated again for 1 min. The subsequent sintering process was conducted under an argon atmosphere at 8-12 mbar with continuous argon flushing of the chamber. This argon flow prevented fogging or contamination of the pyrometer's sight window, as outgassing from the samples or graphite die could condense on cooler components, particularly the water-cooled mount of the pyrometer, and impair measurement accuracy. While the load on the specimens with few sintering pores was increased to 15.7 kN

within 1.5 min, the force on the specimens with many sintering pores remained unchanged during this time interval. Following this, all specimens were heated with a maximum heating power of 21 kW, corresponding to a heating rate of approximately 140 K min^{-1}, until the pyrometer integrated into the upper punch registered a temperature of 450 °C. Subsequently, the heating was continued with a set rate of 100 K min^{-1} until the maximum temperature of 600 °C was reached. To ensure that differences in grain size do not arise from the manufacturing process, all specimens were held at the maximum temperature for 2 min before being cooled to 400 °C at a rate of 100 K min^{-1}. Once 400 °C was reached, the force on the specimens loaded with 15.7 kN was reduced to 5 kN within 1 min, while the force on the other specimens remained unchanged. After ventilation and a waiting time of 7 min, the chamber was opened, allowing the die to reach room temperature after an additional 5 min. Figure 3.3 exemplarily shows the progression of force, temperature, and speed, defined as the rate at which the punches move toward each other, over time during the field assisted sintering of a low-porosity specimen. To investigate the influence of an additional cold-isostatic pressing (CIP) step on the tribological behavior, FSP and FBP specimens were each fabricated in duplicate to produce a CIP-treated sample with few small pores (FSPC) and one with few big pores (FBPC). CIP was conducted at 400 MPa for 6 h, using a KIP100E from Paul-Otto Weber GmbH, Remshalden, Germany. Glycol PG46 from Dunze GmbH, Hamburg, Germany, was used as the press medium. In summary, the specimen types and their main distinguishing features are shown in Figure 3.4.

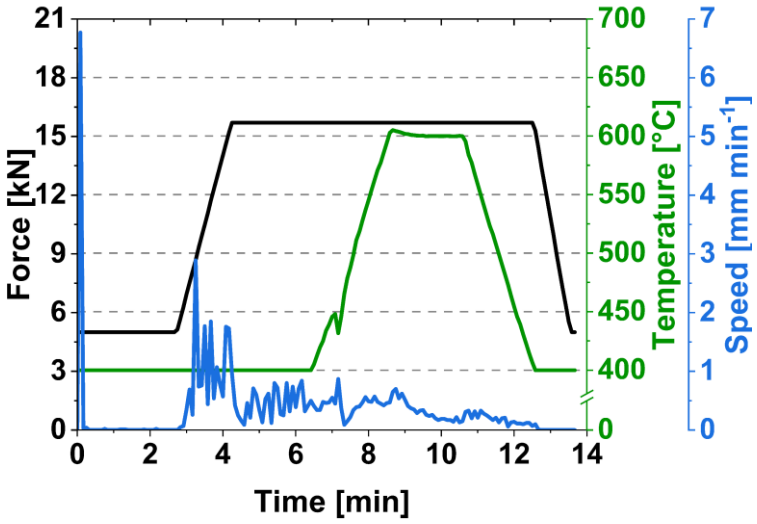

Figure 3.3: Evolution of punch force, temperature, and punch moving speed during the field assisted sintering process for a low-porosity sample.

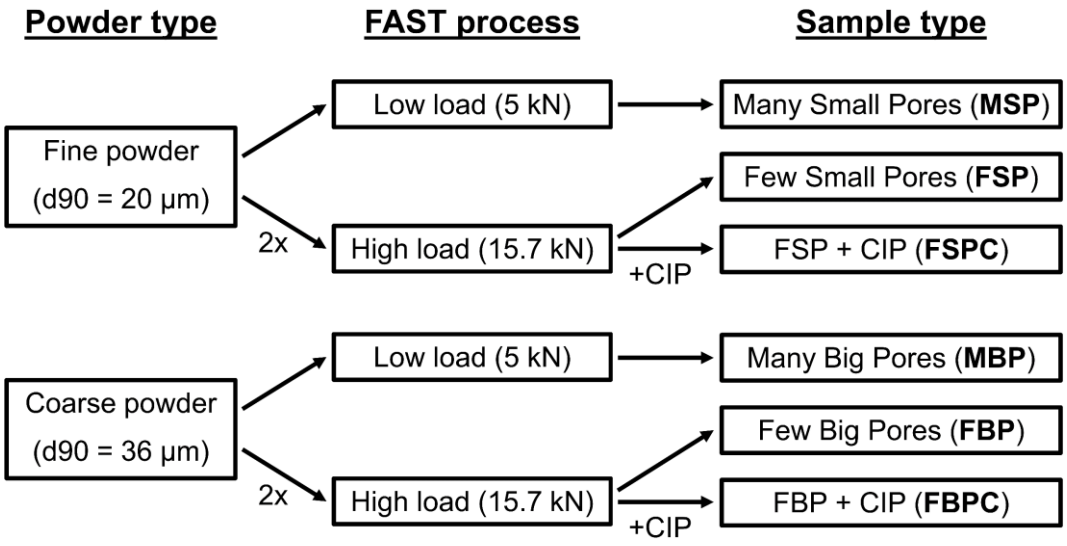

Figure 3.4: Overview of the key differences in the fabrication of the porous specimen types used in this study [122]. After the field-assisted sintering technique (FAST), some samples underwent an additional cold-isostatic pressing (CIP) step.

To ensure a high and comparable surface quality between the specimens and to remove the adhering graphite foil, the samples were manually ground with SiC paper of different grit sizes (#800, #1200, #2500, #4000) on a grinding machine Saphir 320 at a rotation speed of 150 rpm, both from QATM GmbH. A water-cooling system was used during the grinding process to prevent heating of the specimens. Subsequently, all samples were manually polished using MD-Dur polishing discs on a LaboPol-30 polishing machine, both from Struers GmbH. Polishing was carried out for 20 min with Mono 3 µm and for 30 min with Mono 1 µm diamond suspensions from Cloeren Technology GmbH, together with the lubricant described above. Afterwards, the different specimen types underwent either a chemical-mechanical vibropolishing or an electropolishing step. To expose the sintering pores introduced during preparation and remove residual deformations, the specimens were loaded with 400 g and subsequently vibropolished in air for 15 h with OP-U non-dry from Struers GmbH, on a VibroMet 2 from Buehler, Lake Bluff, Illinois, United States, with an amplitude of 60 % on a MicroCloth disc from Buehler ITW Test and Measurement GmbH, Leinfelden-Echterdingen, Germany. Subsequently, the specimens were pre-cleaned for 10 min on a clean MicroCloth disc with distilled water using vibration. The preparation was completed with a manual cleaning in distilled water with detergent, followed by a final rinse with isopropanol. During electropolishing of the second MSP sample, 2 cm^2 of the specimen was polished for 20 s with a voltage of 28 V and a flow rate of 16, using the LectroPol-5 electropolishing device and the

D2 electrolyte from Struers GmbH. Immediately after electropolishing, the sample was rinsed with 200 ml of deionized water and then ultrasonically cleaned in isopropanol for 10 min. Immediately after drying the sample with an air blower, the first tribological test was performed. The second tribological test was conducted 24 h after electropolishing to allow the native oxide layer to grow and stabilize before the experiment.

3.2 Tribological Experiments

The tribological tests under mild loading conditions were conducted using a reciprocating linear tribometer. The specimen was clamped on a precision linear actuator M-404.2DG from Physik Instrumente (PI) GmbH & Co. KG, Karlsruhe, Germany, and its position was precisely controlled by a C-863 Mercury servo controller from PI. The sample was moved against a fixed sphere without lubricant, as schematically shown in Figure 3.5. During the tribological tests, the frictional force was measured using a piezoelectric, three-axis force sensor, Type Z16758, from Kistler Instrumente AG, and temperature and humidity were continuously recorded using the GIA 2000-AAG010 from Greisinger-Electronic GmbH, Regenstauf, Germany. The sphere was attached to the lever arm of the tribometer using a special specimen holder and a fast-curing two-component epoxy adhesive (Uhu plus instant, Bühl, Germany). When a sapphire sphere was used, it was aligned with the aid of a polarizer and a light source so that its hexagonal close-packed plane was oriented parallel to the contact surface, ensuring consistent conditions in all the tribological experiments. For all experiments, a new sphere was used to avoid chemical interactions or roughness differences from previous tests. The nano-grained and porous samples were mounted in such a way that the tribological experiments could be carried out as shown in Figure 3.6. Before the experiments both the copper specimen and the sphere were exposed to the set humidity for at least 1 h before testing to ensure consistent experimental conditions. Humidity produces a surface hydroxide layer on alumina that has a lower hardness compared to alumina itself and can influence the frictional behavior [123, 124]. Between 40 % and 80 % relative humidity, the hardness values of sapphire, however, exhibit a relatively stable value [125]. Immediately after the test, the specimen was unloaded and stored in a vacuum (< 1 mbar) to prevent further oxidation. To determine the coefficient of friction, an average value was calculated for each cycle over the central 60 % of both strokes, as a constant sliding speed could be assumed in this region.

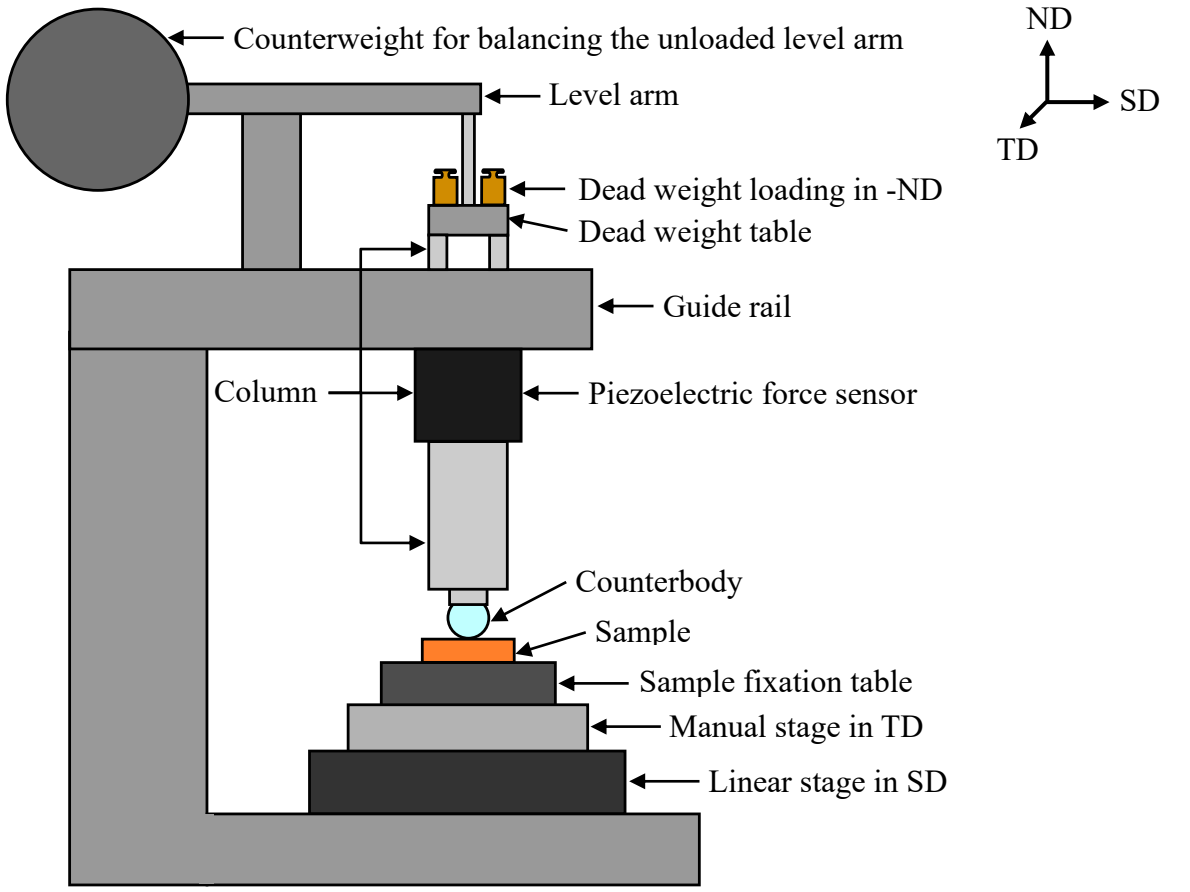

Figure 3.5: Schematic setup of the tribometer used in this study, including the associated coordinate system indicating the normal direction (ND), sliding direction (SD), and transversal direction (TD).

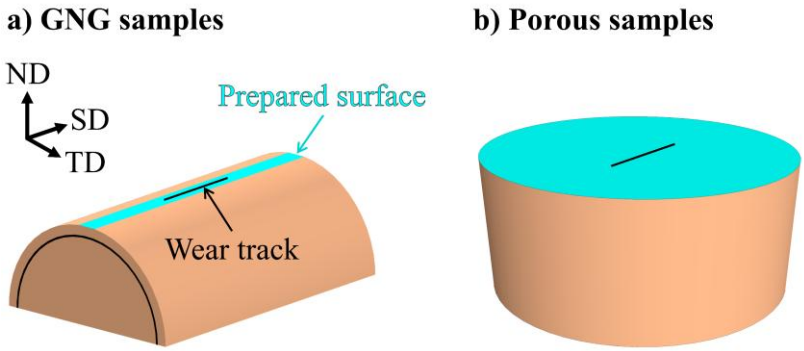

Figure 3.6: Schematic representation of the wear track positions on the a) gradient nano-grained (GNG) and b) porous samples. The tribological tests were conducted parallel to the sliding direction (SD) and orthogonal to both the transverse direction (TD) and the normal direction (ND).

In the tribological experiments conducted under severe loading conditions according to Chen et al. [12], a linear reciprocating SRV5 tribometer from Optimol Instruments Prüftechnik

GmbH, Munich, Germany, was used, equipped with the associated 2disk OCA software package for operation, control, and data evaluation.

The specimens with gradient nano-grained (GNG) microstructures were tested under various tribological conditions. A key distinction in this regard is that, while GNG-0(Chen), GNG-30(Chen), and GNG1-60 were tested under severe tribological loading conditions with a normal load of 30 N and a sliding speed of 10 mm s^{-1}, GNG2-160 and GNG2-10 were examined under mild tribological loading conditions with a normal load of 2 N and a sliding speed of 0.5 mm s^{-1}. All tests conducted under severe loading conditions in this study were performed with a stroke of 1 mm, whereas those under mild conditions had a stroke of 6 mm. The severe tribological loading conditions with a stroke of 1 mm were based on the tests by Chen et al. [12], who demonstrated friction reduction for GNG-0(Chen) and GNG-30(Chen) under these conditions. To verify whether the surface mechanical grinding treatment (SMGT) applied in this study produces GNG microstructures with the desired friction reduction effect, GNG1-60 was also tested under severe conditions. This enabled a systematic comparison between mild and severe testing conditions and an analysis of the influence of different GNG microstructures on friction performance. Due to the limited number of samples available, all experiments were conducted once. The symbols presented in Table 3.2 are used in the following to distinguish between the different tribological test conditions.

Table 3.2: Summary of the tribological testing conditions applied to various sample types. GNG-0(Chen) and GNG-30(Chen) are reference samples from Chen et al. [12].

Sample type	Tribological test parameters
GNG-0(Chen) **GNG-30(Chen)** **GNG1-60**	**Severe conditions:** **Normal load:** 30 N **Sliding speed:** 10 mm s^{-1} **Stroke:** 1 mm **Cycle numbers:** GNG-0 and GNG-30: 6000; GNG1-60: 7500 **Counterbody:** WC-Co, diameter: 10 mm **Environment:** air, 45 % RH, 22 °C
GNG2-160 **GNG2-10** **Porous samples:** **(FSP, FBP, MSP, MBP, FSPC, FBPC)**	**Mild conditions:** **Normal load:** 2 N **Sliding speed:** 0.5 mm s^{-1} **Stroke:** 6 mm **Cycle numbers:** 1000 **Counterbody:** Sapphire, WC-Co (GNG2-10), diameter: 10 mm **Environment:** air, 50 % RH, 22 °C

In all experiments on the porous specimens, the mild conditions from Table 3.2 were applied, meaning a sapphire sphere was used as the counterbody, and a normal force of 2 N was applied to the specimen using a dead weight. Each stroke covered a sliding distance of 6 mm at a speed of 0.5 mm s^{-1}, and two strokes constituted one complete cycle. The experiments were conducted at room temperature in a closed chamber where a relative humidity of 50 % was maintained. For all vibropolished specimen types and the electropolished sample, 1000 cycles were performed. In order to investigate the long-term behavior, chemical-mechanical vibropolished samples with few small pores (FSP), many small pores (MSP) and many big pores (MBP) were additionally exposed to 5000 cycles. To ensure comparability between the specimens, and since Figure 3.7 shows that the distribution of sintering pores differs between the center and the edge of the samples, all tribological experiments as well as the

microstructure analyses were carried out in the center, where porosity is lower. To verify the reproducibility of the results, the 1000-cycle experiments for the different vibropolished specimen types and analyses were conducted twice.

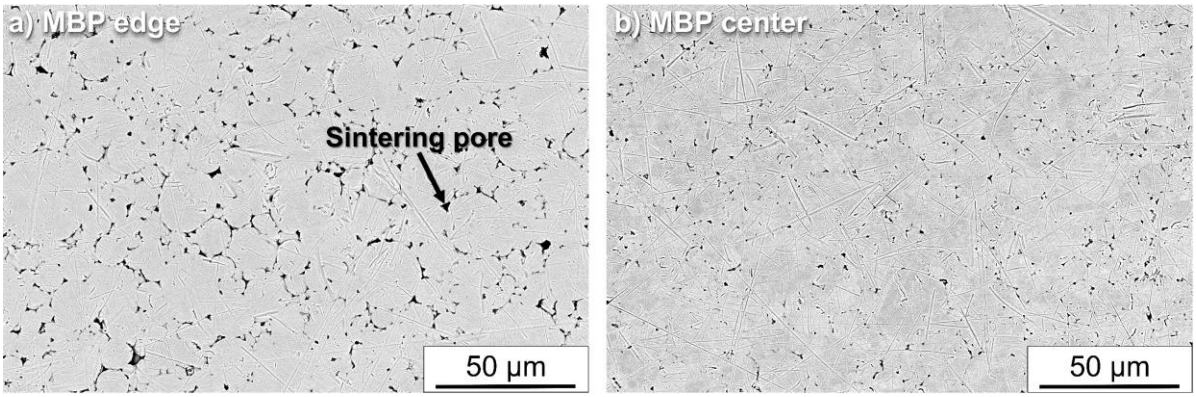

Figure 3.7: SEM images of a vibro-polished surface, which lays perpendicular to the current flow during the field assisted sintering process, taken a) at the edge and b) in the center of a specimen with many big pores (MBP) [122].

3.3 Sample Characterization

The characterization methods used in this work were aimed at both investigating the processing-induced microstructures and analyzing the changes caused by tribological loading in terms of surface topography and the microstructure beneath the surface. Due to the small dimensions of the generated tribo-oxides and deformation zones, high lateral resolution was required, which is why the microstructure analysis was conducted using SEM. To ensure that the analyzed area was exposed to constant sliding speeds, the analysis was performed in the center of the wear tracks.

Microstructure Analysis. The microstructures of the copper specimens were analyzed after the tribological experiments. For this, cross-sections were prepared using the DualBeam Helios NanoLab 650 from FEI, ThermoFisher Scientific, Waltham, Massachusetts, United States, with a FIB and subsequently examined through SEM imaging. The cross-sections were prepared both parallel to the sliding direction within the wear track and adjacent to the track. Before the cutting process, two platinum layers were applied to the specimen surface, the first one using the electron beam and the second one with the ion beam, to protect the surface from damage by gallium ions. The subsequent imaging was performed using the through-the-lens

detector with an acceleration voltage of 2 kV and a beam current of 0.8 nA. The immersion mode was used, in which an electromagnetic field is generated to enhance the resolution. Due to process-induced distortions, a slight beam rotation of less than 1° was sometimes necessary to align the specimen surface horizontally for the images. To determine the manufacturing-induced pore size and pore fraction, two cross-sectional images per specimen were analyzed. For this, the sintering pores were first manually colored using the software Inkscape (Inkscape Community, Boston, Massachusetts, United States) due to the partial low contrast difference between the sintering pores and the solid material. Using ImageJ (NIH, Bethesda, Maryland, United States), the edited images were then inverted into binary images, allowing for the determination of both the average pore size and the porosity. To calculate the average grain size of the gradient nano-grained (GNG) specimens, the line intercept method was applied [126]. The process-induced tilt angle of the specimens during imaging, which was 52°, was taken into account, and the measured values were accordingly corrected to the true length.

Density Measurement. In addition to the local determination of the porosity, the total density of the specimens was measured using the Archimedes method. For this, the specimens were first weighed both in air $m_{S(A)}$ and in deionized water $m_{S(W)}$ using a precision balance, type R160P-*D1 from Sartorius AG, Göttingen, Germany. After a stabilization time of 5 min, the measurements were recorded. To ensure higher reliability of the results, the measurements were repeated three times, and the average was used for analysis. In the calculation, the corresponding water density ρ_W was considered based on the measured water temperature, and an air density ρ_A of 0.0012 g cm^{-3} was used, in accordance with ISO 15212-1:1998 [127, 128]. Based on the absolute density of the specimens

$$\rho_S = (m_{S(A)} / (m_{S(A)} - m_{S(W)})) \cdot (\rho_W - \rho_A) + \rho_A \qquad \text{Equation 4}$$

and with the absolute density of copper being 8.96 g cm^{-3}, the relative density could be calculated. To obtain reliable values for the determination of water density, the thermometer was immersed in the water 2 h prior to the measurements, and the temperature was recorded immediately before the measurement in water [129].

Surface Characterization. The analysis of the specimen surfaces was conducted using several methods. Light microscopy images were taken using the BX60 from Olympus, Tokyo,

Japan, while SEM and electron backscatter diffraction (EBSD) imaging were performed using the DualBeam Helios NanoLab 650. For the determination of local porosity differences, secondary electron images were taken using the in-lens electron detector at an acceleration voltage of 2 kV and a beam current of 0.8 nA, both at the edge and in the center of the specimen. For the analysis of the wear tracks, both secondary electron and backscattered electron images were obtained using the circular backscatter detector at 15 kV and 6.4 nA. The grain orientation in the center of the specimen was determined using EBSD imaging. The scans were performed with a surface tilt of 70°, a beam current of 13 nA and an acceleration voltage of 20 kV. When measuring the surface of the specimen with many big pores (MBP), a magnification of 250 and a step size of 1 µm were employed, whereas for the sample with few big pores (FBP), a magnification of 500 and a step size of 250 nm were chosen. The indexing rate for both specimens was approximately 50 %. The MATLAB toolbox MTEX was used for data analysis, which creates a color-based map based on the pole figures of the {100}, {110} and {111} directions [130].

In addition, the surface profiles of the wear tracks were obtained from optical surface profilometry images. While the wear tracks of the chemical-mechanical vibropolished porous specimens after 1000 cycles were measured with the optical surface profilometer Plµ Neox from Sensofar, Barcelona, Spain, the chemical-mechanical vibropolished surfaces, the wear tracks after 5000 cycles, the electropolished specimen and the GNG samples were measured with TopMap Micro.View+ from Polytec GmbH, Waldbronn, Germany, using a 10x magnification objective from Nikon, Tokyo, Japan. The wear track images were acquired at the center of each track. The height profiles of the various wear tracks shown in this study represent the average values along the sliding direction over a distance of 0.9 mm, and are plotted along the width of the wear track. The roughness values of the GNG samples were determined along a height profile line, firstly to enable direct comparison with the results of Chen et al. [12], in which the *Ra* value was also measured along a profile line, and secondly because the GNG specimens have a cylindrical geometry that would require surface corrections, which can be prone to error. The arithmetic mean height

$$Ra = 1/l_e \int_0^{l_e} |z(x)| \, dx \qquad \text{Equation 5}$$

was determined along the evaluation length l_e using the height values $z(x)$ of the examined scale-limited profile, according to ISO 21920-2:2021 [131]. A Gaussian high-pass cut-off filter was applied, with the cut-off wavelength selected according to the criteria specified in ISO 4288:1996 [132], to minimize long-wavelength components such as waviness and form deviations. This allowed for isolating the short-wavelength roughness features and ensured an accurate, norm-compliant evaluation of the surface roughness.

In case of the porous specimens, the surface roughness was calculated using the arithmetic means of the height, given by

$$Sa = 1/A \iint |z(x,y)| \, dx dy \qquad \text{Equation 6}$$

using the ordinate values $z(x,y)$ within the evaluation area A, according to ISO 25178-2:2021 [133].

Microhardness. The surface hardness measurements of the various sample types were performed using a FISCHERSCOPE® H100 from Helmut Fischer GmbH, Sindelfingen, Germany, equipped with a Vickers indenter. A test load of 250 mN was applied, and five indentations were made per sample. The measured Vickers hardness was subsequently converted into hardness in GPa by multiplying it with 0.009807, based on the definition of standard gravity in SI units [134].

4 Results

The results section of this work is divided into two parts. Section 4.1 investigates the gradient nano-grained (GNG) samples produced by the surface mechanical grinding treatment (SMGT) and examines their tribological performance, whereas section 4.2 examines the porous field assisted sintered (FAST) samples, focusing on their friction and wear behavior. First, the porous samples are characterized, and their tribological behavior after 1000 and 5000 cycles is evaluated. Subsequently, the effect of surface treatments on highly porous samples and their impact on the tribological behavior is investigated.

4.1 GNG Samples

4.1.1 Sample Microstructure

The cross-sectional images illustrated in Figure 4.1 depict the microstructures of the different GNG samples produced in this study, taken directly after SMGT processing and prior to surface preparation for tribological testing, which involves grinding, polishing, and electropolishing. It becomes evident that the different manufacturing approaches listed in Table 3.1 used for the two specimens resulted in GNG layers of varying thickness. The GNG1 sample shown in Figure 4.1a) exhibits a GNG layer depth of approximately 350 µm, while the GNG2 in Figure 4.1b) shows a GNG depth of around 800 µm. Similar to GNG-0(Chen), grain sizes of around 300 nm were observed at a depth of 150 µm in GNG2, with some grains reaching up to 700 nm.

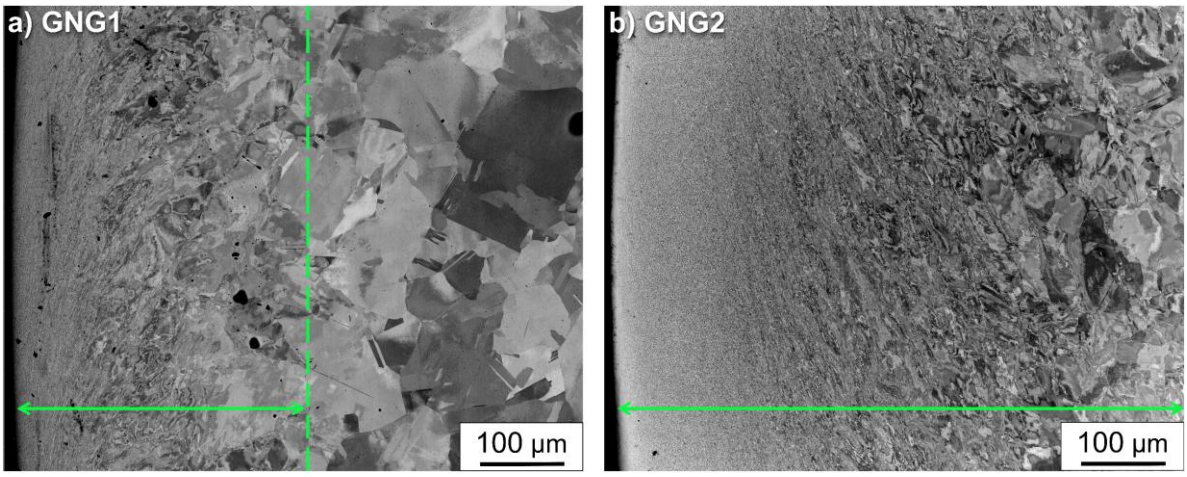

Figure 4.1: BSE images of the cross-sectional microstructures of a) GNG1 and b) GNG2 after surface mechanical grinding treatment and before surface post-treatment. The deformation depth is indicated in green, which in b) is greater than the displayed image section.

The microstructures of the sample types displayed in Figure 4.2 were obtained after surface post-treatment following the SMGT process. While the grains within the uppermost 5 µm beneath the surface had an average size of 617 nm in GNG1-60 (60 µm surface removal), they measured 282 nm in GNG2-160 (160 µm surface removal) and 116 nm in GNG2-10 (10 µm surface removal). In GNG2-10, grain sizes below 30 nm and up to 300 nm could be detected beneath the surface.

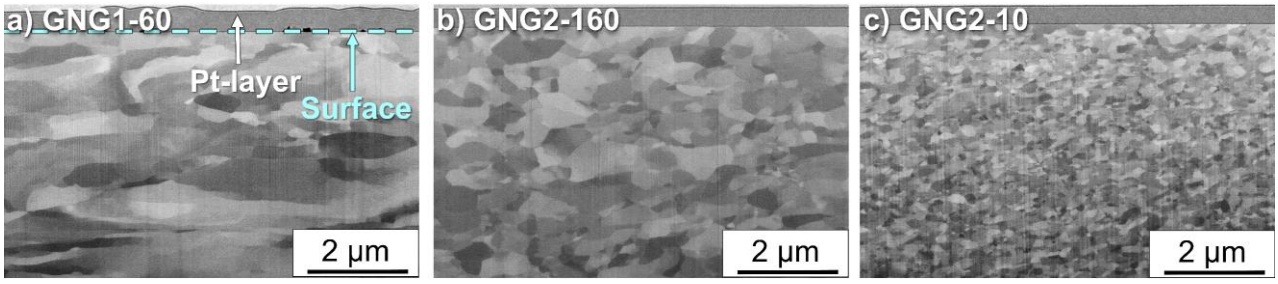

Figure 4.2: SEM cross-sectional images of a) GNG1-60, b) GNG2-160 and c) GNG2-10. The value following the hyphen in the specimen's name indicates the amount of surface removal after SMGT.

The roughness measurements of the different specimens after the various preparation steps, summarized in Table 4.1, indicate that the additional surface treatments after the SMGT process reduced the surface roughness. The surface of the GNG2 specimen is exemplarily shown by profilometry images in Figure 4.3. The observed grooves, appearing as surface waviness, resulted from the forward motion of the sphere in combination with the rotation of the copper rod during SMGT. An additional grinding and mechanical polishing step before electropolishing generated a planar surface and further reduced the surface roughness. GNG1 exhibited a lower surface roughness after the SMGT process than GNG2 and showed a comparable roughness value to GNG2 after the additional surface post-treatment.

Table 4.1: Overview of roughness values for the gradient nano-grained (GNG) surfaces across different sample types following surface mechanical grinding treatment (SMGT) and subsequent additional surface treatments. The data of the GNG surfaces are taken from Chen et al. [12, 29].

Sample type & Surface treatment	**Surface roughness *Ra***
GNG [12, 29]	
SMGT	0.20 µm
SMGT + electropolished: **GNG-0(Chen)**	0.03 µm
SMGT + ground + polished + electropolished: **GNG-30(Chen)**	0.03 µm
GNG1	
SMGT	0.13 µm ± 0.01 µm
SMGT + ground + polished + electropolished: **GNG1-60**	0.07 µm ± 0.01 µm
GNG2	
SMGT	1.07 µm ± 0.01 µm
SMGT + electropolished	0.20 µm ± 0.01 µm
SMGT + ground + polished + electropolished: **GNG2-160, GNG2-10**	0.07 µm ± 0.01 µm

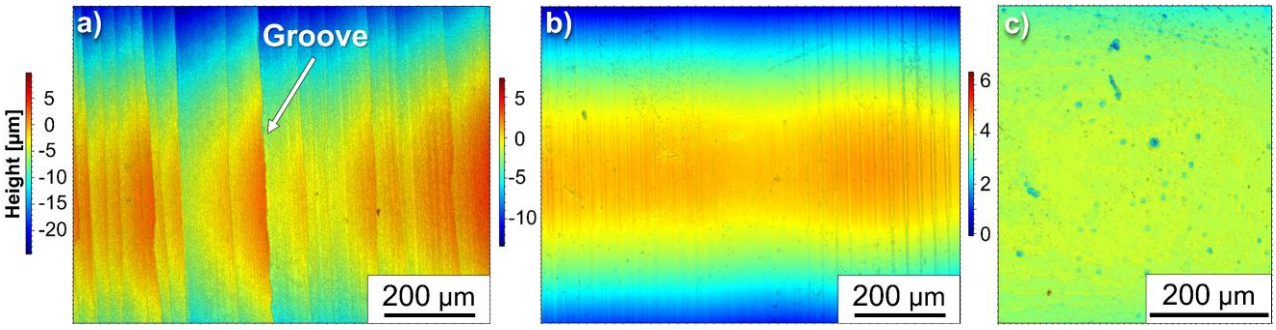

Figure 4.3: Surface profilometry images of the GNG2 sample after different processing steps: a) directly after surface mechanical grinding treatment (SMGT), b) after SMGT and electropolishing, and c) after SMGT, grinding (removal of 10 µm of the surface layer), polishing, and electropolishing, representing the GNG2-10 microstructure.

Microhardness measurements of the different samples after SMGT processing and subsequent surface treatments, are shown in Figure 4.4. Chen et al. [12] reported an average microhardness of 1.8 GPa for the GNG structure. After removal of the top 20-30 µm nano-grained (NG) layer, which corresponds to the GNG-30(Chen) structure, the hardness was reduced to 1.4 GPa. The GNG1-60

microstructure produced in this study exhibited a mean microhardness of 1.5 GPa, compared to 1.7 GPa for GNG2-160 and 3.0 GPa for GNG2-10. While the GNG2-160 showed a comparable hardness to GNG-0(Chen), the mean hardness of GNG2-10 was more than 1.5 times higher than that of GNG-0(Chen). For comparison, the untreated coarse-grained (CG) microstructure inside the sample, with a grain size of around 20 µm, exhibited a mean microhardness of 0.7 GPa [12].

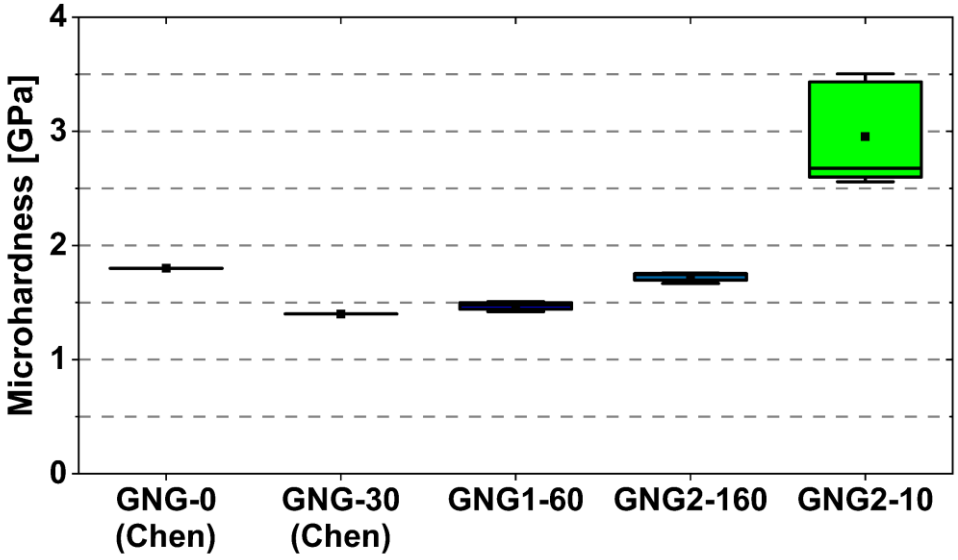

Figure 4.4: Microhardness measurements of the different surface mechanical grinding treated (SMGT) specimens. The mean values for GNG-0(Chen) and GNG-30(Chen) were taken from Chen et al. [12]. The value following the hyphen in the specimen's name represents the amount of surface removal after SMGT. The box indicates the interquartile range from the first to the third quartile, with the median shown as a line. Whiskers extend to values within 1.5 times the interquartile range, while the mean is represented by a square.

4.1.2 Friction and Wear Behavior

The coefficients of friction of the different GNG sample types also demonstrated distinct behaviors. It is important to note that the tribological tests for the GNG2 sample were conducted under mild loading conditions with a normal force of 2 N, a sliding speed of 0.5 mm s^{-1}, a stroke length of 6 mm, and a sapphire sphere as counterbody. In the case of GNG2-10, tests were performed with both a sapphire sphere and a WC-Co sphere as counterbodies. In contrast, the GNG1 and GNG samples were tested under severe tribological loading conditions, meaning with a normal force of 30 N, a sliding speed of 10 mm s^{-1}, a stroke length of 1 mm, and a WC-6Co counterbody. Since Chen et al. [12] have shown that the GNG microstructures exhibit low coefficients of friction under severe loading conditions, the differences in tribological testing conditions in this study allow for analysis

of both the influence of GNG microstructures and the impact of testing conditions on tribological behavior.

The coefficient of friction of the samples tested under severe tribological loading conditions are shown in Figure 4.5. For both GNG-30(Chen) and GNG1-60, the coefficients of friction increased continuously throughout the tribological experiments. For GNG-30(Chen), the coefficient rose to 0.43 within the first 400 cycles and then increased gradually, reaching a value of 0.53 by cycle 6000. GNG1-60 reached a coefficient of 0.30 within the first 60 cycles and then increased to 0.50 by cycle 7500. Despite the different progression patterns, both specimens reached similar coefficients of friction values by the end of their respective experiments. In contrast, GNG-0(Chen) behaved differently. The coefficients increased rapidly within the first few cycles and then remained nearly constant around a value of 0.37 throughout the entire test duration.

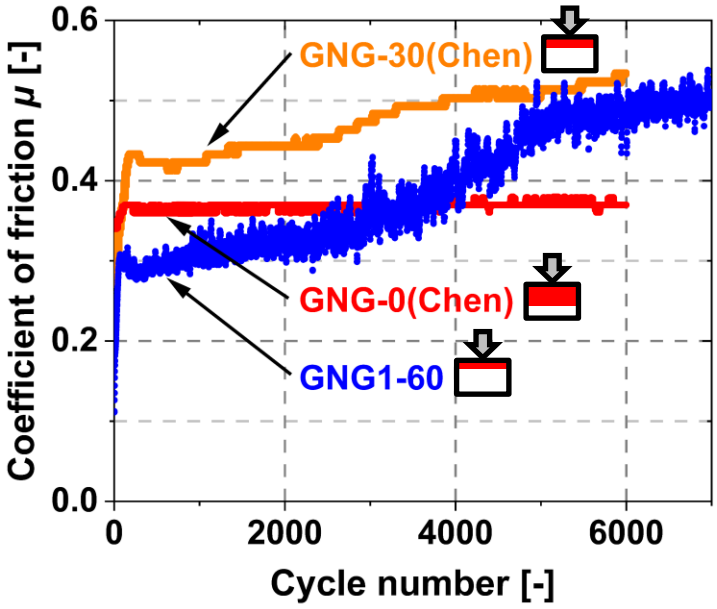

Figure 4.5: Evolution of the coefficient of friction of differently processed gradient nano-grained (GNG) samples tested under varying tribological conditions. In the symbols the red area indicates the thickness of the GNG layer for each sample type. The experiments were conducted using a normal load of 30 N, a sliding speed of 10 mm s^{-1}, and a stroke of 1 mm with a WC-6Co sphere as counterbody. The values for GNG-0(Chen) and GNG-30(Chen) were taken from Chen et al. [12].

Figure 4.6 illustrates how increasing surface removal depth, as well as the counterbody material affect the coefficient of friction in mild tribological loading conditions. For the GNG2-160 sample, where 160 µm of the surface was removed, a high coefficient of friction of 0.6 was reached within the first 50 cycles. The coefficient of friction remained relatively stable thereafter, reaching a value

of 0.61 by cycle 1000. In contrast, the GNG2-10 sample, with a surface removal of only 10 µm, showed a slower increase of the coefficient of friction, reaching values of 0.58 and 0.50 after approximately 240 cycles. Two GNG2-10 samples were tested under identical tribological conditions, differing only in the counterbody material. One used a sapphire and the other a WC-6Co sphere. In both cases, the increase in the coefficient of friction was slower compared to GNG2-160. The sample tested with the sapphire sphere exhibited a steeper rise within the first 200 cycles but stabilized at 0.53 by cycle 1000, whereas the WC-6Co counterpart resulted in a final value of 0.58. Since the GNG2-10 samples showed similar behavior regardless of the counterbody, the following analysis focuses on the one tested with the sapphire sphere.

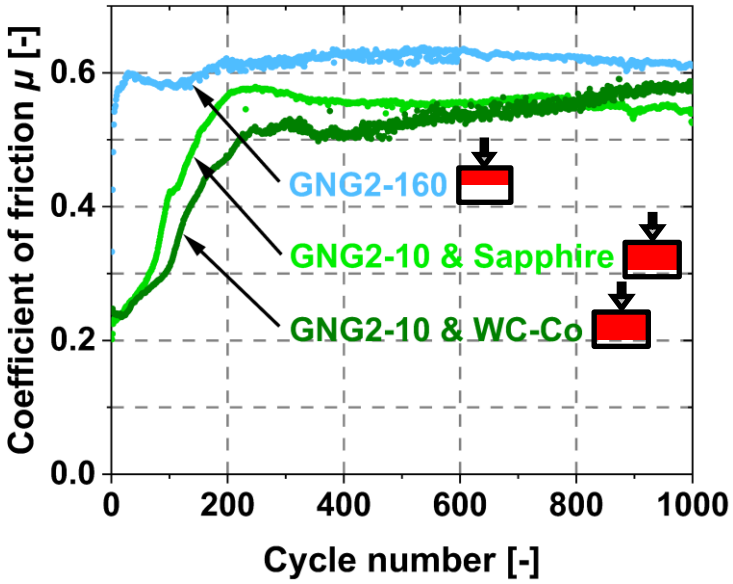

Figure 4.6: Coefficients of friction of the GNG2 sample under mild tribological loading conditions, using a normal load of 2 N, a sliding speed of 0.5 mm s^{-1}, and a stroke length of 6 mm with a sapphire or a WC-6Co sphere as the counterbody. The red area in the symbols indicates the thickness of the GNG layer for the different sample types.

Based on the profilometric images of the wear tracks shown in Figure 4.7, it is evident that GNG2 exhibited a different wear behavior compared to GNG1. This can be attributed to the differing test conditions presented in Table 3.2. GNG1-60 showed a wear track width of approximately 200 µm, accompanied by asymmetric pile-ups of approximately 3 and 25 µm in height on the respective sides. Additionally, the wear track of GNG1-60 appeared significantly smoother than that of GNG2. It should be noted that for GNG1-60, the initial surface level was difficult to determine and therefore had to be roughly estimated, as the wear track was as wide as the prepared area, and the surrounding surface dropped off due to the cylindrical shape of the sample. GNG2-10 and GNG2-160 exhibited

similar wear behavior, with wear track widths of around 150 and 200 µm, respectively, and less pronounced pile-ups at the sides compared to GNG1-60. The wear tracks did not exhibit pronounced pile-up along the edges. Instead, they displayed an irregular, rough surface that rose above the initial surface plane.

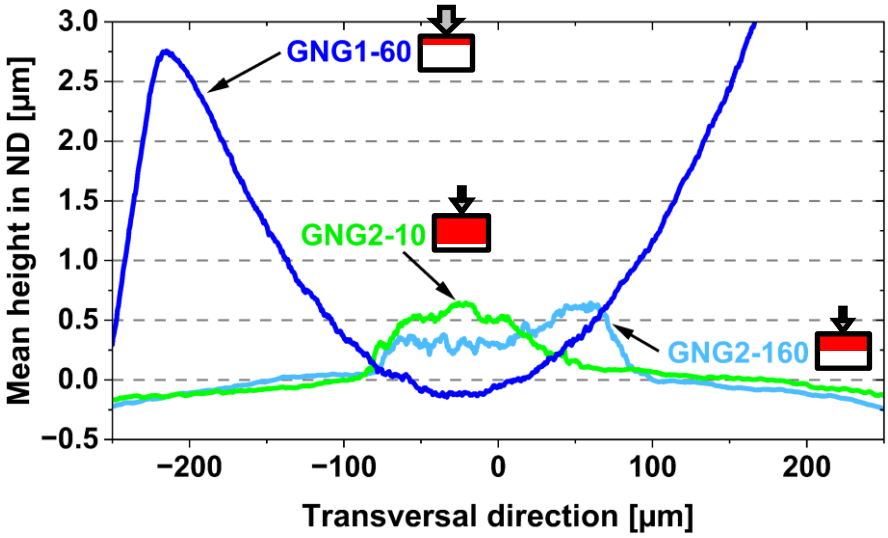

Figure 4.7: Surface profilometric images of different specimen types after the tribological experiments. While GNG1-60 was tested with a normal load of 30 N, a sliding speed of 10 mm s^{-1}, a stroke of 1 mm and a WC-6Co sphere as the counterbody, GNG2-160 and GNG2-10 were tested with a normal load of 2 N, a sliding speed of 0.5 mm s^{-1}, a stroke of 6 mm and a sapphire sphere as the counterbody. The red area in the symbols represents the thickness of the GNG layer for the different sample types.

Light microscopy images in Figure 4.8 reveal that the pile-ups in GNG1-60 consisted of fringe-like accumulations rather than compact, continuous ridges. The GNG1 surface appeared smooth and reddish, whereas the GNG2 surfaces were darker and showed signs of delamination and debris along the wear track edges. No obvious difference was observed between the tribologically tested GNG2-10 and GNG2-160 surfaces. Grooves along the sliding direction (SD) were present in all wear tracks.

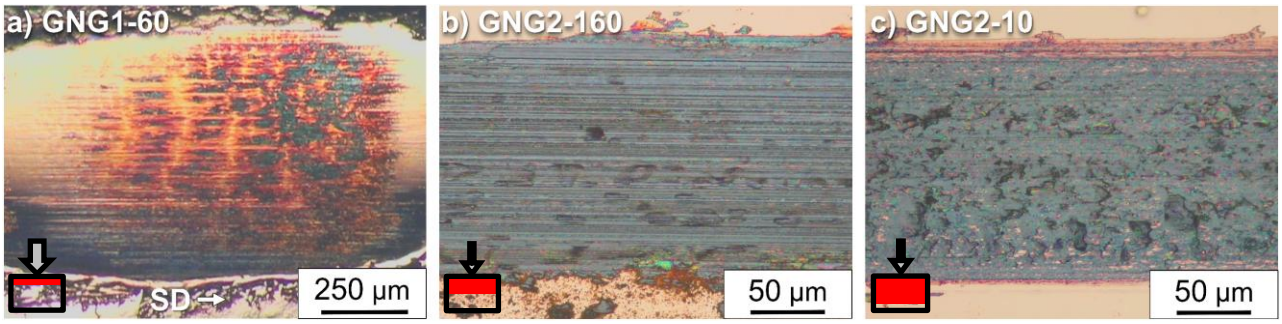

Figure 4.8: Light microscopy images of the wear tracks of a) GNG1-60, b) GNG2-160, and c) GNG2-10. The red area in the symbols indicates the GNG layer thickness for the different sample types.

Clear differences between the wear tracks of GNG1-60 and those of GNG2-160 and GNG2-10 are evident in the SEM images shown in Figure 4.9. GNG1-60 exhibited pronounced pile-ups along the sides and a relatively smooth wear track surface. In contrast, the surfaces of GNG2-160 and GNG2-10 showed significant delamination across the entire width of the wear track, without pronounced pile-ups at the edges.

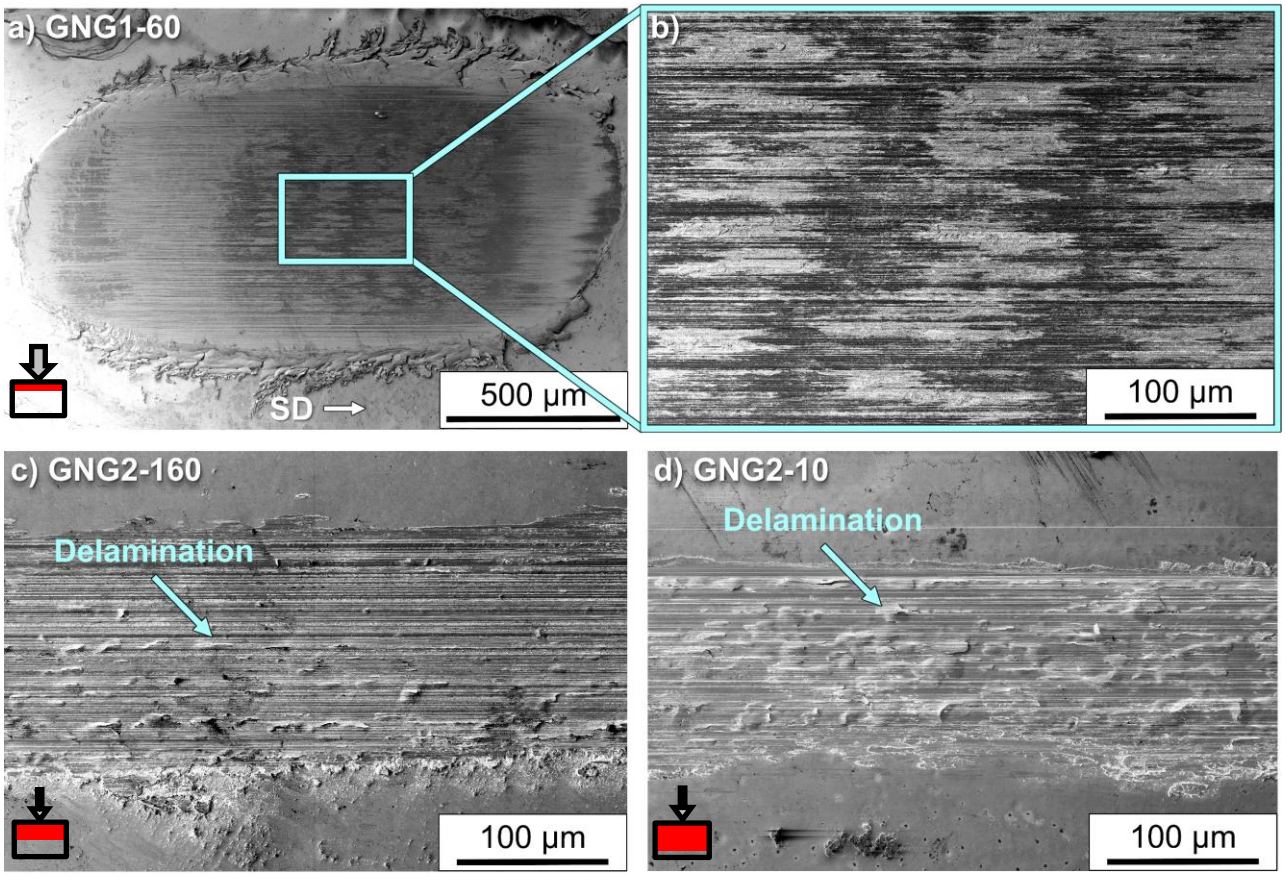

Figure 4.9: SEM images of the wear tracks of GNG1-60 in a) and b), GNG2-160 in c), and GNG2-10 in d) after the respective tribological experiments. The white arrow indicates the sliding direction (SD) in all images. The GNG layer thickness for the different sample types is indicated by the red area in the symbols.

The effects of the tribological experiments on the microstructures can be identified by comparing SEM cross-section images taken before testing in Figure 4.2 and Figure A.1 in the Appendix and after testing in Figure 4.10. The grain size analysis within the top 6.3 µm below the surface of the different specimens before tribological testing, presented in Figure 4.2, reveals that GNG1-60 exhibited an average grain size of 0.62 µm, GNG2-160 of 0.28 µm, and GNG2-10 of 0.12 µm. Figure 4.10 illustrates that the tribological loading under the different conditions altered the microstructure of GNG1-60 to a depth exceeding 31.7 µm, while in GNG2-160 and GNG2-10 the tribologically

induced deformation layer (DL) only affected approximately 11.0 and 4.4 µm, respectively. Figure 4.10a) shows that, during the tribological experiment, the grain morphology in GNG1-60 became elongated in vertical direction towards certain spots at the surface. As seen in Figure 4.10b), the grains were also coarser than in the original subsurface microstructure, with sizes of approximately 0.35 µm. Additionally, regions with numerous small black, circular features and refined microstructural features (F0) were observed both at the surface and at various depths down to 21.6 µm below the sample surface. In contrast, the microstructure of GNG2-160 and GNG2-10, shown in Figure 4.10c) to f), exhibited coarser grains in the DL, along with a slight elongation of the grain morphology in the sliding direction. The average grain size of 0.31 µm beneath the surface of GNG2-10 was similar to that observed in GNG1-60, whereas significantly larger average grain sizes of 0.56 µm were found in GNG2-160. Furthermore, larger black, circular features than in GNG1-60, as well as black, elongated features (F2), were visible directly beneath the surface of GNG2-160 and GNG2-10. Both features were found in a darker, uniformly gray region (F1) reaching depths of up to 2.5 µm in GNG2-160 and 1.8 µm in GNG2-10, contrasting with the surrounding grains.

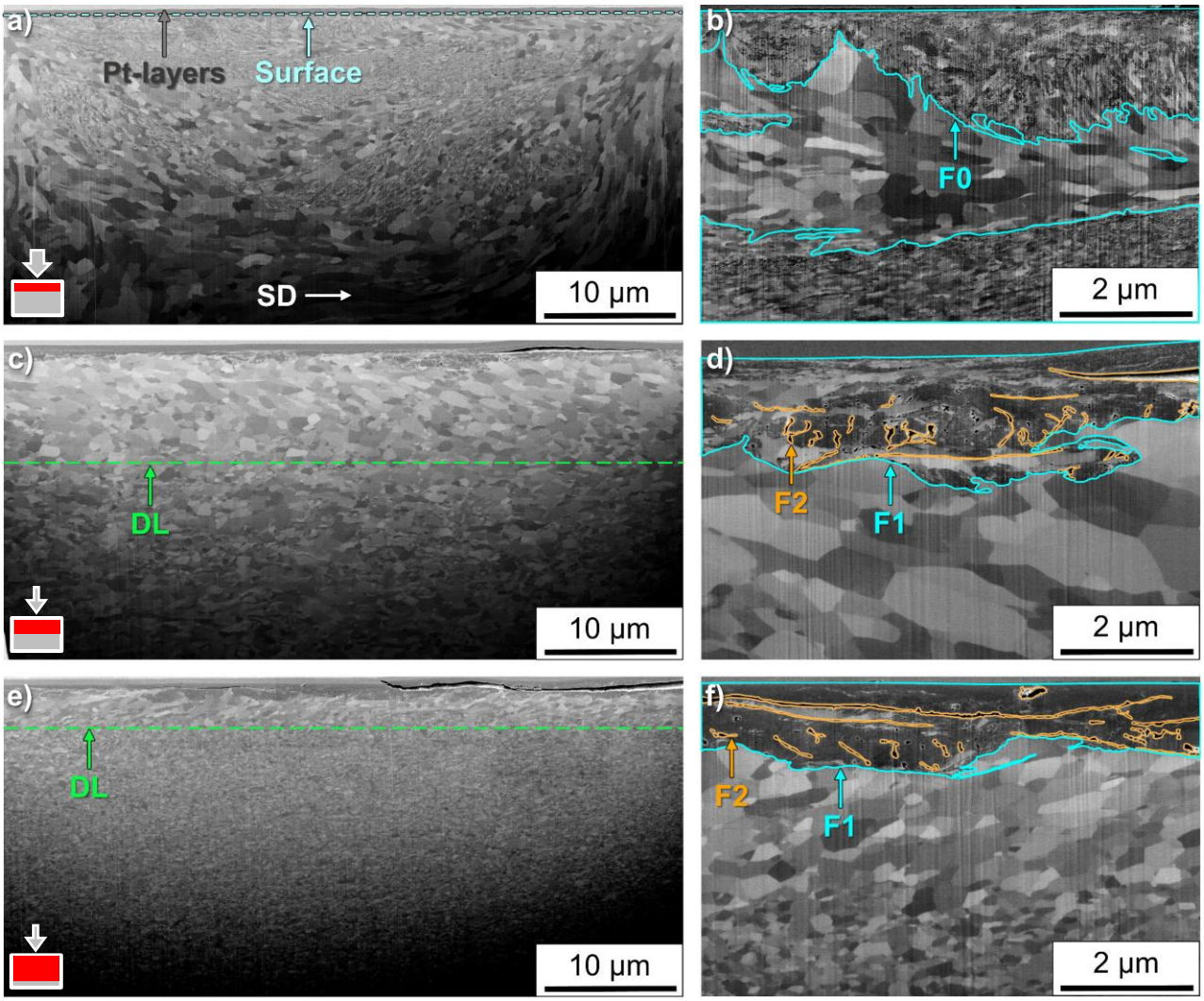

Figure 4.10: SEM images of cross-sections taken along the sliding direction (SD) in the middle of the wear tracks of GNG1-60 in a) and b), GNG2-160 in c) and d), and GNG2-10 in e) and f). The GNG layer thickness of the samples is represented by the red area in the symbols. The sliding direction (SD) shown in a) is valid for all images. In a), the specimen surface is marked beneath the protective platinum layers, which applies to all images.

4.2 Porous Samples

The following results in sections 4.2.1 and 4.2.2 have been previously submitted by Lung et al. [122] while those in sections 4.2.3 to 4.2.5 have been published by Lung et al. [135].

4.2.1 Sample Microstructure

For the field assisted sintering technology (FAST) samples, pore analysis was conducted by measuring the overall density using the Archimedes method, while the local density in the center of the specimens was determined by image analysis of FIB cross-sections, as summarized in Table 4.2.

Both Table 4.2 and the SEM images in Figure 3.7 illustrate that the porosity was more pronounced at the edges of the specimens than in the center. Surface appearances and microstructures of the various sample types are shown in Figure A.2 and Figure A.3 in the Appendix.

Table 4.2: Comparison of the overall relative density of the different specimens, some of which were additionally cold isostatically pressed (CIP), with the porosity measured in the center of the specimens [122].

Sample type	Relative density [%]	Porosity in the center [%]
Few Small Pores (FSP)	96.7	1.6
Few Big Pores (FBP)	94.7	3.1
Many Small Pores (MSP)	84.8	7.3
Many Big Pores (MBP)	85.6	5.4
Few Small Pores + CIP (FSPC)	97.7	0.7
Few Big Pores + CIP (FBPC)	96.4	1.5

The samples produced with the finer powder exhibited smaller pore areas, as shown in Figure 4.11, and a higher number of pores compared to those generated with the coarser powder. Using the finer powder, a reduction in average pore area of 1.9 μm^2 could be achieved for fewer sintering pores, while a reduction of 2.8 μm^2 could be attained for many sintering pores. Applying a lower force of 5 kN instead of 15.7 kN during the FAST process resulted not only in an increase in pore area by 2.2 μm^2 for the finer powder and 3.1 μm^2 for the coarser powder, but also in an increase in porosity by 5.7 % for the finer powder and 2.3 % for the coarser powder. An additional cold isostatic pressing (CIP) step led to a reduction in pore area by 0.4 μm^2 and porosity by 0.8 % for the samples generated with the finer powder, and a reduction in pore area by 1.7 μm^2 and porosity by 1.6 % for the specimens made with the coarser powder.

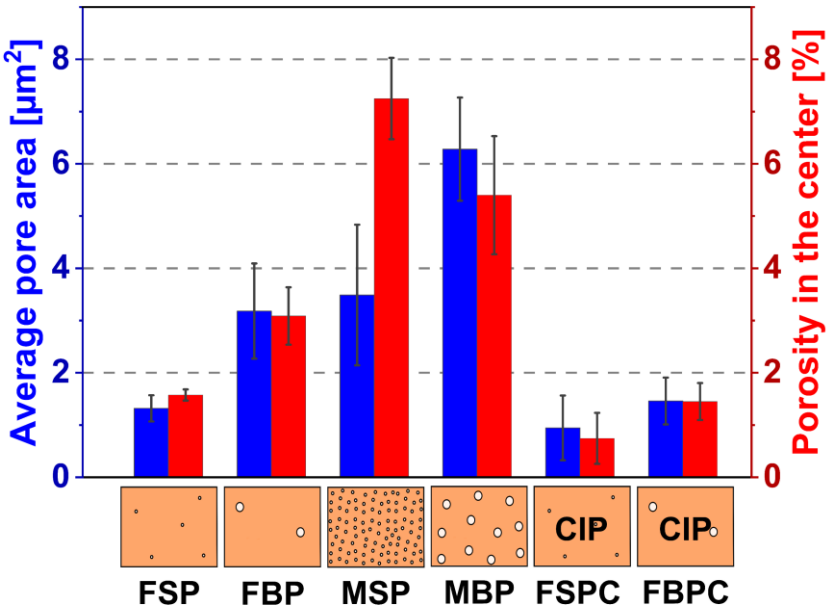

Figure 4.11: Average pore area and porosity measured in FIB cross-sections in the center of the different specimen types with varying size and number of pores as represented by the symbols [122]. CIP refers to specimens that were additionally cold-isostatically pressed.

In order to determine whether a possible anisotropy of the grain orientations needed to be considered in the tribological experiments and in the comparability of the results of the different specimen types, EBSD scans were performed. The orientation distribution functions generated from pole figures in Figure 4.12 illustrate the grain orientation on the specimen surface, taken from a central section of the sample containing many big pores (MBP). They reveal that no significant anisotropy in grain orientation was present, since the maximum frequency of occurring clusters was around 5.0 %. Similarly, no significant anisotropy of grain orientation could be observed in FBP either, with a maximum cluster frequency of approximately 3.5 % visible in the orientation distribution functions in Figure A.4. Thus, sintering at both low and high forces did not cause substantial anisotropy in grain orientations. Consequently, no manufacturing-induced crystal orientation anisotropy needed to be considered when conducting the tribological tests, ruling out crystallographic orientation as a confounding variable and strengthening the conclusion that the observed effects are driven by the sintering pores.

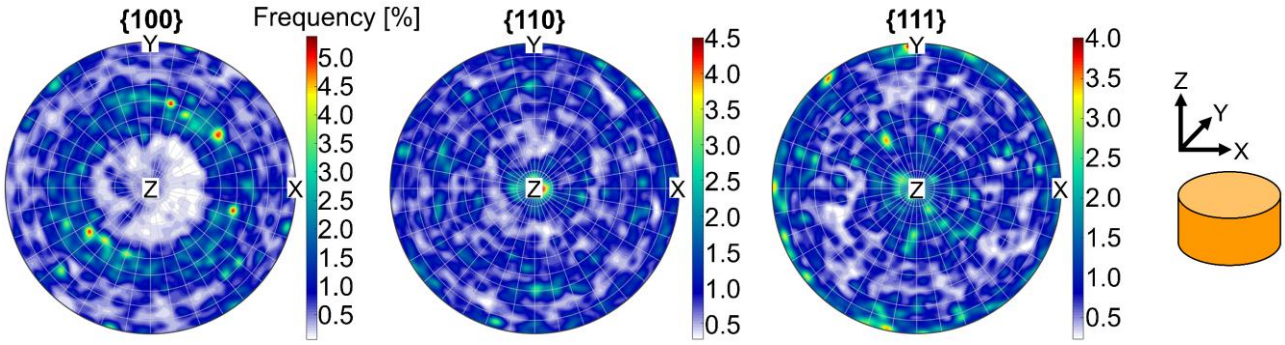

Figure 4.12: Orientation distribution functions derived from pole figures, showing the frequency of surface grain orientations for a specimen with many big pores in the {100}, {110}, and {111} crystal orientations, with the X and Y directions lying within the specimen surface plane, and the Z direction oriented perpendicular to it [122].

The surface roughness values of the different specimen types after vibropolishing are summarized in Table 4.3. It can be observed that the surface roughness of the different sample types increased with porosity. The microhardness measurements of the vibropolished samples shown in Figure 4.13 indicate that the sample with few small pores (FSP) displayed a hardness of 0.67 ± 0.04 GPa, whereas the specimen with few big pores (FBP) had a hardness of 0.61 ± 0.06 GPa. The samples with many small pores (MSP) and MBP exhibited lower hardness values, with MSP showing a hardness of 0.48 ± 0.01 GPa and MBP of 0.40 ± 0.04 GPa. The CIP treatment carried out after the FAST process resulted in increased hardness values in the specimens with few pores. Thus, FSPC exhibited a hardness of 0.74 ± 0.02 GPa, while FBPC showed a hardness of 0.92 ± 0.08 GPa. The size ratio between sintering pores and the indenter is exemplified on an FBP specimen in Figure A.5.

Table 4.3: Surface roughness of the vibropolished porous specimens, including the additionally cold-isostatically pressed (CIP) ones.

Sample type	**Surface roughness *Sa***
Few Small Pores (FSP)	0.05 µm
Few Big Pores (FBP)	0.06 µm
Many Small Pores (MSP)	0.11 µm
Many Big Pores (MBP)	0.07 µm
Few Small Pores + CIP (FSPC)	0.04 µm
Few Big Pores + CIP (FBPC)	0.04 µm

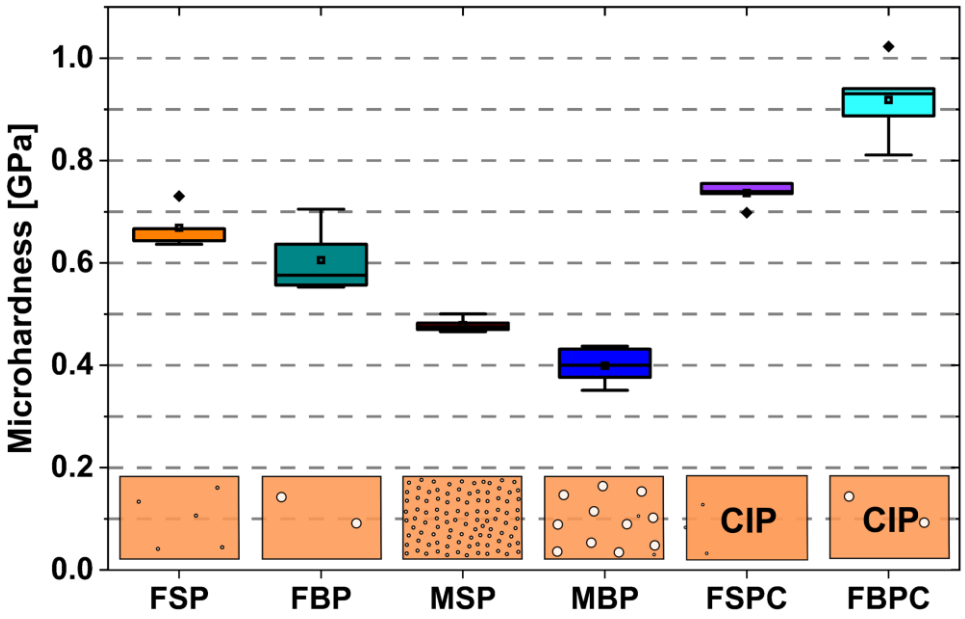

Figure 4.13: Microhardness measurements of the different samples with varying number and size of pores as indicated by the symbols [122]. The applied load is 250 mN. CIP indicates that the specimen was additionally cold isostatically pressed. The box represents the interquartile range from the first to the third quartile, with the median as a line; whiskers show values within 1.5 times the interquartile range, outliers appear as diamonds and the mean as a square.

4.2.2 Tribological Behavior

The measured coefficients of friction over 1000 cycles, presented in Figure 4.14, showed a significant difference between vibropolished specimens with low and high porosity. The coefficients of friction of specimens with low porosity increased significantly by 0.3 to 0.5 within the first 100-200 cycles, whereas they remained nearly constant in specimens with high porosity. While the coefficients of friction of high-porosity specimens reached a value of approximately 0.3 after 1000 cycles, those of low-porosity samples were at least twice as high.

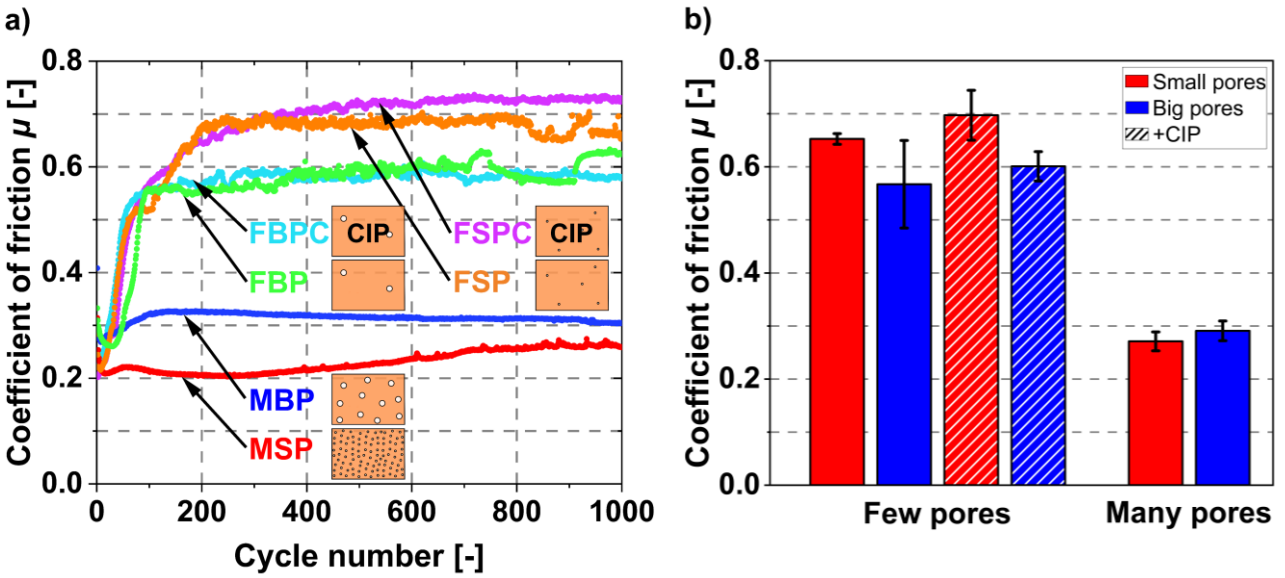

Figure 4.14: Coefficients of friction of the vibropolished specimen types a) over 1000 cycles and b) the mean values and standard deviations in cycle 1000 [122]. The symbols represent the varying number and size of pores and whether the sample was cold isostatically pressed (CIP).

SEM analysis using secondary electron imaging, shown in Figure 4.15a) to e), revealed that delamination occurred in the wear track of both the CIP specimens shown in Figure 4.15a) and b) and the FBP specimens illustrated in Figure 4.15d). Neither the FSP specimens, nor those with high porosity, indicated surface delamination due to the tribological tests. The zoomed-in backscattered electron (BSE) images of the MSP and MBP samples in Figure 4.15f) and g) revealed that sintered powder particles were still visible on the surface of the wear tracks even after 1000 cycles, indicating they were not deformed in sliding direction by the counterbody during the tribological experiments. Furthermore, there were significantly more grooves in the sliding direction on the low-porosity samples compared to the high-porosity ones, as exemplarily highlighted in Figure 4.15c).

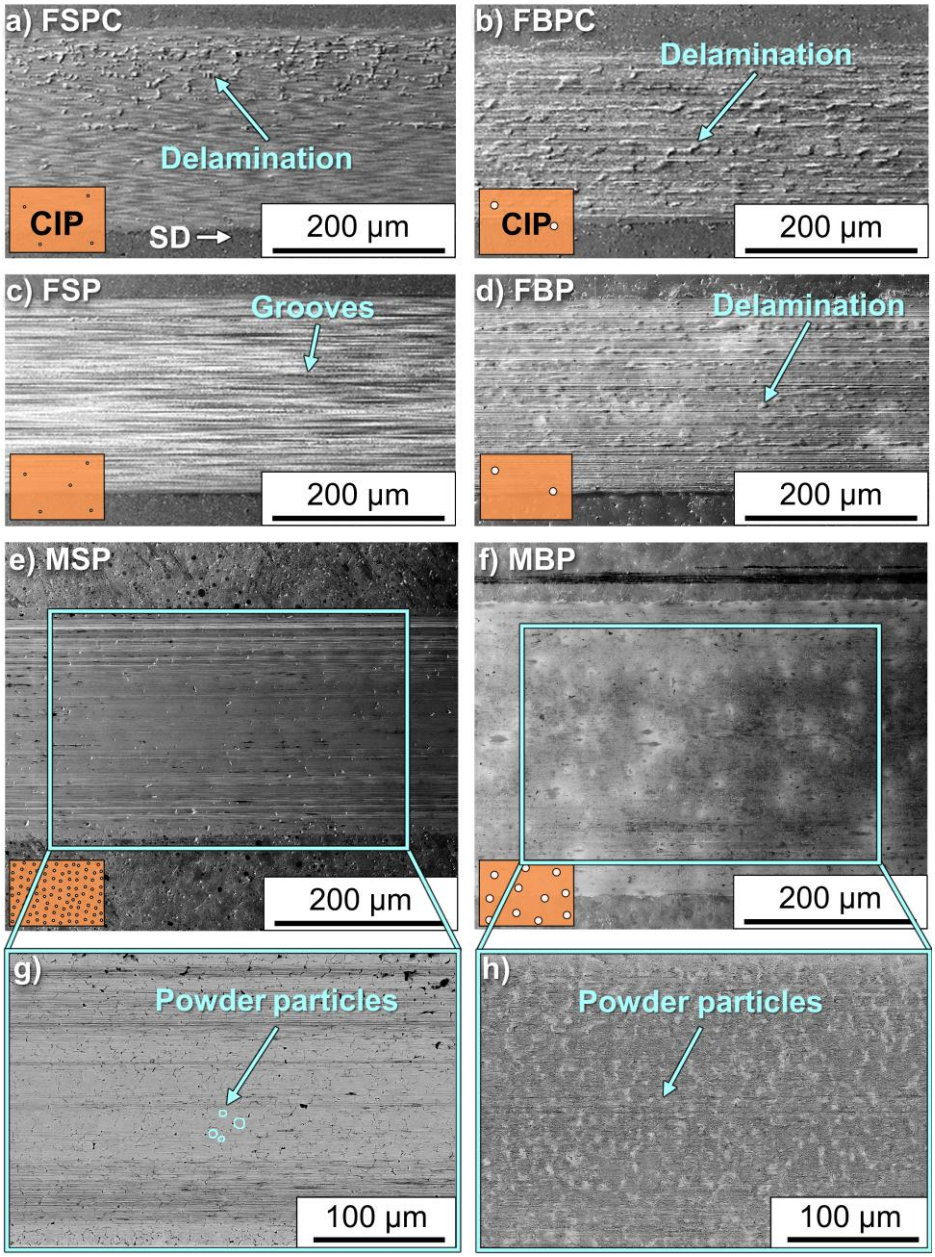

Figure 4.15: SEM images of the surfaces in the center of the wear track for various specimens [122]. While secondary electron images are shown for a) FSPC, b) FBPC, c) FSP, d) FBP, e) MSP, and f) MBP, BSE images of the sections of specimens with high porosity are presented in g) and h). The symbols indicate the number and size of pores and whether the sample was cold isostatically pressed (CIP). The sliding direction (SD) is valid for all images.

Figure 4.16 presents cross-section images in the sliding direction at the center of the wear tracks for the varying sample types. In all cross-sections, a dark gray zone (F1) could be detected directly beneath the surface. While this zone was clearly visible in the cross-sections of specimens with low porosity as illustrated in Figure 4.16a) to d), it was barely present in specimens with a high number of sintering pores as shown in Figure 4.16e) and f). Among the specimens with few sintering pores,

those with larger pores displayed a more pronounced dark gray area in Figure 4.16b) and d) compared to those with smaller pores in Figure 4.16a) and c). Additionally, black, elongated features (F2) appeared in the dark gray zone in the FSPC, FBPC and FBP. In all cross-sections of the samples having a small number of sintering pores, black, circular features were observed in the dark gray layer, which is exemplarily shown in Figure 4.16c) along the interface between the dark and light gray areas. At the interface between the sintering pores and the particles, an oxide-rich layer was detected, as shown in Figure A.6.

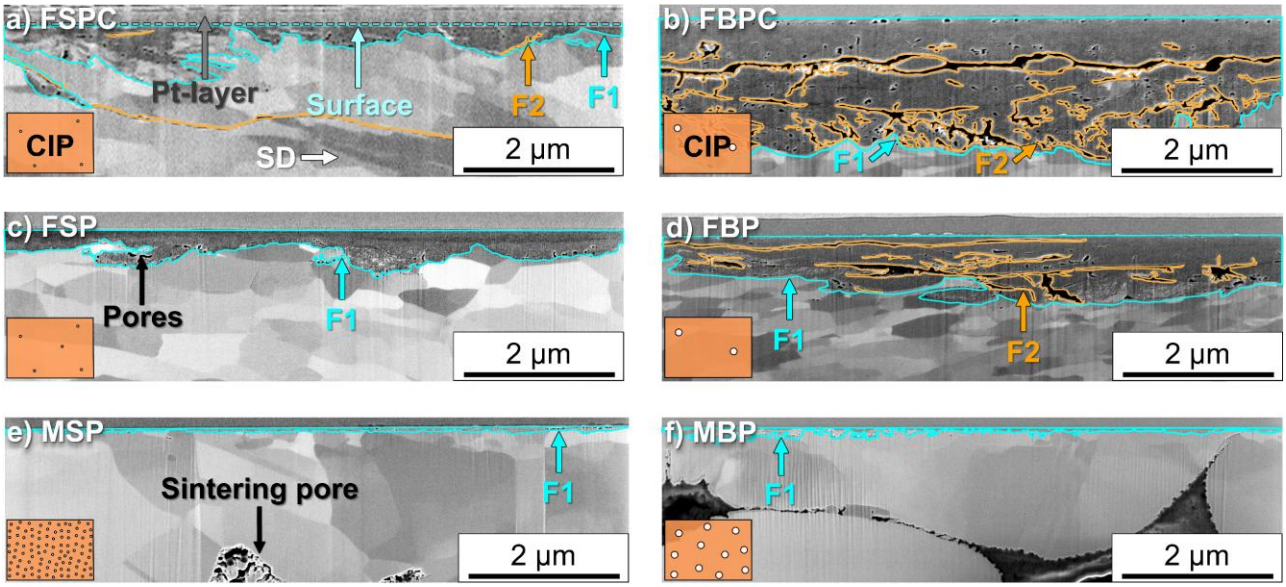

Figure 4.16: SE cross-section images in sliding direction at the center of the wear track for a) FSPC, b) FBPC, c) FSP, d) FBP, e) MSP, and f) MBP [122]. The symbols indicate variations in pore quantity and size and if the specimen was cold isostatically pressed (CIP). The white arrow indicates the sliding direction (SD) in all images. In a), the specimen surface is exemplarily marked beneath the protective platinum layer.

In the light microscope images, a discolored surface could be observed along the wear track, as shown in Figure 4.17. While specimens with many sintering pores exhibited a bluish-reddish surface in Figure 4.17e) and f), specimens with few sintering pores showed a darker surface, as visible in Figure 4.17a) to d). In contrast to specimens with few sintering pores, on the surfaces of specimens with many sintering pores, as shown in Figure 4.17e) and f), the colored area did not appear to be continuous, with individual copper-colored portions visible.

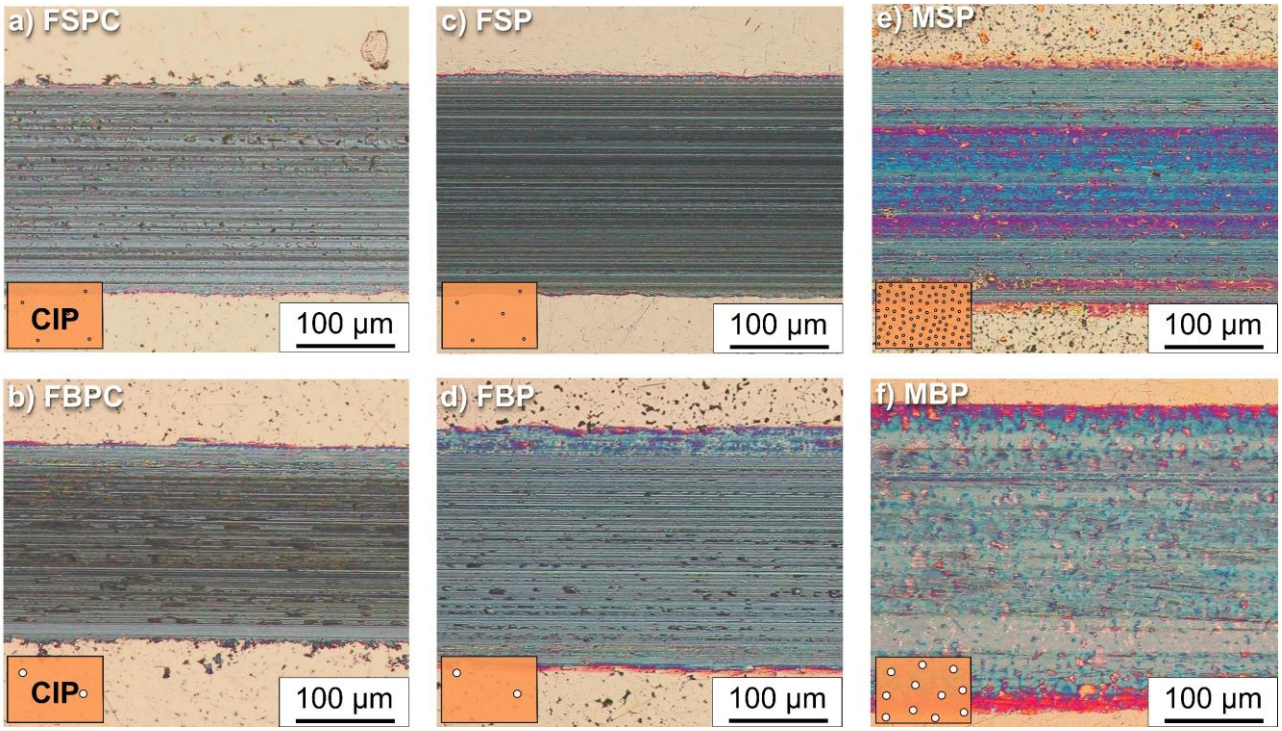

Figure 4.17: Light microscopy images of the surfaces in the center of the wear tracks of a) FSPC, b) FBPC, c) FSP, d) FBP, e) MSP, and f) MBP after 1000 sliding cycles [122]. The symbols represent differences in pore quantity and size and if the specimen was cold isostatically pressed (CIP).

In addition to the tribologically induced dark gray zone, cross-sections in Figure 4.18 reveal a region beneath the surface of the various specimens where the grain sizes were smaller than those in the bulk material. This deformation layer (DL) extended deeper into the sample as the dark gray layer (F1) shown in Figure 4.16. As highlighted in Figure 4.19, for FSPC this area with smaller grain sizes was approximately 5.7 ± 2.1 µm deep, about 6.4 ± 1.1 µm for FBPC, around 7.2 ± 2.4 µm for FSP, approximately 2.9 ± 1.3 µm for FBP, and about 0.4 ± 0.2 µm thick for MSP and 0.6 ± 0.2 µm for MBP.

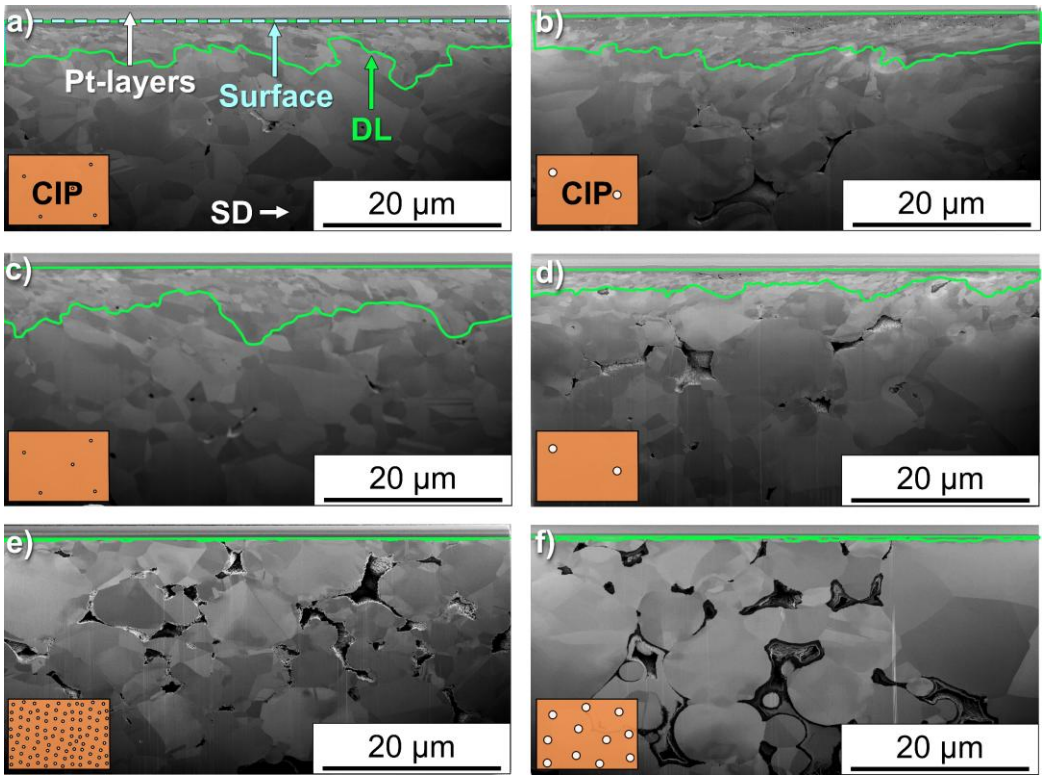

Figure 4.18: SE cross-section images in sliding direction at the centers of the wear tracks for a) FSPC, b) FBPC, c) FSP, d) FBP, e) MSP, and f) MBP [122]. Variations in pore size and quantity, along with whether the specimen was cold isostatically pressed (CIP), are indicated by the symbols. The sliding direction (SD) and the specimen surface marked below the protective platinum layers apply to all images.

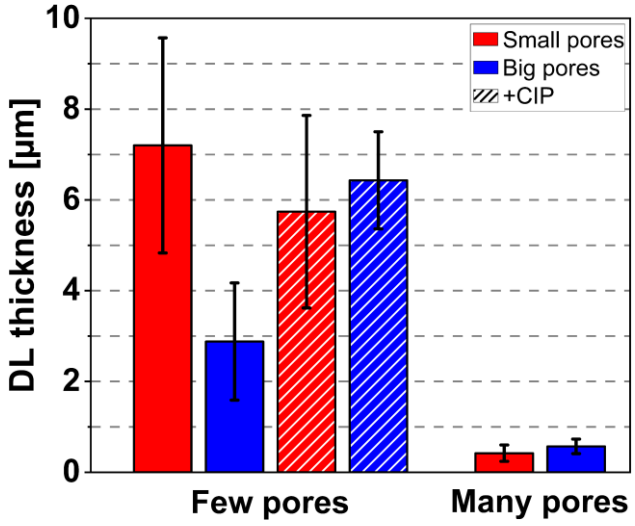

Figure 4.19: Overview of the mean deformation layer (DL) thicknesses and their standard deviations for the different specimen types at the center of the wear tracks. Hatching indicates specimens that were additionally cold-isostatically pressed (CIP).

A difference in wear track profiles measured with a white light interferometer, and consequently in topographical deformation, was also noticeable between the samples with many and few sintering pores, as shown in Figure 4.20. While low-porosity specimens exhibited pile-ups at the edges of the wear tracks, those with many sintering pores were 0.9-2.0 µm deeper and 100-200 µm wider. Additionally, it could be observed that the wear track of MBP was around 0.5 µm deeper than that of MSP.

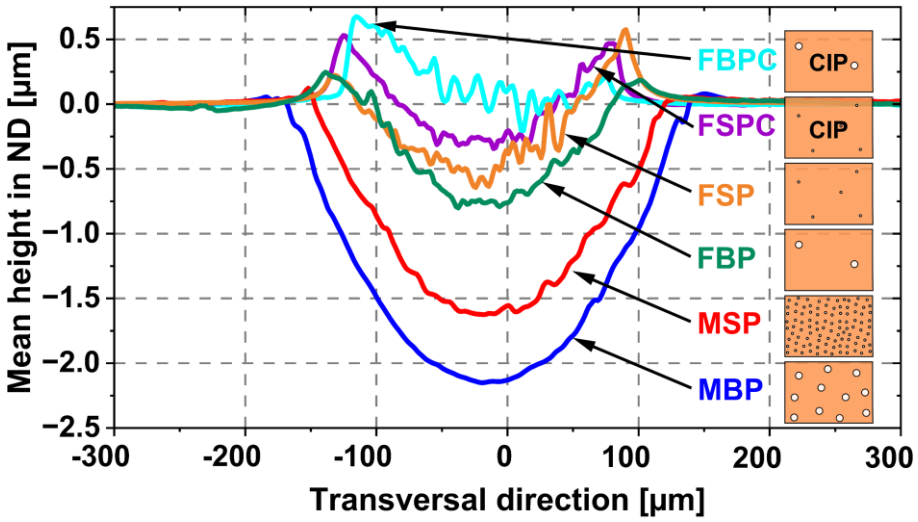

Figure 4.20: Average height profiles of the wear track centers for the various specimen types [122]. The symbols represent the pore quantity and size of the specimens and whether they were cold isostatically pressed (CIP).

Figure 4.21 shows light microscope images of the sapphire spheres which were used in tribological experiments on FSP and MSP samples. No significant difference in material transfer from the bulk to the sphere over the course of the tests could be observed. The MSP experiment showed a larger contact area of the sphere, resulting in a wider wear track, consistent with the wear track profiles in Figure 4.20. Furthermore, the sphere on FSP exhibited more pronounced grooves.

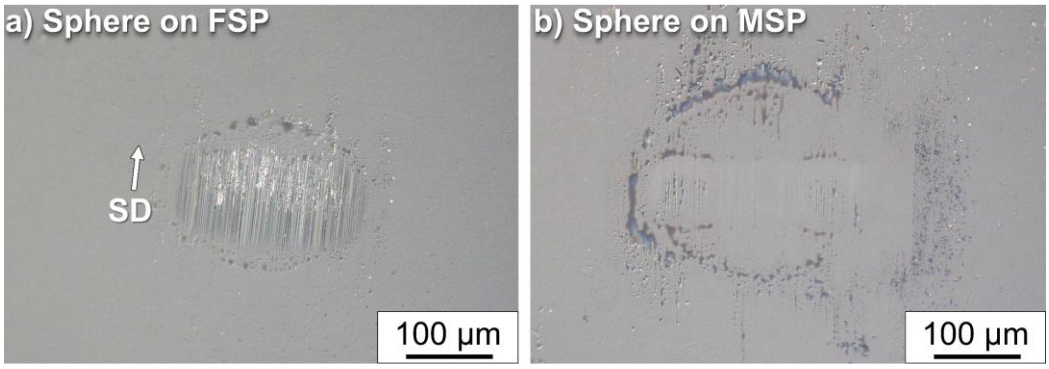

Figure 4.21: Light microscope images of the sapphire spheres after tribological experiments with a) few small pores (FSP) and b) many small pores (MSP) [122]. The sliding direction (SD) is indicated by the arrow.

4.2.3 Long Term Tribological Performance

By increasing the number of cycles from 1000 to 5000 for the vibropolished specimens, Figure 4.22a) shows that the differences in the coefficients of friction due to varying porosities remained. The coefficients of friction of the samples with many pores stabilized at a value of 0.23 after 5000 cycles, while the coefficient of friction of the specimen with few small pores was nearly three times higher, reaching 0.67. The increase in the coefficient of friction of MSP after approximately 2500 cycles could be attributed to an increase in relative humidity, as shown in Figure A.7 in the Appendix. Figure 4.22b) demonstrates that, compared to FSP, specimens with many pores exhibited a 1.0 to 1.5 µm deeper wear track, and MBP showed an approximately 100 µm wider wear track. Furthermore, specimens with many sintering pores exhibited no pile-ups at the edges of the wear track after 5000 cycles, in contrast to FSP.

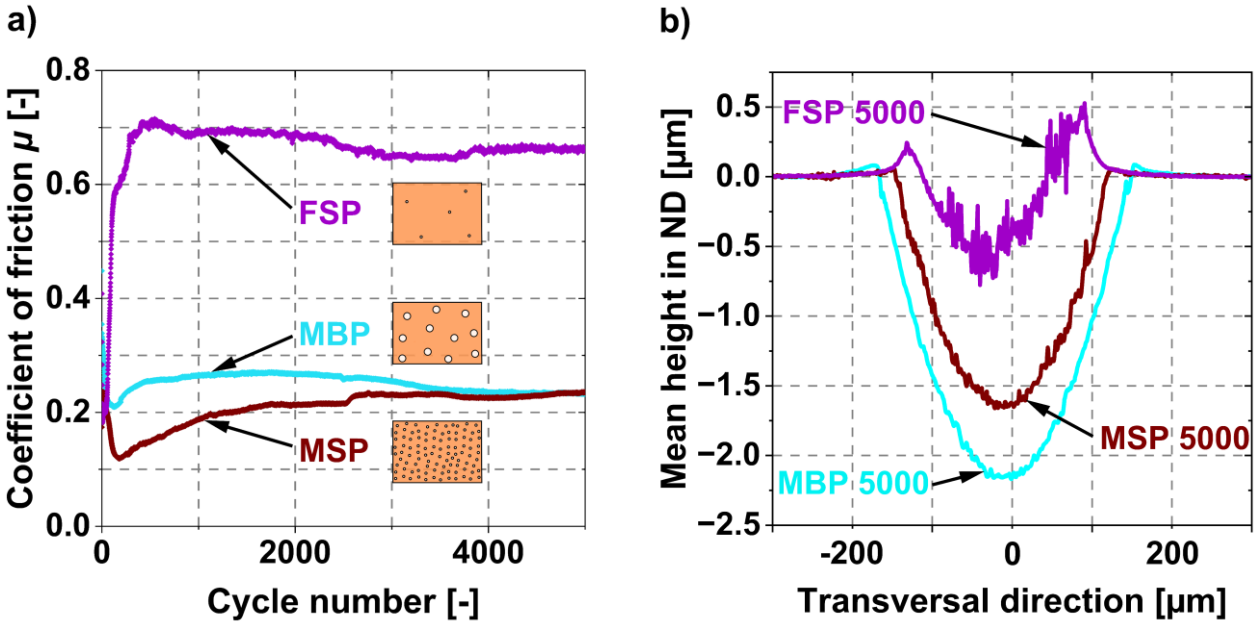

Figure 4.22: a) Development of the coefficients of friction over 5000 cycles for vibropolished FSP, MSP, and MBP, and b) comparison of their wear track profiles based on white light interferometric images after 5000 cycles (adapted from [135]). The symbols represent the number and size of pores of the different specimen types.

Below the surfaces of the different specimen types after 5000 cycles, a zone with finer grains (DL) was observed in the FIB cross-section images shown in Figure 4.23a), c), and e). This deformation layer was approximately 15.8 µm deep in FSP, while in specimens with many sintering pores, it was much shallower, with maximum depths of 0.8 µm in MSP and 1.2 µm in MBP. Furthermore, in all three microstructures a dark gray layer (F1) appeared, as visible in Figure 4.23b), d), and f). This

layer was also significantly more pronounced in FSP, as it extended up to 1.9 µm beneath the surface, while for MSP it reached 0.3 µm and for MBP 0.5 µm. In contrast to the other microstructures, FSP also exhibited black elongated features (F2) beneath the surface, as shown in Figure 4.23b).

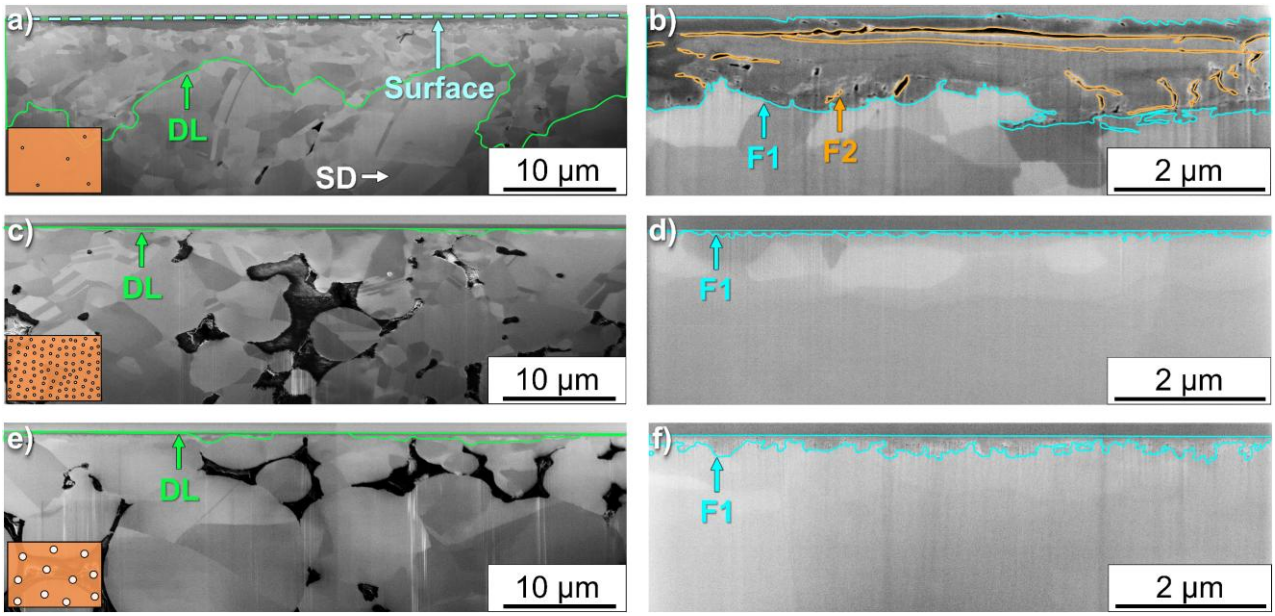

Figure 4.23: SE cross-section images in sliding direction at the center of the wear track after 5000 cycles of vibro-polished FSP in a) and b), MSP in c) and d), MBP in e) and f) (adapted from [135]). The variations in pore size and quantity are indicated by the symbols. The sliding direction (SD) and the sample surface marked in a) applies to all images.

4.2.4 Microstructural Impact of Vibropolishing and Electropolishing

During the investigation of surface treatment effects on the FAST samples, the densities of the ground specimens were initially measured. The MSP specimen that was subsequently electropolished had a total density of 85.0 %, while the MSP specimen that was vibropolished afterward showed a total density of 84.8 %. After electropolishing or vibropolishing, the surfaces of the specimens were analyzed using both the profilometer and SEM, as shown in Figure 4.24. It was found that the vibropolished specimen had a surface roughness *Sa* of 0.11 µm, while the electropolished sample had a value of 1.63 µm, more than 16 times higher. In both the profilometer and SEM images, it is evident that electropolishing significantly enlarged the sintering pores and led to rounding of the sintering pore edges.

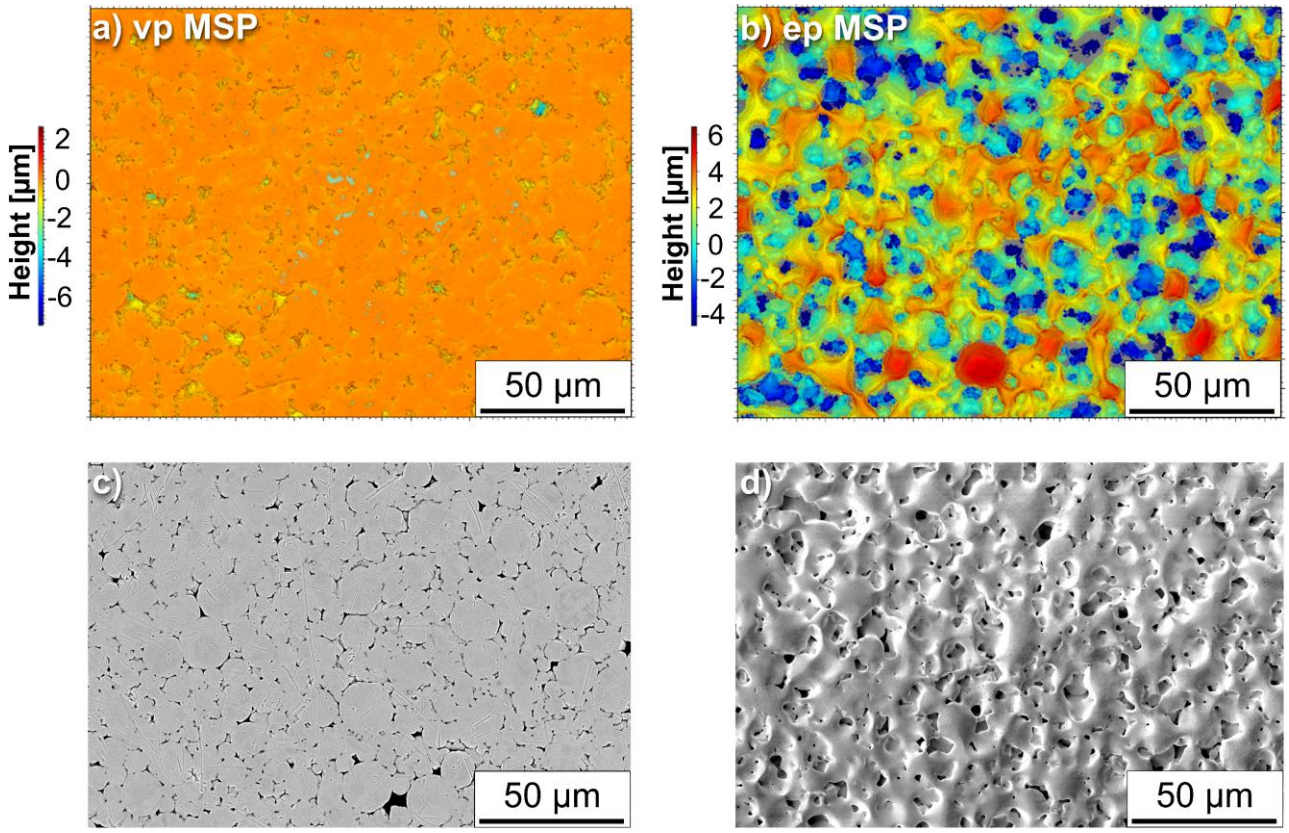

Figure 4.24: Optical surface profilometry images of the a) vibropolished (vp) and b) electropolished (ep) surfaces of specimens with many small pores (MSP), and SEM images of the c) vibropolished and d) electropolished MSP surfaces (adapted from [135]).

Clear differences between the microhardness values of MSP after different surface treatments are shown in Figure 4.25. The vibropolished surface showed an average hardness of 0.48 GPa with a standard deviation of 0.01 GPa, whereas the electropolished surface exhibited an average hardness of 0.30 GPa with a standard deviation of 0.09 GPa.

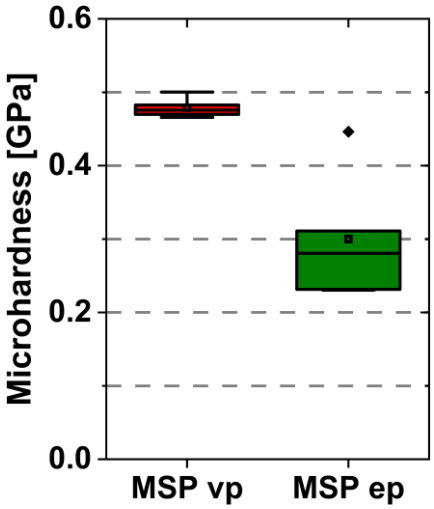

Figure 4.25: Microhardness measurements of vibropolished (vp) specimens and an electropolished (ep) sample with many small pores (MSP). The box represents the interquartile range from the first to the third quartile, with the median as a line; whiskers show values within 1.5 times the interquartile range, outliers appear as diamonds and the mean as a square.

A closer examination of the electropolished surface in the SEM, shown in Figure 4.26, revealed circular patterns (CP) on the surface, which were visible at varying densities in different areas of the specimen. In the center of the CP small craters could be detected, as visible in Figure 4.26c). It could also be observed that electropolishing resulted in a more pronounced material removal at the grain boundaries.

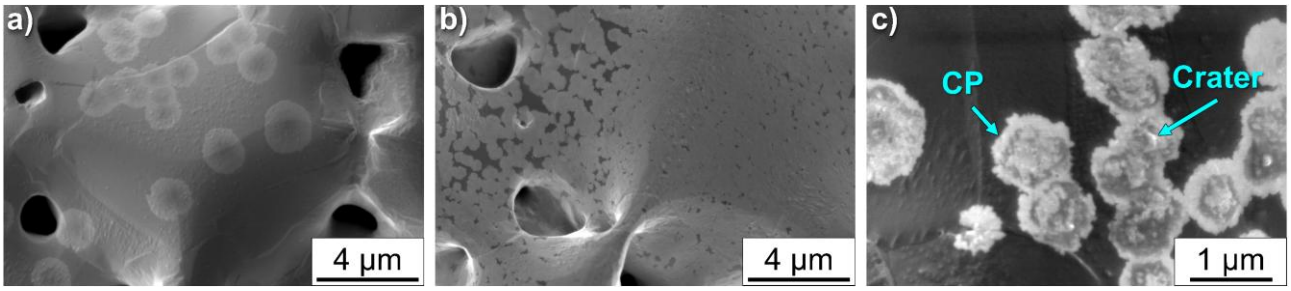

Figure 4.26: SE images of the electropolished surface of a specimen with many small pores showing circular patterns (CP) at varying densities, with a), b) and c) taken from different spots in the center of the specimen (adapted from [135]).

4.2.5 Tribological Effect of Vibropolishing and Electropolishing

In order to consider a potential influence of the native oxide layer, tribological experiments were performed on the surface both immediately after electropolishing and after 24 h in air. The coefficients of friction of the varying specimen types over 1000 cycles in Figure 4.27 displayed significant differences between electropolished and vibropolished MSP specimens. While the

coefficient of friction of the vibropolished samples reached a value of 0.2 after just a few cycles and showed only a slight increase over the cycles, the coefficient of friction of the electropolished sample reached nearly three times that value within the first 50 cycles. While the value for the sample tested directly after electropolishing subsequently dropped by 0.1 and then rose, reaching the value of the first peak after approximately 600 cycles, the coefficient of friction of the surface exposed to air for 24 h after electropolishing showed a steady, slight increase. After 1000 cycles, the coefficients of friction of the electropolished MSP sample were comparable to the one of vibropolished FSP, ranging between 0.6 and 0.65, as shown in Figure 4.14. Thus, the coefficients of friction of the electropolished MSP were about 2.5 times higher than that of vibropolished MSP, which reached a value of approximately 0.25 after 1000 cycles.

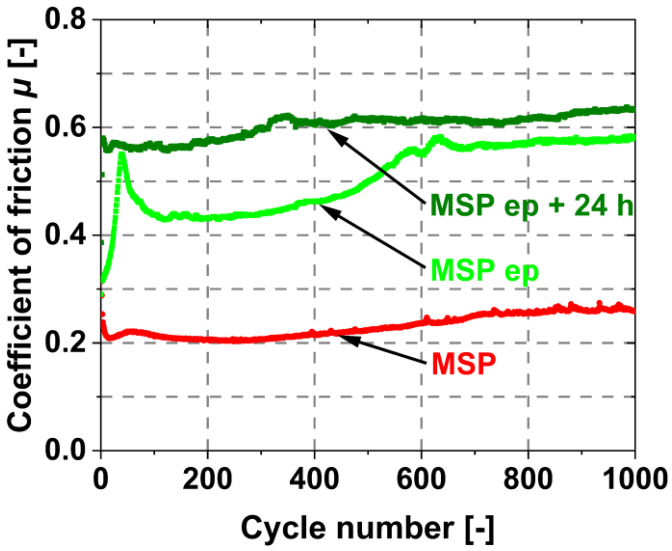

Figure 4.27: Coefficients of friction of the specimens with many small pores after vibropolishing or electropolishing (ep) over 1000 cycles (adapted from [135]). The electropolished sample was tested immediately and after an additional 24 h exposure to air.

Based on the SEM investigations of the wear tracks shown in Figure 4.28, particularly in the SE images in Figure 4.28a) and b), it could be observed that delamination occurred on the surface during both tribological tests. The craters within the wear tracks resembled the sintering pores adjacent to the tracks, which were enlarged by the electropolishing process. BSE images in Figure 4.28c) and d) show that these sintering pores were partially worn away and filled during tribological loading, especially at the center of the wear tracks.

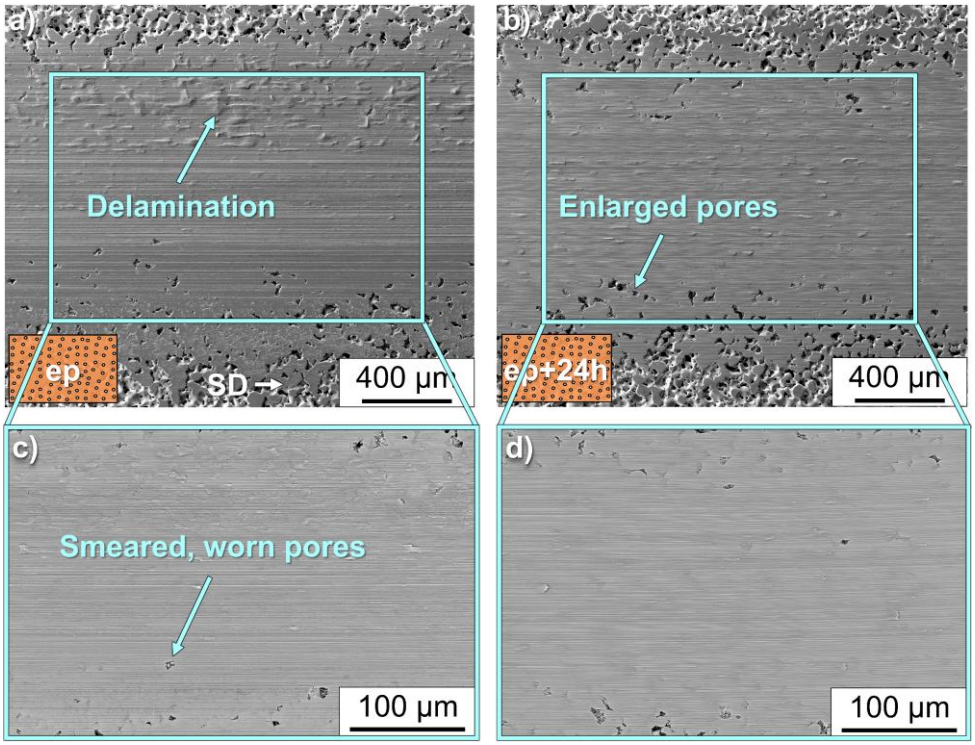

Figure 4.28: SEM images of the wear tracks of the electropolished surface of a specimen with many small pores in a) and c) as well as the electropolished (ep) surface exposed to air for 24 h before tribological testing in b) and d) (adapted from [135]). While SE images are shown in a) and b), enlarged BSE images are visible in c) and d). The sliding direction (SD) shown in a) also applies for b).

Similarly, no significant differences in the subsurface microstructure could be observed in Figure 4.29 between the specimen tested immediately after electropolishing and after an additional 24 h exposure to air before the tribological test. In both microstructures, the subsurface deformation layer (DL) in Figure 4.29a) and c) was similarly pronounced, reaching depths of up to 3.8 µm after electropolishing and up to 7.4 µm with an additional 24 h after electropolishing. Also, the dark gray zone (F1) in Figure 4.29b) and d) was similarly developed, with maximum depths of 1.6 µm after electropolishing and 0.8 µm tribologically tested 24 h after electropolishing. In this zone, black elongated features (F2) were visible in both microstructures. Additionally, the sintering pores seemed to act as boundaries for the subsurface deformation, as the grain refinement did not extend deeper into the material once a sintering pore appeared.

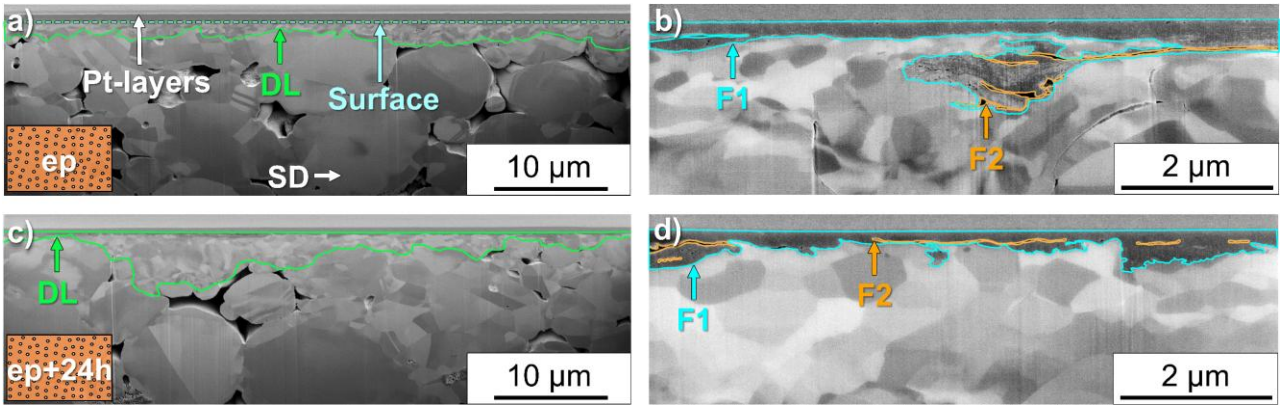

Figure 4.29: SE cross-section images in sliding direction at the center of the wear tracks of the specimen with many small pores tested directly after electropolishing (ep) in a) and b), and after an additional 24 h exposure to air in c) and d) (adapted from [135]). The sliding direction (SD) shown in a) applies to all images. In a) the specimen surface is exemplarily marked beneath the protective platinum layers.

Light microscopy images in Figure 4.30 showed no significant difference between the wear track width of the MSP surface that was tribologically tested immediately after electropolishing in Figure 4.30a) and the wear track of the surface exposed to air for 24 h before the tribological test in Figure 4.30b). Additionally, both exhibited a similar groove pattern in sliding direction, as well as the same grayish discoloration in the wear track. In both, craters could be detected, which were more frequent at the edges of the tracks.

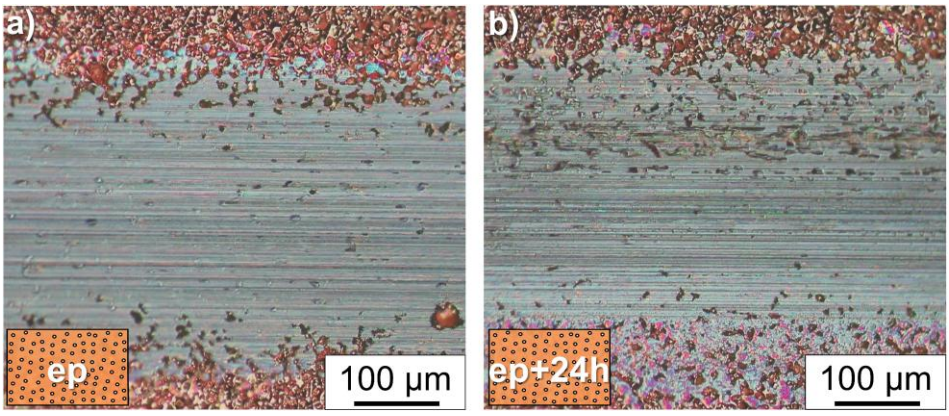

Figure 4.30: Light microscopy images of the wear tracks of the specimen with many small pores tested a) directly after electropolishing (ep) and b) after additionally being exposed to air for 24 h (adapted from [135]).

Based on the mean wear track profiles measured from white light interferometric images in Figure 4.31, it could be observed that the electropolished samples exhibited a much rougher surface compared to the vibropolished ones. Additionally, no significant pile-ups could be observed at the sides of the wear tracks of all the specimens with many sintering pores. In general, the wear tracks

of MSP showed a tendency to be, on average, 0.9 µm less deep and 100 µm narrower than those of MBP. The wear track depths and widths of the electropolished MSP lied between the depths of vibropolished MSP and MBP.

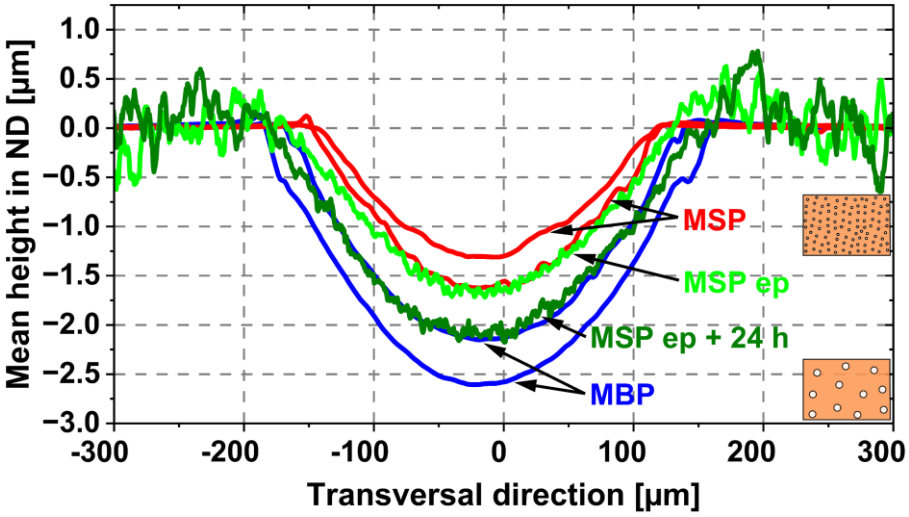

Figure 4.31: Wear track profiles based on white light interferometric images of the vibropolished or electropolished (ep) sample with many small pores (MSP) and vibropolished sample with many big pores (MBP) (adapted from [135]). The electropolished sample was tested directly after electropolishing and after being exposed to air for 24 h.

5 Discussion

The research hypothesis underlying this work that gradient nano-grained (GNG) microstructures have a greater impact on the tribological behavior of copper under mild loading conditions than porous copper samples and can achieve more effective friction reduction, is discussed in the following based on the results presented in Chapter 4. The study is guided by two main research questions:

1. Can a GNG surface layer reduce the coefficient of friction under mild tribological loading conditions? How does the thickness of the GNG layer and the size of the surface grains influence the tribological performance?

2. How do pore size and overall porosity affect the tribological behavior? To what extent does surface porosity influence this behavior?

5.1 Tribological Behavior of GNG Samples

5.1.1 Comparative Analysis of Various GNG Microstructures

Before it can be determined which conditions are necessary to achieve a reduction of the coefficient of friction under mild tribological conditions, the behavior of the different GNG microstructures under tribological loading has to be analyzed. The surface mechanical grinding treatment (SMGT) and surface post-treatments produced GNG microstructures in all samples, differing in both gradient depth and the grain sizes directly at the surface, as shown in Figure 4.1 and summarized in Table 3.1. After the tribological tests, grooves in the sliding direction were observed in all wear tracks, as visible in Figure 4.8. Single trace experiments of sapphire on single-crystal copper showed that grooves formed already during indentation, with widths of approximately 0.2-0.4 µm, as visible in Figure A.8. Since the sapphire sphere exhibited asperities in a similar size range on its surface, as shown in Figure A.9a) and b), the grooves observed in the copper wear track could be caused by these asperities. Consequently, the grooves visible in Figure 4.8 could be attributed to abrasive wear, caused by asperities of the harder counterbody [63]. Besides that, clear differences in both tribological performance and the resulting microstructure were observed between GNG-0(Chen), GNG-30(Chen), and

GNG1-60 on the one hand, and GNG2-10 and GNG2-160 on the other, as summarized in Table 5.1. The numbers following the hyphen represent the amount of surface removal.

Table 5.1: Overview of the coefficients of friction and the main differences in the microstructural evolution of the gradient nano-grained (GNG) samples. The information about GNG-0(Chen) and GNG-30(Chen) was taken from Chen et al. [12]. The thick arrows represent the severe tribological loading conditions (normal force: 30 N, sliding speed: 10 mm s^{-1}, stroke: 1 mm) and the thin arrow indicate the mild tribological loading conditions (normal force: 2 N, sliding speed: 0.5 mm s^{-1}, stroke: 6 mm). The thickness of the GNG layer is indicated in red.

Sample & Tribological loading condition	Coefficient of friction (number of cycles)	Microstructural evolution
 **GNG-0(Chen)**[12]	**0.37** (6000)	Grain coarsening Dynamic recrystallization (DRX)
 **GNG-30(Chen)**[12]	**0.43** → **0.53** (1000, 6000)	Grain coarsening Tribo-oxidation DRX (GNG-30(Chen))
 **GNG1-60**	**0.30** → **0.50** (1000, 6000)	
 **GNG2-160**	**0.61** (1000)	Grain coarsening Tribo-oxidation Cracking Delamination
 **GNG2-10**	**0.53** (1000)	

Detailed analysis of the microstructures before and after tribological testing showed that the evolution observed in GNG1-60, as illustrated in Figure 5.1, was comparable to the microstructural changes of GNG-30(Chen) reported by Chen et al. [12]. This was likely due to the partial or full removal of the subsurface nano-grained (NG) layer during surface post-treatments, as evidenced by the reduced microhardness of GNG1-60 compared to GNG-0(Chen) shown in Figure 4.4. Accordingly, tribological testing resulted in subsurface grain sizes of about 350 nm in GNG1-60, which exceeded the 200 nm grain size found in the grain coarsening layer of the GNG-0(Chen) microstructure. This may be attributed to the removal of the NG layer at the surface during surface post-treatment, which, in the case of GNG-0(Chen), appeared to prevent the formation of a grain coarsening layer during tribological testing. This stability of the NG layer is likely related to the presence of energetically more stable deformation-twin boundaries and to the high yield strength of nanograins, the latter

reducing plastic deformation at the surface. Furthermore, vertically elongated grains within the top 30 µm beneath the surface, as shown in Figure 4.10a), indicate the characteristic vertical plastic flow occurring in the 25 µm grain coarsening layer, which is associated with the low-to-high friction transition in GNG-0(Chen) samples [13]. According to Chen and Han [13], the saturation of grain coarsening limits the material's ability to accommodate plastic strain uniformly, thereby promoting the onset of local shear instability. Consequently, subsurface deformation progresses into the topmost NG layer, leading to local variations in thickness. The resulting surface roughening facilitates crack initiation and delamination [13, 111]. The regions with fine features, along with small, round black areas representing pores, highlighted in blue (F0), extended to depths of up to 13.3 µm, as visible in Figure 4.10a) and b) [90]. These regions correspond to the mechanically mixed layer (MML) [12]. This layer, consisting of NG and tribo-oxides, typically forms during the low-to-high friction transition of GNG specimens. Microcracks, appearing as black, elongated features similar to those observed in GNG-30(Chen), were also present within the MML of GNG1-60 and at the interface between the MML and the dynamic recrystallization (DRX) layer. The earlier low-to-high friction transition observed in GNG1-60 and GNG-30(Chen) compared to GNG-0(Chen) can be attributed to the larger grain size beneath the surface. These coarser grains exhibit a lower yield strength and are therefore able to undergo greater plastic deformation. As a consequence, plastic deformation increases near the surface, likely leading to a breakdown of homogeneous plastic strain accommodation after fewer cycles. This is evident from the locally vertically aligned grain morphologies in the cross-section, as visible in Figure 4.10a).

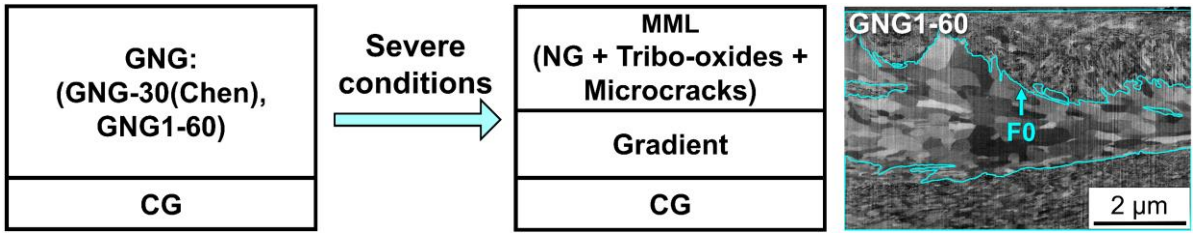

Figure 5.1: Representation of the microstructural evolution of GNG-30(Chen) and GNG1-60 under severe tribological loading conditions (normal load: 30 N, sliding speed: 10 mm s^{-1}, stroke: 1 mm, sliding cycles: 6000 and 7500). Beneath the gradient nano-grained (GNG) layer lies the coarse-grained (CG) bulk, while nanograins (NG) are found in the mechanically mixed layer (MML).

In contrast, GNG2-10 and GNG2-160 exhibited a significantly different microstructural evolution, as shown in Figure 5.2, due to the tribological tests being conducted under mild loading conditions, meaning with a normal load of 2 N, a stroke length of 6 mm, and a speed of 0.5 mm s^{-1}. A pronounced difference in the extent of tribologically affected zones (DL) was observed, with GNG1-60 showing depths of at least 31.7 µm, compared to 11.0 µm in GNG2-160 and around 4.4 µm in GNG2-10, although their surface grain sizes were comparable, as demonstrated in Figure 4.10. The differing depths are a result of varying contact stresses arising from different normal loads. Under a normal load of 2 N, the copper-sapphire contact used for GNG2-10 and GNG2-160 produces a maximum Hertzian pressure of 581 MPa, whereas the copper-WC-Co contact with a normal load of 30 N applied for GNG1-60, GNG-30(Chen), and GNG-0(Chen) results in a Hertzian pressure of up to 1511 MPa [136]. The significantly higher pressure promotes more severe subsurface deformation, affecting the microstructure at greater depths. An additional distinction can be seen in the tribo-oxide layer, which is characterized by island-like features, the presence of pores, and a uniformly dark appearance [90, 91]. The tribo-oxides differed significantly in their morphology and appearance as shown in the highlighted blue zones F0 and F1 in the cross-sectional SEM images in Figure 4.10b), d) and f) and the light microscopy images in Figure 4.8. Unlike GNG1-60, where the MML features a finely intermixed structure likely composed of residual nanograins and tribo-oxide (F0), the F1 region in GNG2-160 and GNG2-10 showed a clear separation between the tribo-oxide and the copper grains, as observed in Figure 4.10d) and f). In addition, the tribo-oxides of GNG1-60 showed a different color compared to those of GNG2-160 and GNG2-10, as shown in the light microscopic images in Figure 4.8. While the wear track of GNG1-60 displayed a reddish coloration, indicating the presence of Cu_2O, the surfaces of the wear tracks of GNG2-160 and GNG2-10 appeared black [97, 98, 100]. Cu_2O is known to form during tribo-oxidation at room temperature [70]. Since the color of the oxide varies with its thickness, the different colors of the tribo-oxides in Figure 4.8 likely reflect corresponding differences in thickness [137]. In combination with the still visible copper grain structure in the MML of GNG1-60, shown in the cross-sectional images in Figure 4.10, it can be assumed that tribo-oxidation was either less advanced due to the shorter test duration of 25 min compared to the 400 min experiments in GNG2-160 and GNG2-10, or that it was initiated at later stages of the tribological experiment in GNG1-60. The cross-sectional images

clearly show that the tribo-oxide in GNG1-60 penetrated up to 13.3 µm into the material, whereas in GNG2-160 and GNG2-10, it extended only to depths of 2.5 µm and 1.8 µm, respectively. However, this difference may primarily result from the varying normal loads applied during testing and is therefore not necessarily indicative of the actual duration of the tribo-oxidation, as higher normal loads result in an increased Hertzian stress, which is also evident in the greater depth of subsurface deformation. The observed pores in the tribo-layer are most likely the result of the Kirkendall effect. During the tribological loading, Kirkendall pores form at the interface between oxide and copper due to the faster diffusion rate of copper ions compared to oxygen ions [90, 95]. With prolonged oxidation, pores also form along the diffusion paths [90]. As oxidation progresses, the tribo-oxide layer grows deeper into the copper specimen, causing the interface between oxide and copper to shift inward. This may result in pores and cracks (F2), as marked in Figure 4.10, appearing at different depths after numerous cycles of tribological loading. With increasing oxidation, these Kirkendall pores most likely gave rise to both subsurface cracks (F2), marked in orange in Figure 4.10d) for GNG2-160, as well as in Figure 4.10e) and f) for GNG2-10, and delamination at the surface, as evidenced by Figure 4.9. The formation of Cu_2O leads to a volume expansion of around 1.7 times that of copper [99]. Consequently, both the increased volume of the copper oxide layer and the occurrence of surface delamination contributed to the wear track appearing elevated relative to the surrounding copper surface in the profilometric images of Figure 4.7. These energy-dissipating processes are linked to the high-friction regime. Together with the observation that GNG2-160 and GNG2-10 showed high coefficients of friction after 50 and 240 sliding cycles, respectively, this indicates that tribo-oxidation proceeded over a significant portion of the tribological testing duration. In summary, these findings suggest that tribo-oxidation in GNG2-160 and GNG2-10 potentially progressed over a longer test duration and was thus more pronounced compared to GNG1-60.

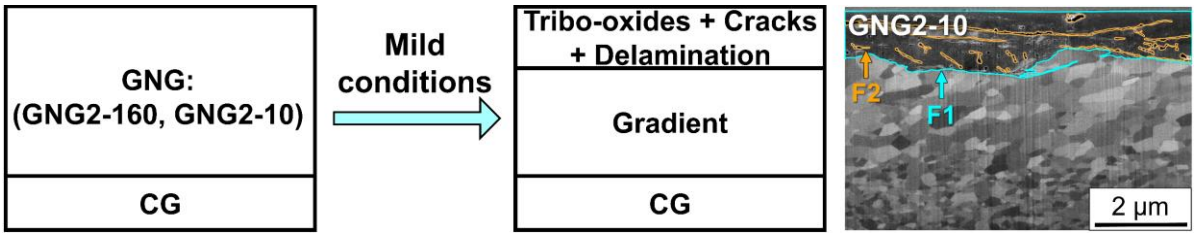

Figure 5.2: Microstructural evolution of GNG2-160 and GNG2-10 under mild loading conditions (normal load: 2 N, sliding speed: 0.5 mm s^{-1}, stroke: 6 mm, sliding cycles: 1000). The coarse-grained bulk (CG) is located beneath the gradient nano-grained layer (GNG).

Despite identical experimental conditions, GNG2-160 and GNG2-10 displayed differences in their tribological behavior. After the tribological experiments, GNG2-10 exhibited finer grains beneath the surface, and its coefficient of friction increased to a value above 0.5 within the first 240 cycles. In contrast, GNG2-160 showed a faster increase, reaching a coefficient of friction of 0.61 within the first 50 cycles, as evident in Figure 4.6. The delayed increase in the coefficient of friction observed for GNG2-10 may be attributed to its higher surface microhardness, as shown in Figure 4.4. According to Bowden and Tabor [60], the real contact area

$$A_R = F_N / p \qquad \text{Equation 7}$$

depends on the normal force F_N and the indentation hardness p, assuming that all microcontacts undergo plastic deformation and that the contact pressure equals the indentation hardness [138]. Therefore, the initially finer grain structure and resulting higher microhardness of GNG2-10 suggest a reduced real contact area. Bowden and Tabor [60] identified adhesion and deformation as the two main contributors to the frictional force. As stated in Amonton's first law, shown in Equation 3 in Chapter 2.3.1, the adhesive component is linearly dependent on the real contact area. Consequently, for GNG2-10, a reduced adhesive contribution is expected at the beginning of the tribological test, owing to its smaller real contact area resulting from the initially finer grains. As the tribological experiment progresses, however, an increase in the real contact area is expected for GNG2-10, leading to a rise in adhesion and thus friction force, with the coefficient of friction exceeding 0.5 after approximately 240 cycles. This behavior can be attributed to grain coarsening and the likely associated decrease in surface microhardness. Due to the low sliding speed during the tribological experiments on GNG2-160 and GNG2-10, the strain rate remained low, which

allowed grain coarsening to occur within the subsurface deformation zone (DL) highlighted in Figure 4.10 [139]. Another possible reason for the immediate transition to high friction in GNG2-160 could be the more pronounced plastic subsurface deformation at the surface, caused by the larger subsurface grains with an average grain size of 282 nm, compared to 116 nm in GNG2-10, as shown in Figure 4.2. According to the Hall-Petch relationship, the lower yield strength associated with larger grain sizes in GNG2-160 promotes plastic subsurface deformation near the surface [140]. Furthermore, since approximately 150 µm more material was removed from the surface during the post-treatment in GNG2-160 than in GNG2-10, larger grain sizes were observed in the remaining GNG layer of GNG2-160. As a consequence, the tribologically induced stress field is expected to exceed the critical shear stress over a greater depth, allowing plastic deformation and thus the deformation layer (DL) to extend deeper into the material in GNG2-160, as shown in Figure 4.10.

After analyzing the different tribological behaviors of the various microstructures, the question arises: What are the main reasons for the significantly different behavior of GNG1 and GNG2?

5.1.2 Major Influences on Friction and Wear

In order to understand why the coefficients of friction and wear behaviors of GNG-0(Chen), GNG-30(Chen) and GNG1-60 differed so significantly from those of GNG2-10 and GNG2-160, and to identify the conditions required for achieving low friction, the underlying differences of the samples and tribological conditions must be systematically analyzed. Table 5.2 summarizes the differences in surface and microstructure characteristics as well as the varying experimental conditions. As shown in Figure 4.5, while the GNG-0(Chen) structure reported by Chen et al. [12] maintains a low coefficient of friction, GNG-30(Chen) and GNG1-60 displayed an initially low but steadily increasing coefficient of friction over 6000 and 7500 cycles, reaching high values similar to that observed for GNG2-160 after 50 cycles and GNG2-10 within the first 200 cycles, as observed in Figure 4.6.

Table 5.2: Overview of the key differences in various GNG samples and tribological testing conditions. The values for GNG-0(Chen) and GNG-30(Chen) are taken from Chen et al. [12].

	GNG-0 (Chen)	**GNG-30 (Chen)**	**GNG1-60**	**GNG2-160**	**GNG2-10**
Microstructure					
Microhardness [GPa]	1.8	1.4	1.5 ± 0.04	1.7 ± 0.04	3.0 ± 0.47
GNG thickness [µm]	600-700	570-670	290	660	790
Roughness *Ra* [µm]	0.03	0.03	0.07 ± 0.01	0.07 ± 0.01	0.07 ± 0.01
Test parameters					
Normal load [N]	30	30	30	2	2
Counterbody	WC-Co	WC-Co	WC-Co	Sapphire	WC-Co, Sapphire
Relative humidity [%]	45	45	45	50	50
Sliding speed [mm s^{-1}]	10	10	10	0.5	0.5
Sliding time [min]	20	20	25	400	400

One notable difference among the various specimens is that GNG2-10, unlike GNG-30(Chen), GNG1-60 and GNG2-160 exhibited almost double the **surface microhardness** of the GNG-0(Chen) microstructure. The higher hardness suggests the presence of a NG surface layer in GNG2-10. According to Chen et al. [12], the grains at a depth of 10 µm below the surface of GNG-0(Chen) exhibited an average size of 50 nm, while the average grain size measured in this work within the top 6 µm of GNG2-10 was 116 nm. The grain sizes reported in this study were determined using the line intercept method on cross-sectional images, whereas Chen et al. [12] measured the grain sizes using TEM lamellae. Given the lower resolution of the cross-sectional SEM images compared to TEM and the significantly higher surface microhardness of GNG2-10 compared to GNG-0(Chen), it is likely that the grain sizes determined in the

present work are overestimated [141]. In GNG1-60, the NG surface layer has most likely been partially or fully removed compared to the original microstructure produced by the SMGT process, as visible in Figure 4.2a). This conclusion is supported by its surface microhardness of 1.5 GPa which is similar to the one of GNG-30(Chen) of 1.4 GPa, as reported by Chen et al. [12], indicating that the NG surface layer has also been removed. Since the absence of a NG surface layer is associated with an increase in the coefficient of friction, and no grain coarsening layer develops beneath the surface during the tribological experiments, but instead the DRX layer formed directly below the delaminating tribo-layer, similar behavior can be assumed for GNG1-60 [12]. Despite the higher surface hardness compared to GNG-30(Chen) and GNG1-60, the coefficient of friction in GNG2-160 rapidly increased to 0.6 within the first 50 cycles, whereas GNG-30(Chen) and GNG1-60 reached values of around 0.5 only after 6000 and 7500 cycles, respectively. Given that GNG2-160 exhibited a comparable surface microhardness to GNG-0(Chen), it can be expected that the surface contained a similar amount of nanograins. In contrast to GNG2-160, however, GNG-0(Chen) maintained a nearly stable coefficient of friction of approximately 0.37 over 6000 cycles. In summary, although GNG2-10 likely had a higher amount of NGs at the surface compared to GNG-0(Chen), and GNG2-160 contained more NGs than GNG-30(Chen) and GNG1-60, both GNG2 samples exhibited higher friction. While the absence of a sufficiently developed NG surface layer was a contributing factor to why GNG-30(Chen) and GNG1-60 do not maintain a consistently low coefficient of friction throughout the test duration, the observed increase in friction, particularly in GNG2-10, cannot be explained by differences in microhardness and thus surface NG content.

The **GNG layer thickness** likewise does not explain the differences in friction behavior. This is due to the fact that GNG2-160 showed a GNG depth comparable to GNG-0(Chen), whereas GNG2-10 possessed a thicker GNG layer. Nevertheless, GNG2-160 and GNG2-10 exhibited almost twice the coefficient of friction of GNG-0(Chen). Thus, the GNG thickness cannot be the cause of the increased coefficient of friction. This is further supported by GNG1-60, whose GNG layer thickness of around 290 µm was less than half that of GNG2-160 and GNG2-10, while still displaying a lower coefficient of friction. Additionally, despite the thicker GNG layer in GNG-30(Chen), GNG1-60 exhibited a lower coefficient of friction over 6000 cycles under the same testing conditions, as shown in Figure 4.5, confirming that the total GNG

thickness does not significantly influence the friction behavior. To investigate whether the tribologically induced plastic deformation occurred within the gradient layer for all samples, the tribological stress fields can be compared with the different GNG layer thicknesses of the samples. A widely used model for describing the tribological stress field was developed by Hamilton [142]. In this approach, the classical Hertzian contact model is extended by superimposing a shear stress component in the sliding direction on the normal plane, with the magnitude of this shear stress being proportional to the experimentally determined coefficient of friction. The Hamilton model is linear elastic and static, and it has frequently been applied to estimate the extent of the plastic zone beneath sliding contacts. The various tribologically tested samples were divided into three categories: For GNG-0(Chen), the coefficient of friction remained nearly constant at 0.37 over 6000 cycles. In contrast, GNG-30(Chen) and GNG1-60 exhibited an increasing coefficient of friction during 6000 cycles, reaching a value around 0.50. For GNG2-10 and GNG2-160, a similar coefficient of friction of 0.57 was observed after 1000 cycles. Unlike the other three samples, they were tested under mild tribological loading conditions. For these three cases, the corresponding stress tensors were calculated according to the Hamilton model, as shown in Figure A.10 to Figure A.12. As the shear stress component $\tau_{SD\text{-}ND}$, which acts along the sliding direction (SD) parallel to the surface and perpendicular to the normal direction (ND), is expected to be the primary driving force for dislocation motion, it is shown for comparison across the different specimens in Figure 5.3 [143]. According to Chen et al. [12], a tribologically induced change in the microstructure of GNG-0(Chen) was observed down to a depth of approximately 90 µm. However, since the tribologically induced stress field extends to depths greater than 400 µm, as shown in Figure 5.3, and at a depth of 90 µm the maximum shear stress reaches about 270 MPa, it is likely that regions deeper than 90 µm were also affected by the tribological loading. Since the main changes in the tribologically affected microstructure in GNG-30(Chen) also appears to be located within approximately the top 100 µm, according to Chen et al. [12], and GNG1-60 shows similar tribological behavior, it can be assumed that plastic deformation most likely also occurred primarily within the gradient layer of GNG1-60, which has a thickness of around 290 µm. At a depth of 100 µm, a maximum shear stress of approximately 280 MPa is present, as shown in Figure 5.3, whereas at the maximum depth of the gradient layer in GNG1-60 the shear stress is expected to be around 60 MPa. GNG2-160

and GNG2-10 exhibit shear stresses of around 40 MPa at a depth of 100 µm, and since the shear stress at a depth of 400 µm is expected to be below 20 MPa, while GNG2-160 and GNG2-10 have GNG layer thicknesses of approximately 640 µm and 790 µm, this indicates that the tribologically induced plastic deformation in both samples occurred within the gradient layer. Consequently, since plastic deformation was most likely predominantly localized within the gradient layer in all samples, the variations in GNG layer thickness probably did not account for the observed tribological differences.

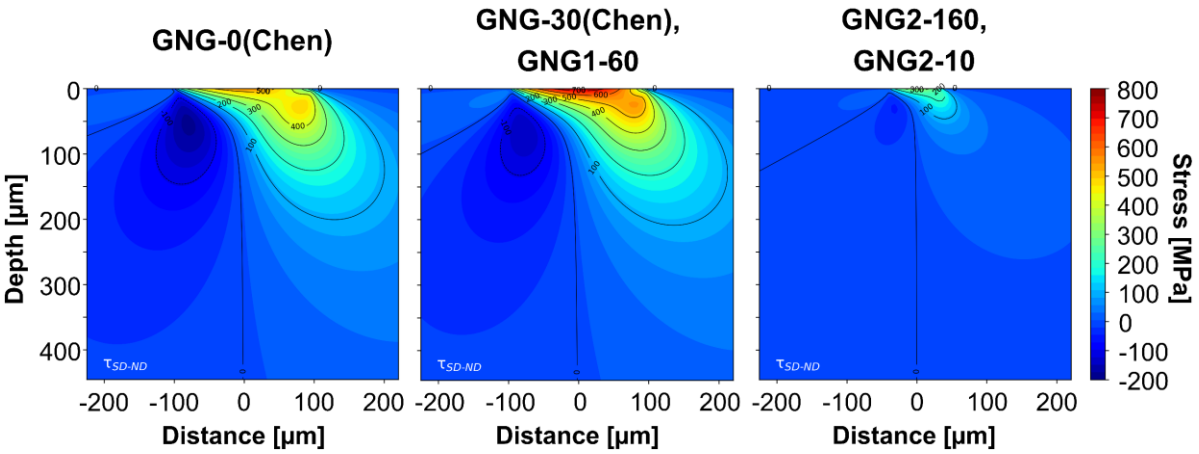

Figure 5.3: Stress distribution maps of the projected shear stress component $\tau_{SD\text{-}ND}$ (SD: sliding direction, ND: normal direction) calculated using the Hamilton model. For GNG-0(Chen), GNG-30(Chen), and GNG1-60, a WC-Co counterbody with a normal force of 30 N was used; the coefficient of friction was 0.37 for GNG-0(Chen) and 0.50 for GNG-30(Chen) and GNG1-60. For GNG2-160 and GNG2-10, a sapphire counterbody, a normal force of 2 N, and a coefficient of friction of 0.57 were used.

Another characteristic that varies between the different sample types is the **surface roughness**. GNG-0(Chen) and GNG-30(Chen) showed less than half the surface roughness of GNG1-60, GNG2-160, and GNG2-10. After the SMGT process, GNG2 exhibited a *Ra* value of 1.07 µm ± 0.01 µm, respectively, exceeding the *Ra* value of 0.2 µm reported by Chen et al. [12] for their GNG sample, as demonstrated in Table 4.1. For both GNG and GNG2 samples, a total indentation depth of 240 µm was selected for the WC-Co sphere during SMGT processing. While Chen et al. [12, 29] used a feed rate of 3 mm min^{-1} for surface treatment, the samples in this study were processed at 18.9 mm min^{-1}. However, the rotation speeds of the samples were comparable, with 600 rpm in the experiments of Chen et al. [12] and 660 rpm in this study. Due to the lower feed rate of the WC-Co sphere, the resulting spiral-shaped surface grooves, as visible in Figure 4.3a), were less pronounced. This is because the

slower lateral movement of the sphere caused the processing paths to overlap more densely, leading to a smoother surface texture with less pronounced spiraling. GNG1, on the other hand, exhibited lower surface roughness than the GNG sample directly after the SMGT process, with a *Ra* value of 0.13 µm ± 0.01 µm. Nevertheless, the reduced indentation and thus lower total plastic deformation depth of the WC-Co sphere during the SMGT processing of GNG1, compared to GNG and GNG2, resulted in a shallower GNG layer. Another reason for the high surface roughness of GNG2 could be that during the SMGT process, the copper rod was not fully immersed in nitrogen but instead had nitrogen poured over it. Insufficient surface cooling during the SMGT treatment can result in localized grain coarsening. In these regions, strain localization may occur, potentially leading to crack formation at the surface and increased roughness. The relatively large range of surface microhardness values of GNG2-10 shown in Figure 4.4 may be indicative of an inhomogeneous grain refinement at the surface. This assumption is supported by the fact that in Figure 4.2c), in addition to small grains below 30 nm, grains up to 300 nm were also detected beneath the GNG2-10 surface. The non-uniform grain refinement combined with the effects of the higher sliding speed of the WC-Co sphere during SMGT, may have further contributed to the elevated surface roughness.

The following surface post-treatments reduced the surface roughness of GNG-0(Chen) and GNG-30(Chen) to about half of GNG1-60, GNG2-160 and GNG2-10. Nevertheless, GNG1-60 demonstrated a lower coefficient of friction over the course of 7500 cycles than GNG-30(Chen) over 6000 cycles. This indicates that a surface roughness of *Ra* = 0.07 µm ± 0.01 µm, compared to *Ra* = 0.03 µm for GNG-30(Chen), does not result in an increased coefficient of friction. GNG2-10 and GNG2-160 demonstrated the same surface roughness of *Ra* = 0.07 µm ± 0.01 µm as GNG1-60. However, they showed a clearly elevated coefficient of friction throughout the sliding cycles. Therefore, it can be assumed that the high coefficients of friction in GNG2-160 and GNG2-10 were also not caused by their surface roughness. In summary, the properties of the various GNG specimen do not provide an explanation for the high coefficient of friction in GNG2-160 and GNG2-10, suggesting that the experimental conditions are the more probable cause.

Accordingly, the impact of the test conditions on the tribological behavior is analyzed, starting with the **normal force**. Based on the findings of Li et al. [14], a normal load of 5 N, a 1 mm

stroke, a sliding speed of 10 mm s^{-1}, and a 10 mm WC-Co sphere result in low coefficients of friction for both coarse-grained (CG) and GNG samples during the initial 60 min of tribological testing, corresponding to approximately 18000 reciprocating cycles. Under normal loads of 10 N, the coefficient of friction in CG copper increases to high values of around 0.6 [14]. In contrast, GNG copper with a NG surface layer maintains a low steady-state coefficient of friction under normal loads between 5 and 25 N. However, at 25 N, the coefficient of friction gradually increases over time, reaching a high value of 0.6 after 18000 cycles. This indicates that increasing the normal load beyond 5 N leads to higher friction. Chen et al. [12] tested not only CG copper with an average grain size of 20 µm but also NG copper with a mean grain size of 75 nm, and also found that both exhibit high coefficients of friction between 0.6 and 0.8 at a normal load of 10 N or higher. However, at a normal load of 2 N, it could be possible that the stress cannot be distributed throughout the GNG layer because the applied load is too low. As a result, the stress might be concentrated only within the NG surface layer. Consequently, under tribological loading, the sample may not behave according to the GNG microstructure but rather like a NG copper specimen in the contact region. According to Prasad et al. [84], the coefficient of friction of NG nickel in dry nitrogen with grain sizes between 20 and 100 nm is highly dependent on the strain rate and the maximum contact pressure. While at high sliding speeds, delamination and thus a high coefficient of friction were observed, at a sliding speed of 0.5 mm s^{-1}, maximum contact pressures of up to 1.1 GPa still resulted in a low coefficient of friction [12, 83, 110]. This behavior is attributed to the development of a 25 to 50 nm thick ultrafine-grained layer at the contact surface with grain sizes between 5 and 10 nm, where, according to the inverse Hall-Petch relationship, the subsurface deformation mechanism transitions from dislocation-mediated deformation to strain-rate dependent grain boundary-mediated deformation [144]. According to Mishra et al. [145], below a critical grain size in the inverse Hall-Petch regime, each grain cannot sustain more than one dislocation making dislocation pile-up mechanisms ineffective. Furthermore, they reported a decreased coefficient of friction with decreasing grain size down to 8 nm. While Prasad et al. [146] suggested grain rotation as a possible deformation mechanism, Argibay et al. [88] attributed shear accommodation to grain boundary sliding. In order to achieve low friction in pure metals, the rate of defect formation and grain refinement within the sliding shear layer must exceed the rate of grain growth and

defect annihilation, leading to significant grain refinement and inverse Hall-Petch softening [147]. However, stress assisted grain growth occurs over time, promoting a transition back to dislocation mediated plasticity [148]. This indicates that suppression of grain growth is a key mechanism for extending the low-friction regime associated with grain boundary sliding in ultrafine-grained metals to conditions involving higher stresses and prolonged contact times [147]. While Prasad et al. [84] observed that at a sliding speed of 0.5 mm s^{-1} in dry nitrogen, a maximum contact pressure of 1.1 GPa in nickel still resulted in low friction, the present study showed that even with a lower maximum Hertzian contact pressure of 581 MPa, a high coefficient of friction was measured. A possible reason for this could be the tribo-oxidation in this study, in contrast to the work of Prasad et al. [84], who conducted their experiments in dry nitrogen [147, 149]. In conclusion, the GNG2-160 and GNG2-10 samples may have behaved like NG specimens if, under a normal load of 2 N, the stress was localized only within the subsurface NG layer. In this case, a friction-reducing ultrafine-grained layer could form at the surface during the tribological loading, but it would inherently create numerous additional diffusion pathways for oxygen. These paths would promote tribo-oxidation and thus prevent the stability of the friction-reducing ultrafine-grained layer. In summary, Figure 5.4 shows that under the prevailing tribological conditions of GNG2-160 and GNG2-10, namely in air and at low sliding speeds, a low coefficient of friction most likely cannot be achieved, neither with a normal force so low that only the topmost NG layer is affected, nor with a normal force high enough for the stress to be distributed across the GNG layer. Consequently, the normal force is probably not the main factor responsible for the high coefficient of friction in GNG2-160 and GNG2-10.

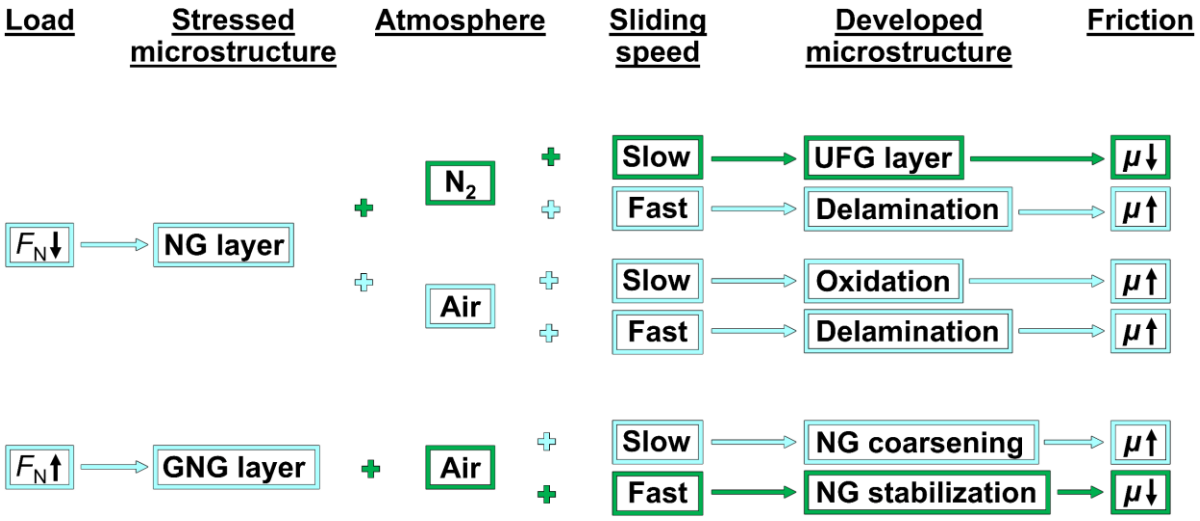

Figure 5.4: Schematic illustration of the influence of the normal force F_N on the stress distribution in the gradient nano-grained (GNG) sample during tribological experiments under different atmospheric conditions and sliding speeds, along with the resulting microstructural evolution and coefficients of friction μ (NG: nano-grained, UFG: ultrafine-grained).

Subsequently, the influence of the **counterbody** and **relative humidity** on the tribological performance is examined. Friction tests on GNG2-10 using both WC-Co and sapphire counterbodies, conducted under otherwise identical test conditions, revealed that the type of counterbody had no significant influence on the coefficient of friction, as shown in Figure 4.6. Therefore, the absence of stable low friction in GNG2-10, as observed in GNG-0(Chen), cannot be attributed to the use of a sapphire sphere as the counterbody. Similarly, the difference in relative humidity across all experiments was limited to 5 % and does not sufficiently explain the observed differences in friction behavior. As shown in Figure A.7 in the Appendix, an increase in relative humidity of 15 % led to a rise in the coefficient of friction of porous copper of approximately 0.02. This indicates that a 5 % difference did most likely not account for the much larger difference in coefficients of friction of around 0.2 observed between GNG-0(Chen) and GNG2-10.

The remaining unresolved factors distinguishing the samples with low and high coefficients of friction are the sliding speed of the sphere during testing and the total test duration, which depends on both the sliding speed and the stroke length. In polycrystalline copper with grain sizes between 30 and 40 µm, Rau [94] demonstrated that the tribological **test duration** plays a more significant role than the sliding speed with regard to tribo-oxidation and, consequently, the tribological behavior. This observation was made under testing conditions similar to the

mild tribological loading condition applied in this study. The tribo-oxide was found to grow linearly with the test duration. Under conditions of short stroke length or high sliding speed, repeated passes of the sphere interrupt diffusion pathways, reducing the extent of oxygen penetration into the material primarily via grain boundary diffusion in a fine-grained microstructure. Accordingly, the time available for diffusion is of primary importance. Under the tribological conditions described by Chen et al. [12] and Li et al. [14], GNG samples show no tribo-oxidation even at normal loads up to 50 N, whereas CG samples exhibit no tribo-oxidation only at loads up to 5 N. It can thus be concluded that tribo-oxides are typically observed after tribological loading when the coefficient of friction is high, meaning around 0.65 [13]. In GNG microstructures and CG under low normal loads of at least 5 N, the wear debris is minimal. In the case of GNG samples, the depth-dependent yield strength under tribological loading leads to a distribution of plastic deformation beneath the surface rather than being localized at the surface [12]. Consequently, only little plastic deformation occurs at the surface, which limits the formation of deformation-induced high diffusivity pathways for oxygen such as dislocations, grain and phase boundaries as described by Rau et al. [70], and thereby reduces tribo-oxidation. In addition to the stress distribution that reduces stress concentration at the surface, the presence of surface nanograins leads to a higher density of grain boundaries. Because of the small grain size, dislocations reach grain boundaries more quickly, resulting in a faster accumulation of dislocations at these boundaries. At the same time, the high density of grain boundaries means that fewer dislocations are required to generate a significant dislocation pile-up, effectively inhibiting further dislocation motion due to overlapping stress fields of individual dislocations. According to Rau et al. [94], the sliding of the sapphire sphere removes the native oxide layer on the copper surface, allowing oxygen to diffuse along the dislocation cores. Upon subsequent sliding, the motion of dislocations under the tribologically induced stress fields causes them to detach from the previously diffused oxygen, after which they are free again and can take up new oxygen. When dislocations accumulate at obstacles such as grain boundaries, they can no longer move and detach from the already diffused oxygen, which prevents the creation of free pathways for additional oxygen uptake. Therefore, an increased grain boundary and dislocation density and thus restricted dislocation mobility can lead to a reduced number of cleared diffusion pathways and consequently to reduced tribo-oxidation. In CG and GNG copper, under a high sliding

speed of 10 mm s^{-1}, a small stroke of 1 mm, and consequently a short test duration, the formation of tribo-oxides and their removal as wear debris are likely in equilibrium, even at a normal force of 5 N [14]. Since the wear scar of the GNG sample under these conditions is shallow, it is unlikely that a large amount of tribo-oxide was formed and subsequently removed. Thus, it could be expected that in GNG structures, when tested under even lower normal loads in this study, resulting in reduced stress and plastic deformation, no tribo-oxidation would be observed after tribological testing. However, the GNG samples tested under mild tribological loading conditions exhibited pronounced tribo-oxidation, as shown in Figure 4.10d) and f). The formation of tribo-oxides is associated with the dissipation of mechanical energy, which in turn is linked to an increase in friction [1]. Consequently, the low level of tribo-oxidation in CG microstructures at even higher normal loads is most likely partly caused by the short test duration resulting from the small stroke and high sliding frequency, which limits the time available for diffusion and thereby restricts the depth to which oxygen can penetrate into the material [94]. Since, under mild tribological loading conditions, a lower sliding speed of 0.5 mm s^{-1} was combined with a larger stroke of 6 mm, and as a result a longer test duration, pronounced tribo-oxidation could be observed in the GNG microstructures. Thus, the observed significant tribo-oxide formation, together with resulting other energy-dissipating phenomena such as subsurface cracking and surface delamination, which are all associated with a high coefficient of friction, is probably not primarily governed by the microstructure. Instead, the test duration is most likely an important factor.

In addition to test duration, **sliding speed** also plays a crucial role. The following interpretations are valid under the assumption that the applied normal load is sufficient to distribute the stress throughout the GNG layer. In NG nickel microstructures, the correlation between higher coefficient of friction and increased sliding speeds points to a pronounced strain-rate dependence of the delamination process [12, 112]. In contrast, in GNG Cu samples, increased strain rates during tensile testing were found to suppress grain coarsening in the NG surface layer, as demonstrated in Figure 5.5a), indicating that grain coarsening kinetics are primarily stress-driven [110]. As shown in Figure 5.3, the stress is highest in the topmost surface layer for all specimens and their respective tribological loading conditions. Consequently, the strain rate is expected to be highest in this region and to decrease gradually

with increasing depth below the sliding interface. This may explain why Chen et al. [12, 150], under severe tribological loading conditions generating very high strain rates at the surface, observed grain coarsening only at depths of 1 µm and below. In the immediate surface region, the high strain rates likely stabilize the NG structure, while at greater depths grain growth is favored due to lower strain rates. Accordingly, the mechanical response in this regime is governed by two competing mechanisms: strain softening and dislocation hardening [12]. According to Chen et al. [29], a stable microstructure at the submicron scale emerges when the generation and movement of dislocations, along with their interactions with grain boundaries, are balanced by recovery processes such as dislocation annihilation and grain boundary migration [29]. In addition to the strain-rate-induced stability of the surface NG layer, the tribological behavior observed in GNG-0(Chen) by Chen et al. [12] can be explained by the gradual distribution of the applied stress across the depth of the GNG structure resulting from the gradient in the elastic limit. This gradient causes a larger subsurface region to exceed the yield strength under the tribologically induced stress field than in homogeneous NG samples, leading to plastic deformation over a greater depth and thereby generating a smaller gradient in plastic strain. In NG samples, strain localization at the surface generates a steep strain gradient, which promotes surface cracking [29]. With increasing sliding cycles, the cracked regions detach and form wear particles that cold-weld to the surface, forming a nanostructured tribolayer whose repeated formation and delamination lead to a high coefficient of friction and increased surface roughness. This implies that a low plastic strain gradient is essential for maintaining a low coefficient of friction.

The low strain rate used in this study during the tribological tests, such as 0.5 mm s^{-1} for GNG2-10 and GNG2-160, may have promoted pronounced grain coarsening, potentially occurring even at the immediate surface, as demonstrated in Figure 5.5b). Furthermore, since grain boundary migration and grain boundary sliding are time-dependent processes, with migration relying on mass transport along the boundary as atoms change their crystallographic affiliation, and sliding being controlled by localized atomic shuffling events that occur at a finite rate, a reduction in strain rate facilitates the activation of both mechanisms in the NG surface layer of GNG2-10 and GNG2-160 [151, 152]. As a result, plastic subsurface deformation and thus shear accommodation can occur not only through dislocation-mediated mechanisms, but also via grain boundary processes [153]. Jiang et al. [154] observed a strong

strain rate sensitivity in copper grains with a diameter of 30 nm at room temperature, indicating a transition in the deformation mechanism to grain boundary sliding or grain boundary diffusion occurring at low strain rates. Reducing the sliding speed in the tribological tests lowers the strain rate, which facilitates plastic deformation in the NG surface layer of the GNG samples through grain boundary sliding and grain boundary migration. Furthermore, the lower strain rate promotes grain coarsening at the surface, which decreases the local yield strength and thereby enables additional plastic deformation. Consequently, more plastic strain is accommodated at the surface, leading to an increased plastic strain gradient across the depth. In GNG copper, the breakdown of uniform plastic strain accommodation results in shear-induced surface roughening, which triggers the transition from low-to-high friction [13, 111]. According to Chen and Han [13], surface roughening increases friction and facilitates crack initiation and possible delamination at the surface. At the same time, the formation of a tribo-oxidation layer accompanies these surface changes, contributing further to the evolution of friction and wear behavior. The observed microstructural and tribological evolutions of GNG2-160 and GNG2-10 can thus be attributed not only to the influence of test duration, which contributes to the tribo-oxidation and thus cracking and delamination, but also to the low sliding speed.

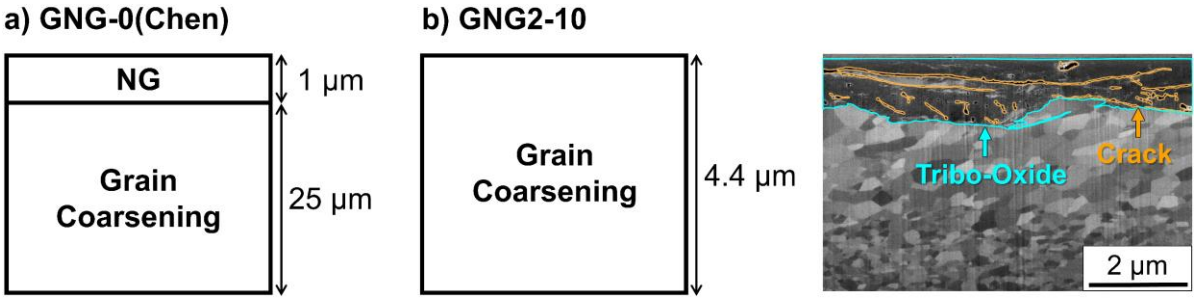

Figure 5.5: Illustration of the subsurface microstructure evolution of a) GNG-0(Chen), according to Chen et al. [12], under a normal load of 30 N, with a 1 mm stroke and sliding speed of 10 mm s^{-1} over 10000 cycles, and b) GNG2-10 under a normal load of 2 N, a stroke of 6 mm and a sliding speed of 0.5 mm s^{-1} over 1000 cycles.

In addition to the GNG structures, the NG and CG copper microstructures also show dependencies of the coefficient of friction on **test duration and sliding speed**. Li et al. [14] observed that applying a normal load of 5 N with a 1 mm stroke length at a sliding speed of 10 mm s^{-1} using a WC-Co sphere with a diameter of 10 mm led to low coefficients of friction of around 0.3 for CG copper during 18000 sliding cycles. The low coefficient of friction is

attributed to surface condition being the dominant factor in frictional increase. At a normal load of 5 N, the wear debris generated was minimal and could be largely removed from the contact zone. However, as shown by Lehmann et al. [69], CG copper with a grain size of 40 µm reached a coefficient of friction of 0.5 within the first sliding cycles under a normal load of 1.5 N, a stroke of 12 mm, a sliding speed of 0.5 mm s^{-1}, and using a sapphire sphere with a diameter of 10 mm. Thus, the reduction in sliding speed combined with the increased test duration, also due to the significantly longer stroke, already leads to a considerable increase in the coefficient of friction of CG copper, even at much lower normal forces. Fine grained samples produced by high-pressure torsion (HPT) with an average grain size of around 229 nm exhibit a rise in the coefficient of friction to above 0.5 within the first 100 sliding cycles, as shown in Figure 5.6 [155]. The cylindrical sample had a diameter of 60 mm and a thickness of 5 mm, and was processed at room temperature under a pressure of 2 GPa for 8 rotations, resulting in a shear strain of 301.59 at the edge of the sample. The tribological experiments were conducted under mild loading conditions, meaning a normal load of 2 N, with a 6 mm stroke, a sliding speed of 0.5 mm s^{-1}, a sapphire sphere as counterbody with a diameter of 10 mm, and in air at a relative humidity of 50 %. It is likely that tribo-oxidation also prevented the formation of the friction reducing ultrafine-grained layer in this case. To verify this, experiments should be conducted in nitrogen. Consequently, grain boundary-mediated plasticity, which was linked to decreased friction in NG nickel, did not become the dominant subsurface deformation mechanism under these conditions. To summarize, a low coefficient of friction could not be achieved with either the CG or the fine-grained copper samples under mild tribological loading conditions over 1000 cycles.

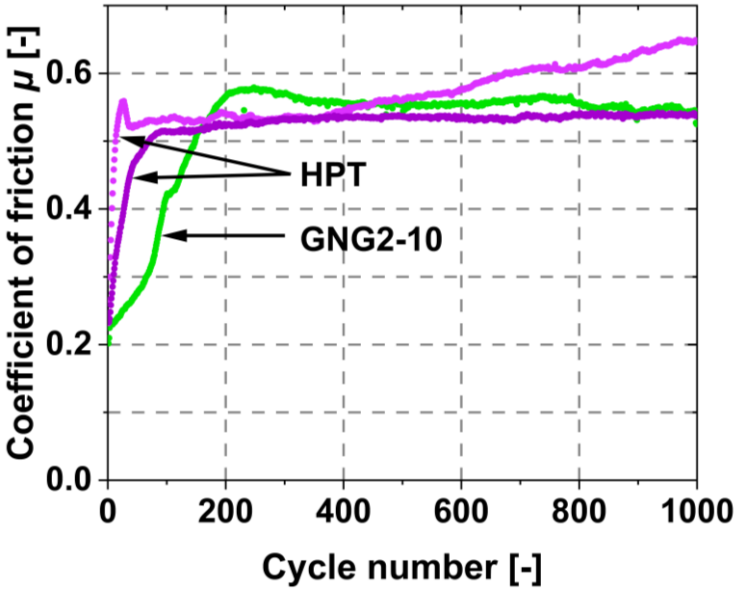

Figure 5.6: Evolution of the coefficients of friction over 1000 sliding cycles for the surface mechanical grinding treated GNG2-10 and fine grained copper prepared by high-pressure torsion (HPT), tested under identical conditions (normal load: 2 N, sliding speed: 0.5 mm s^{-1}, stroke: 6 mm, sapphire sphere as counterbody, 50 % relative humidity) [155].

This allows the first research question to be answered whether a GNG surface layer can reduce the coefficient of friction under mild tribological loading conditions and how the layer thickness and surface grain size affect this behavior. It was found that neither variation in the thickness of the GNG layer nor the grain size at the surface led to a reduction in friction over the course of 1000 sliding cycles under mild tribological conditions. In summary, the observed differences in tribological behavior of GNG-0(Chen), GNG-30(Chen), and GNG1-60 on the one hand, and GNG2-10 and GNG2-160 on the other, were most likely not due to the GNG microstructure itself but rather to variations in both test duration and the sliding speed during the tribological experiments. According to Padilla et al. [112] and Prasad et al. [84] a mild plowing mechanism typically occurs in NG metals when tested in a dry nitrogen atmosphere only under low tribological stresses, such as low sliding speeds and low normal loads, or in the presence of lubrication. Exceeding the yield strength in CG and NG samples due to high contact stress leads to the loss of the low-friction regime [13]. This highlights the limitations of NG and CG metals under severe tribological conditions. Therefore, GNG structures were developed to enhance tribological performance under severe sliding conditions. However, the results of this study indicate that under mild tribological loading conditions with low macroscopic loads and low sliding speeds, GNG microstructures exhibit a high coefficient of

friction. This can be attributed to the fact that, while tribo-oxidation and grain coarsening in GNG copper are generally suppressed under short test durations and high sliding speeds, this work revealed pronounced tribo-oxide formation as well as enhanced plastic deformation and grain coarsening directly at the surface under extended test duration and reduced sliding speed. The composition of the tribo-oxide layer, including the presence of Cu_2O as well as its homogeneity, is more strongly influenced by the testing duration than by the microstructure alone. High sliding speeds tend to stabilize the NG surface layer due to the high strain rates they impose, whereas lower speeds likely allow for enhanced plastic deformation at the surface through grain boundary sliding and grain boundary migration, as well as through grain coarsening, which in turn promotes increased dislocation-mediated plasticity. This increase in plastic deformation at the surface likely leads to a higher strain gradient. The resulting non-uniform plastic strain accommodation causes, according to Chen and Han [13], shear-induced surface roughening, which in turn promotes the transition from low to high friction. An increase in surface roughness due to a steep strain gradient is also observed in NG samples, where the pronounced gradient leads to surface cracking and delamination [29]. Both the significant tribo-oxidation resulting from enhanced testing duration and the increased strain gradient caused by low sliding speed promote subsurface cracking and delamination. These mechanisms increase energy dissipation during sliding and are associated with a higher coefficient of friction. Although the GNG layer depth and surface grain size did not account for the differences observed in the coefficient of friction, they may have influenced the depth of the subsurface deformation layer. Samples with larger surface grains before the tribological tests exhibited greater tribologically-induced deformation depths, as the stress field likely exceeds the critical shear stress across a greater depth, enabling plastic deformation to occur further below the surface and leading to a deeper deformation layer. However, no significant differences in the overall topographical deformation depth or wear behavior were observed. These findings suggest that the tribological performance of GNG copper may be governed less by the initial microstructure and more by the interplay between sliding speed and test duration under tribological loading. A similar behavior of the coefficient of friction is observed for both CG and NG copper. While CG copper exhibits low friction at high sliding speeds and short test durations under a normal load of 5 N, both CG and NG copper show

significantly higher coefficients of friction at lower sliding speeds and extended test durations, even at reduced normal loads of 1.5 N and 2 N, respectively.

Since no reduction in the coefficient of friction was achieved with GNG microstructures under the mild tribological loading conditions used in this study, the following analysis examines whether the introduction of porosity could contribute to improving the tribological behavior.

5.2 Tribological Performance of Porous Specimens

5.2.1 Influence of Pore Size and Porosity

In the following section, the tribological behavior of porous copper samples under mild tribological loading conditions is investigated. In order to explore the influence of pore size and porosity on the tribological behavior, friction data collected during the experiments and analyses of the specimens before and after tribological testing were used to gain insight into the underlying causes of the observed differences. While no significant anisotropy in grain orientation was observed at the specimen surfaces, as shown in Figure 4.12 and Figure A.4, it should be noted that the porosity varied across the specimen. Thus, the overall porosity did not correspond to the prevailing porosity at the locations of the tribological tests. The tribological experiments were all conducted in the center of the specimens due to the process-induced variations in pore distribution within the samples, as shown in Figure 3.7. The temperature profile across the sample during the field assisted sintering (FAST), illustrated in Figure 2.4, shows that the highest temperature occurs in the center of the specimen. In this study, graphite foils were used both as the die lining and between the punches and the powder. Consequently, the powder was not surrounded by an insulating liner, but by graphite with an electrical resistivity of synthetic graphite of $4.31 \cdot 10^{-5}$ Ωm [156]. Copper, on the other hand, has an electrical resistivity at room temperature of approximately $1.7 \cdot 10^{-8}$ Ωm [157]. However, at the beginning of the process, the copper powder exhibits a higher electrical resistance due to native oxide layers on the particle surfaces [32]. According to Chawake et al. [32], after dielectric breakdown of the oxide films, the resistance decreases by nearly an order of magnitude, after which the current flow through the matrix becomes negligible. Thus, the highest current density occurs in the center of the specimen, resulting in the greatest heating and consequently densification in this region. Moreover, the surrounding environment

acts as a heat sink for the die, which additionally accounts for the lower temperatures at the edges.

Evaluation of the coefficients of friction, as shown in Figure 4.14, along with the microstructural evolution during tribological testing, reveals that unlike the sintering pore size and the additional CIP step, the number of sintering pores had a significant influence. The main differences are summarized in Table 5.3.

Table 5.3: Overview of the coefficients of friction and the main differences in the microstructural evolution of the samples with different porosities under mild tribological loading conditions, meaning a normal force of 2 N, a sliding speed of 0.5 mm s^{-1}, a stroke length of 6 mm, after 1000 cycles.

Sample	Coefficient of friction (1000 cycles)	Microstructural evolution
Few Sintering Pores 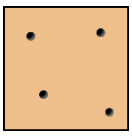	**0.57 – 0.70**	Subsurface deformation, Tribo-oxidation } high Cracking Delamination Pile-up formation Grooving in the wear track
Many Sintering Pores 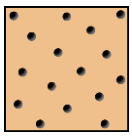	**0.27 – 0.29**	Subsurface deformation, Tribo-oxidation } low

The differences in coefficients of friction identified in Figure 4.14 between specimens with many and few sintering pores could be attributed to variations in the evolution of the respective subsurface microstructures. This also includes surface delamination occurring during the tribological tests, as shown in Figure 4.15a), b) and d). Delamination, observed in the samples with elongated dark features (F2) identified as cracks in Figure 4.16, was likely caused by these tribologically induced cracks. Since Rau et al. [90] identified similar features, it can be assumed that the small, round black areas are pores, and the dark gray area (F1) represent the **tribo-oxidation** layer. Both were formed during the tribological experiments. The large dark features in Figure 4.16e) and f) are process-induced sintering pores and were

already present before the tribological tests. The tribo-oxidation layer, also visible in light microscopy images of the wear tracks for all specimen types in Figure 4.17, could be identified by the differently colored surface. During tribological loading, Kirkendall pores most likely form at the copper-oxide interface due to the faster diffusion of copper ions compared to oxide ions [90, 95]. With prolonged oxidation, pores develop along diffusion pathways [90]. As the interface between copper and oxide progressed deeper into the substrate with increasing tribo-oxidation, pores and cracks appeared at varying depths within the tribo-oxide layer after 1000 sliding cycles. These pores are highlighted at the oxide-copper interface in Figure 4.16c). Another reason for the delamination could be the higher hardness of the tribo-oxide, as Cu_2O has a hardness of 2.94 ± 0.02 GPa, while heat-treated, electropolished Cu-OFHC exhibits a hardness of 42 HV0.1, which corresponds to approximately 0.41 GPa. This makes the tribo-oxide more prone to crack initiation when exceeding a critical thickness of about 1 to 3 µm according to Quinn [158], compared to the bulk material [69, 91]. In addition to the Kirkendall porosity, increased void and crack formation could occur due to dislocation pile-ups at harder phases, such as tribo-oxides, which could lead to surface delamination [66]. This behavior may arise as under a strong dislocation pile-up, the leading dislocations are forced so closely together that they effectively behave like a single dislocation with a large Burgers vector [159]. Consequently, a substantial amount of deformation has to be accommodated near this effective dislocation, which occurs through dilatational strain. If the Burgers vector becomes large enough that the atoms are displaced so far apart that they no longer interact with each other, a crack is formed. Cracks can also form through decohesion at the interface between the matrix and the harder phase due to the plastic flow of the matrix, which represents a key mechanism of void formation [66]. Moreover, cracks can arise when the harder phase itself fractures under the stress concentration generated by the dislocation pile up. Alpas et al. [160] likewise reported that pores and consequently cracks can form in regions where the strain-hardening limit is exceeded.

In the case of few sintering pores, specimens with large pores (FBP) exhibited more pronounced tribo-oxidation, illustrated in Figure 4.16, and a higher degree of grain refinement in the deformation layer (DL) beneath the surface compared to those with small sintering pores, as visible in Figure 4.18 and Figure 4.19. This may result from a reduced real contact area between the specimen and the sapphire sphere, due to the higher porosity in FBP, as

shown in Figure 4.11 and Figure 5.7. This reduced contact area most probably led to increased surface stresses, resulting in a greater number of tribologically induced dislocations and grain boundaries, which both serve as diffusion paths for oxygen atoms [161]. Nevertheless, samples with few small sintering pores which were additionally cold isostatically pressed (FSPC) exhibited delamination and, consequently, more pronounced tribo-oxidation than samples with few small sintering pores (FSP) despite the smaller pores. Similarly, specimens with few big sintering pores that experienced an additional cold isostatic pressing step (FBPC) exhibited a more pronounced tribo-oxidation than FBP samples, as demonstrated in Figure 4.16. Since the additional cold isostatic pressing (CIP) of the sintered specimens resulted in reduced porosity, as shown in Figure 4.11, it can be assumed, according to James [162], that further deformation occurred within the microstructure, leading to an increased dislocation density. A higher initial dislocation density might thus accelerate the void and crack formation induced by dislocation-pile-ups at the copper-oxide interface during the tribological loading and thus explain the crack formation (F2) in the tribo-oxide of FSPC and FBPC, as shown in Figure 4.16. Similarly, Alpas et al. [160] observed that extensive plastic strains in the deformed zone promote failure.

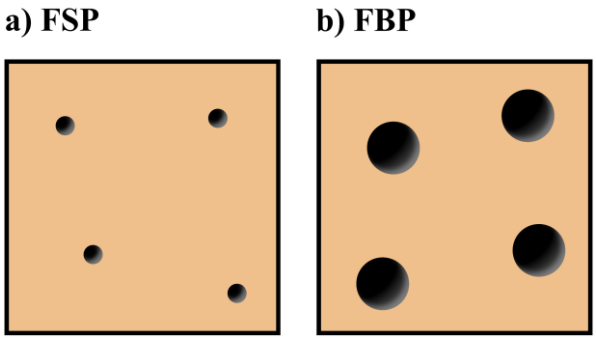

Figure 5.7: Schematic representation of surfaces with a) few small pores (FSP) and b) few big pores (FBP), which are in contact with the sphere during tribological testing. The orange region illustrates the real contact area, while the black circles represent the sintering pores.

In contrast to low-porosity specimens, those with many sintering pores demonstrated only a small tribo-oxidation zone, as visible in Figure 4.16e) and f). The reason for this might be the barely present subsurface deformation, as shown in Figure 4.18. According to Rau et al. [90], the generation and motion of dislocations can act as diffusion paths for oxygen atoms. Therefore, the more pronounced tribo-oxidation observed in specimens with few sintering pores could be attributed to the enhanced subsurface deformation. The degree of deformation

in high-porosity specimens also leads to differing tribo-oxidation behaviors. Among these, the sample with larger pores exhibited a more pronounced tribo-oxidation layer, which may be related to the larger grains and the associated lower Hall-Petch strengthening, resulting in increased plastic deformation and, consequently, the creation of new diffusion paths for oxygen atoms. The light microscopy images in Figure 4.17e) and f) reveal a reddish-blue shimmering oxide, characteristic of Cu_2O, which typically forms first during the oxidation of copper [70, 163, 93]. The tribo-oxide preferentially forms at surface defects as islands growing with advancing oxidation into semi-circular features into the bulk material [91]. However, as some copper-colored areas remained visible in Figure 4.17e) and f), and as indicated by the shallow depth of the blue-highlighted tribo-oxide layer (F1) in the SEM images in Figure 4.16e) and f), the tribo-oxide formed minimally and appeared to have an island-like structure. Minimal oxidation and subsurface deformation in specimens with many sintering pores prevented crack formation and surface delamination, as visible in Figure 4.15e) and f). It was found that after 1000 sliding cycles, delamination and tribo-oxidation became the dominant mechanisms in controlling the coefficient of friction [164]. Thus, these differences between samples with many and few sintering pores are expected to have a significant impact on the differences in coefficients of friction.

In addition to the differences in the tribo-oxidation zones, there was also a significant difference in **subsurface deformation** (DL) between specimens with many and few sintering pores, as shown in Figure 4.18. It is evident that the subsurface deformation zone was significantly more pronounced in specimens with few sintering pores as illustrated in Figure 4.18a) to d) compared to those with many sintering pores, as seen in Figure 4.18e) and f), which exhibited no significant tribologically caused subsurface deformation. The varying porosity levels at the surface influenced the nominal Hertzian contact pressure. With an overall density of 86 %, according to Buch and Goldschmidt [165], a reduction in effective Young's modulus from 130 to 100 GPa could be calculated [166]. This reduction is further supported by the correlation between decreasing hardness and a lower effective Young's modulus [167]. In line with this, the microhardness measurements in Figure 4.13 show that samples with high porosity exhibited lower surface microhardness values. Moreover, it can be expected that the samples with an additional CIP step exhibited a higher effective Young's modulus compared to those that were only sintered. Since the Poisson's ratio of sintered iron decreases by 0.02 at

a porosity of 22 %, no change in the Poisson's ratio was assumed in the calculation of the maximum Hertzian contact pressure of copper at a porosity of 14 % [165]. Thus, a Poisson's ratio of 0.35 could be expected at room temperature for all the samples [166]. Considering that sapphire, according to Dobrovinskaya et al. [168], has a Young's modulus of 435 GPa and a Poisson's ratio of 0.27, a porosity-related reduction in Hertzian contact pressure of 74 MPa, from 581 to 507 MPa, could be calculated [136]. In addition, with a higher number of surface sintering pores, as visible in Figure 4.15g) and h), the asperities in contact with the counterbody can be assumed to be more widely separated. According to Komvopoulos and Choi [169], a larger spacing between asperities reduces the unloading effect beneath the center of contact, but it also leads to a lower superposition of the subsurface stresses at the contact edges, resulting in regions of high stress being confined closer to the surface. An investigation of the real contact area, comparing a sample with many big pores (MBP) with an overall porosity of 86 % and FBP with 97 %, reveals that the arc length of the wear track profile in Figure 4.20 was approximately 20 µm longer in MBP, measuring 263 µm, compared to FBP. This indicates an 8 % larger real contact area for MBP, suggesting slightly higher maximum surface stresses in FBP due to the smaller contact area. In summary, it can be expected that both the maximum surface stress, influenced by the reduction in the effective Young's modulus and the larger real contact area, and the depth of the stress distribution were less pronounced in the specimens with many sintering pores, contributing to the minimal and shallow subsurface deformation. Moreover, the higher effective Young's modulus of CIP samples implies higher Hertzian contact pressures compared to just-sintered specimens, thereby promoting more pronounced plastic deformation and, consequently, enhanced dislocation pile-up and crack formation. The deformation-induced grain refinement beneath the surface of the specimens with few sintering pores is not attributed to recrystallization phenomena under mild tribological loading conditions [170]. This can be assumed as the temperature increase was likely negligible according to the model by Kuhlmann-Wilsdorf [171], which predicts a maximum increase of only about 0.02 K. The calculation is based on the temperature rise in FSP samples, using a coefficient of friction of 0.7, a contact radius of the harder partner of 0.15 mm, a sliding distance of 6 mm, a microhardness of the softer partner of 670 MPa, as demonstrated in Figure 4.13, a density of the softer partner of 0.97 · 8920 kg m^{-3}, a specific heat capacity of the softer partner of 381 J kg^{-1} K^{-1}, and a volume of

the copper cylinder of $2.827 \cdot 10^{-6}$ m^3 [94]. Thus, the grain refinement can be attributed solely to the self-organization of dislocations, which initially arrange into wall-like structures, serving as the core process for the formation of subgrains and grain refinement [143, 172].

Notable differences in **topographical deformation** between the samples with many and few sintering pores are evident in Figure 4.20. In all wear tracks, plowing could be identified as the predominant wear mechanism. Plowing occurs when one surface is harder than the other, causing the asperities of the harder surface to laterally displace material from the softer surface [60]. A certain amount of force is required to move the softer metal from the front of the slider. The specimen types showed a significant variation in the plowing mechanism: while material in specimens with few sintering pores was pushed aside, forming pile-ups, sintered particles in specimens with many sintering pores were apparently pressed into the sintering pores. This observation is supported by the fact that, in specimens with many sintering pores, there was no significant increase in material transfer to the sapphire spheres during the tribological experiments, as visible in Figure 4.21, nor was any debris found alongside the wear track. Moreover, it can be assumed that the sintered particles were not pulled out, as flattened sintered particles resulting from the preparation process were visible in the cross-sections, as shown in Figure 4.18. The sintered particles were most likely also not partially worn away, since significant subsurface deformation, as visible in the specimens with few sintering pores, would be evident. This is also supported by the fact that fewer grooves in the sliding direction were visible on the surface of the high-porosity samples compared to the low-porosity ones, as visible in Figure 4.15. The low quantity of grooves on the copper surface resulted in fewer corresponding grooves forming on the sapphire counterbody during the experiments, as visible in Figure 4.21. Under humid conditions a layer of adsorbed water forms on the surface of alumina, as described by Perez-Unzueta and Beynon [173]. Gee and Jennett [174] further reported that this water layer promotes the formation of hydroxides such as AlOOH (boehmite), which exhibit a lower hardness than alumina. Boehmite has a Mohs hardness of 3.5, which, according to Angus [175], corresponds to a hardness of 172 to 190 HV (1.7 to 1.9 GPa) [176]. Its hardness is therefore lower than that of Cu_2O, which exhibits a hardness value of 2.94 GPa [69]. The lower hardness of the hydroxide compared to sapphire may contribute to the pronounced wear observed in Figure A.9c) and d). EDS measurements reveal that copper wear particles are deposited on the sphere and the grooves consist of aluminum oxide,

indicating wear of the sphere. Thus, tribological experiments on high-porosity samples resulted in lower abrasive wear in the form of grooves on both the copper and sapphire surfaces compared to low-porosity specimens. Furthermore, as the wear track of MBP is deeper than that of a sample with many small pores (MSP), it can be concluded that sintered particles were more easily pressed into the larger sintering pores. The differences in wear track depths are not only due to the distinct plowing mechanisms but also to the oxidation-related volume increase in specimens with few sintering pores, making the difference appear larger [177]. The more pronounced tribo-oxidation and the accompanying volume increase may also explain why the wear track depth was less pronounced in the CIP specimens compared to the just sintered samples with few sintering pores, as evident in Figure 4.20. Furthermore, as can be seen in Figure 4.13, the surface microhardness of the CIP specimens was higher than that of the only sintered specimens with few sintering pores. According to Equation 7 in Chapter 5.1.1, this resulted in a smaller contact area, which implies that the counterbody did not penetrate as deeply into the specimen, thereby reducing the extent of topographical deformation. The microhardness measurements in Figure 4.13 also revealed that the specimens with large sintering pores exhibited a greater scatter than those with small pores. This increased scatter can be attributed to the strong local influence of large pores, which induced significant variations across different measurement locations and led to greater variability in the measured microhardness values despite identical overall porosity, as visible in Figure A.5. In contrast, specimens with small sintering pores exhibit a more uniform distribution of pore-related influences, resulting in more consistent hardness values and reduced scatter. Moreover, at comparable porosity, specimens with small sintering pores had a higher hardness, resulting in a lower wear track depth and consequently less pronounced topographical deformation than samples with large pores.

Both the initial microstructure and its evolution influence the **coefficient of friction**. Following Lafaye et al. [178], the plowing coefficient of friction μ_P can be determined by means of the plowing friction force F_P and the normal force F_N. These could be determined using the mean contact pressure ρ_a and the projected contact areas in sliding direction A_{SD} and in normal direction A_{ND} [114]. The plowing contribution in case of FSP could be calculated using the coefficient of friction of 0.65 after 1000 cycles and

$\mu_P = F_P / F_N = (\rho_a \cdot A_{SD}) / (\rho_a \cdot A_{ND}) = 0.0028$ Equation 8

based on the determination of A_{SD} = 113 µm^2 and A_{ND} = 39760 µm^2. With a proportion of 0.4 %, the plowing contribution was significantly lower than the shearing contribution in the total friction coefficient of friction. While the plowing contribution of 1.8 % with μ_P = 0.0046 was higher in the case of MSP, based on A_{SD} = 275 µm^2 and A_{ND} = 59396 µm^2, it was still very small compared to the shear component. This is consistent with the theory of Bowden and Tabor, which states that for copper, the plowing term is very small [60]. Following Bowden et al. [179, 180], junctions form in the real contact area between the sphere and the bulk, and according to Equation 3 in Chapter 2.3.1, a total force F_{adh} is required to shear them off. Since the real contact areas of the samples with many and few sintering pores were similar, and the plowing contribution was significantly smaller than the shearing contribution, the main influence on the difference in coefficients of friction should be the force required to break the metallic junctions. However, since copper oxide was in contact with a sapphire sphere, the formed junctions were of ionic and covalent nature rather than metallic [181]. Accordingly, the present system behaved differently than in the Bowden and Tabor model and was not based solely on mechanisms related to plasticity.

Beyond the macroscopic mechanical and oxidation behavior, the electronic state at the interface may also play a role. Specimens with many and few sintering pores, having the same sliding speed v during the tribological experiments, exhibited differences in nominal friction power density

$q_N = \mu \cdot p_N \cdot v$ Equation 9

because their nominal contact areas varied, resulting in changes in nominal pressure p_N, and because their coefficients of friction μ differed, as shown in Figure 4.14 [182]. Since the determination of the nominal contact area considers only the macroscopic geometry, it does not account for porosity [183]. As the wear track depth and width are larger in the high-porosity samples, a larger nominal contact area and consequently a lower nominal pressure can be assumed. The specimens with many sintering pores exhibited a lower friction power density during the tribological experiments, which is evident from the lower nominal contact pressure, the lower coefficients of friction in Figure 4.14. As a result, the amount of energy

dissipated at the interface was greatly reduced, providing insufficient driving force for pronounced subsurface deformation, crack formation, or significant tribo-oxidation [184]. In contrast, pronounced plastic deformation was observed beneath the surface in the specimens with few sintering pores, and since the electron work function decreases with the onset of plastic deformation, different electron work functions could be expected between the specimens with few and many sintering pores [185]. According to Li [186], adhesion in the metal-ceramic contact increases with decreasing electron work function. Consequently, a reduced electron work function in the specimens with few sintering pores, linked to a higher degree of plastic deformation, could lead to an increase in adhesion, which according to Bowden and Tabor is the primary component of the coefficient of friction. The influence of the electron state on the coefficient of friction has already been observed in other materials. Pauling [187] found that transition metals are characterized by varying degree of d-orbital bonding. As the d-bond character increases, the distance between metal atoms decreases. The occupation of the d-electron band correlates with the chemical activity of the element's surface, where lower occupancy indicates a more chemically active surface [188]. Buckley and Miyoshi [188–190] correlated tribological properties of pure metals with their d-orbital bonding, finding that metals with low d-orbital bonding such as titanium and zirconium exhibit higher chemical interaction and thus higher friction against ceramics and in self-pairing. Thus, the different electron work functions in copper and its oxides for specimens with many and few sintering pores could also significantly influence the tribological properties.

In summary, pressing the sintered powder particles into the sintering pores, together with the reduced Hertzian pressure and the enlarged contact area, prevented significant subsurface deformation, resulting in minimal tribo-oxidation and consequently in the absence of pore agglomeration beneath the surface that could lead to delamination. This lack of energy dissipation effects likely explains why the coefficient of friction did not increase significantly within the first 100 to 200 cycles, as was the case with specimens containing few sintering pores, as visible in Figure 4.14. Regarding the topographical deformation, the specimens with high porosity exhibited wear tracks that are 0.9 to 2.0 µm deeper and 100 to 200 µm wider than those of low-porosity samples, as shown in Figure 4.20. However, increased material loss is not expected, as it is assumed that sintered particles were pressed into the subsurface

sintering pores during tribological loading. Regarding the pore size, larger sintering pores caused deeper wear tracks as well as higher surface stresses in low-porosity specimens and lower Hall-Petch strengthening in high-porosity ones, thereby promoting greater grain refinement at the surface and tribo-oxidation by creating more oxygen diffusion paths. Consequently, sintering pores, especially small pores, are beneficial for the unlubricated tribological behavior.

Since the vibropolished specimens with many sintering pores showed minimal subsurface deformation after 1000 cycles, the tribo-oxidation layer was only slightly developed, and no cracks or delamination were observed. This raised the questions: Could a significant increase in the number of cycles lead to the formation of a thick tribo-oxidation layer in vibropolished specimens with many sintering pores, despite low subsurface deformation? If so, could this tribo-oxidation layer be sufficiently thick that pronounced pores in the tribo-oxide, cracks, and delamination appear, and thus an increase in the coefficient of friction similar to that observed in samples with a low porosity?

5.2.2 Effect of Testing Duration

An increase in the number of cycles from 1000 to 5000 resulted in neither a change in the coefficients of friction nor a deepening or widening of the wear tracks of the vibropolished FSP, MSP and MBP, as shown in the mean surface profiles of the wear tracks in Figure 5.8 and their light microscopic images in Figure A.13 in the Appendix. During the tribological loading, the decrease in topographical deformation was likely due to an increase in contact area that reduced the maximum surface stress to a level at which no further topographical deformation occurred. Another reason for the wear track depth approaching an equilibrium state, could be the hardening of the material due to, among other factors, Hall-Petch strengthening and work hardening. With increasing number of cycles, oxygen could continue to diffuse into the material along the continuously forming dislocation and grain boundary pathways, leading to the progression of tribo-oxidation, without a further increase in the wear track depth. This can be confirmed by a comparison of the subsurface deformation and tribo-oxidation layers of FSP, MSP and MBP after 5000 cycles in Figure 4.23 with the microstructures after 1000 cycles in Figure 4.16 and in Figure 4.18. It could be observed that there was no change in the subsurface deformation depth, while the tribo-oxidation depth

increased. After 5000 cycles, the depth of the tribo-oxidation zones in high-porosity samples remained less pronounced than in low-porosity specimens after 1000 cycles, as evident in Figure 4.16 and Figure 4.23. In addition, the tribo-oxide in the high-porosity samples appeared more dispersed and non-continuous. Since neither cracking in the tribo-oxide nor delamination at the surface occurred in either the MSP or MBP samples, the density of the tribo-oxide likely played a significant role in the formation of these energy dissipating phenomena. Figure 4.23 further illustrates that the increasing tribologically induced oxidation of the FSP led to the formation of cracks in the tribo-oxide and delamination at the surface after 5000 cycles. This delamination is also visible in the SE images of the wear tracks in Figure A.14 in the Appendix. These phenomena were not observed after 1000 cycles, as shown in Figure 4.16 and in Figure 4.15. FBP, on the other hand, already exhibited cracks and delamination at the surface after 1000 cycles, due to the increased surface stress caused by the larger sintering pores. In all likelihood, the higher surface stress led to a higher tribologically-induced dislocation density and amount of grain boundaries, consequently creating more diffusion channels for oxygen. After 5000 cycles, the depth of the tribo-oxide layer of FSP was similar to that of FBP after 1000 cycles.

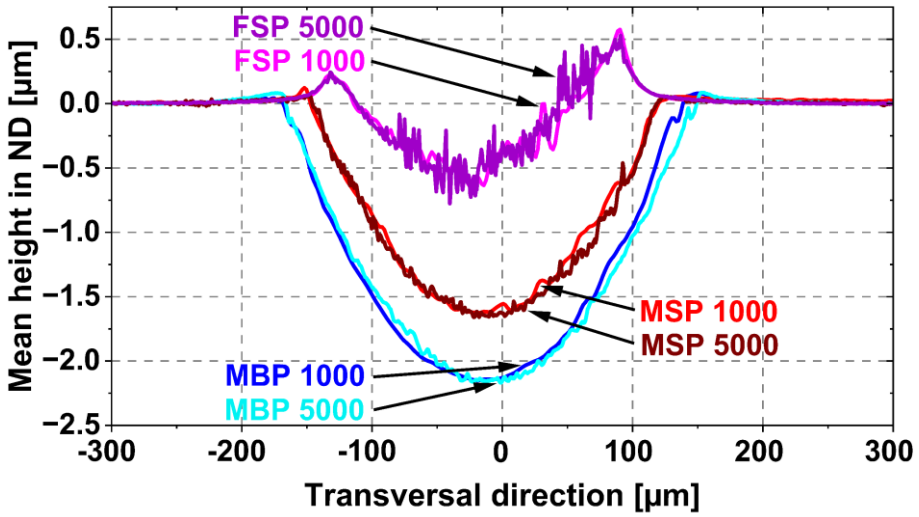

Figure 5.8: Comparison of the wear track profiles of specimens with few small pores (FSP), many small pores (MSP) and many big pores (MBP) based on white light interferometric images after 1000 and 5000 cycles [135].

In summary, after 5000 cycles, no significant changes were observed in the vibropolished MSP and MBP specimens, either on or beneath the surface, aside from the progression of tribo-oxidation. Due to the wear track depth approaching an equilibrium state, the subsurface

sintering pores are most likely never completely filled, and even after 5000 cycles, sintering pores could still be detected beneath the surface. However, an increase in cycles led to cracks in the tribo-oxide and delamination at the surface in the vibropolished FSP sample, which shows that, with increasing tribo-oxidation, these phenomena eventually emerge. For specimens with many sintering pores, a significant increase in cycles would likely be necessary for this to occur. Having found that a lasting reduction of friction can be achieved through high porosity, the remaining question is: To what extent does surface porosity influence this behavior?

5.2.3 Role of Surface Porosity

In order to analyze the impact of surface porosity on the tribological performance, the influence of surface preparation was first investigated by comparing the effect of chemical-mechanical vibropolishing and electropolishing on the MSP specimens. By vibropolishing, the preparation-induced Beilby layer and scratches could be reduced [191]. Additionally, after being smeared during preparation, as seen in Figure A.15a) in the Appendix, the sintering pores between the sintered particles were exposed during vibropolishing, as shown in Figure 4.24a) and c). Under the assumption, according to Steigerwald et al. [50], that clusters of atoms are first removed from the surface and subsequently chemically dissolved, the remaining scratches after vibropolishing, visible in Figure 4.24c), can either be attributed to insufficient chemical reaction, causing the clusters to scratch the sample surface, or to dislodged particles that may have been trapped in the sintering pores. The latter is confirmed by small particles exposed in the sintering pores after vibropolishing, as shown in Figure A.15b). Electropolishing of the MSP specimen not only resulted in the removal of the Beilby layer and scratches, as well as the exposure of the sintering pores but also caused a lateral enlargement of the sintering pores, visible in Figure 4.24b) and d), due to a higher current density at the pore edges than in the pore interior [192]. As noted by Yang et al. [40], the current density is highest at sharp edges, which explains the observed rounding of the sintering pore contours during electropolishing. This led to a significant increase in roughness compared to the vibropolished surface. Since similar overall porosities were measured for the two MSP specimens, which were subsequently either vibropolished or electropolished, the porosity affected the effective Young’s modulus of both specimens to the same extent.

According to Buch and Goldschmidt [165], a porosity of 15 % is expected to result in an effective Young's modulus of 98 GPa. Figure 4.25 shows that the average microhardness of the vibropolished MSP specimen was higher than that of the electropolished one. According to Fellah et al. [193], the effective Young's modulus increases with hardness. Campbell et al. [194] detected local variations in the effective Young's modulus through nanoindentation; however, no change in the average effective Young's modulus could be experimentally determined due to surface roughness. Accordingly, Figure 4.25 reveals a greater scatter of hardness measurement values in the electropolished MSP sample compared to the vibropolished one, indicating local differences in the effective Young's modulus. Therefore, it is plausible to assume that the overall average effective Young's modulus of the electropolished and vibropolished specimens were the same. Considering porosity and surface roughness in the calculation of the maximum Hertzian contact pressure, a value of 501 MPa could be expected in both specimens during the tribological tests [136]. However, due to the enlarged sintering pores on the surface of the electropolished specimen, as shown in Figure 4.24, the contact area between copper and the sapphire sphere was smaller at the beginning of the tribological test than for the vibropolished specimen. Consequently, the applied load from the sphere was distributed over a smaller contact area in the electropolished specimen, so that a higher maximum contact pressure was expected compared to the vibropolished one, since surface roughness, just like the predominant plastic deformation, is not considered in the calculation of the maximum Hertzian contact pressure. This surface-induced stress increase caused more pronounced plastic **subsurface deformation**, compared to the shallower layer seen in the vibropolished MSP specimen, as shown by the deformation layer (DL) in Figure 5.9. Furthermore, the grooves in the sliding direction, which are more pronounced in the electropolished sample and typical for abrasive wear, indicate a more extensive subsurface deformation [63]. These features can be observed in the SE wear track images of the electropolished MSP sample in Figure 4.28a) and b), whereas they are barely visible in the SE images of the vibropolished MSP specimen in Figure 4.15e). The grooves were most probably formed by asperities of the harder sapphire sphere, which penetrated and plowed the softer copper specimen. Another indication, particularly evident in the BSE images in Figure 4.28c) and d), is that in the center of the wear track, where, according to the Hertzian contact pressure distribution, the stress is highest during the tribological tests, the sintering pores of the

electropolished MSP sample have been either smeared or removed [195]. In contrast, after the tribological loading, the sintering pores in the vibropolished MSP specimen remained almost unchanged at the surface, as seen in Figure 4.15g) and h), which supports the fact that no significant subsurface deformation was observed. Through the reduction of sintering pores in the contact area of the electropolished specimens and the enhanced depth and width in the mean height profile of the wear track, as shown in Figure 4.31, the contact area between the specimen and the sapphire sphere increased. While this contributed to a reduction in the maximum stress, as the force from the sphere was distributed over a larger real contact area, the overall shear force increased since, according to Bowden and Tabor [180], a higher amount of junctions were formed and sheared in the larger real contact area of the specimen and the sphere, resulting in an increase in the coefficient of friction [138].

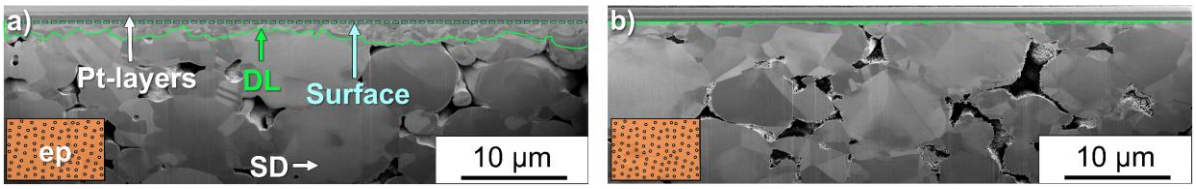

Figure 5.9: SE cross-section images in sliding direction (SD) at the center of the wear track for a) electropolished (ep) MSP and b) vibropolished MSP specimen, in which the subsurface deformation layers (DL) are marked in green, directly beneath the protective Pt-layers (adapted from [122, 135]).

Upon examining the **topographical deformation** by analyzing the mean height of the wear track profiles in Figure 4.31, it is evident that the surface of the electropolished MSP sample was significantly rougher than that of the vibropolished MSP specimen, due to the previously described enlarged sintering pores, delamination and grooves in the sliding direction. Additionally, both the electropolished and vibropolished MSP specimens did not show pile-ups on the sides of the wear tracks, unlike the vibropolished FSP sample. While in the vibropolished MSP specimen, particles were pressed down into the subsurface sintering pores, in the electropolished MSP sample, material was removed and plowed into the enlarged surface sintering pores, especially in the center of the wear tracks. Plowing takes place when one surface is significantly harder than the other, leading the asperities of the harder surface to laterally displace the softer material [60]. Similar to the electropolished MSP sample, in the vibropolished FSP specimen, material was pushed onto the sides of the wear track. However, due to the lack of sufficient sintering pores to fill, pile-ups formed along the edges of the wear

track. Figure 4.31 also shows that, depending on the location on the sample where the tribological tests were conducted, the wear tracks exhibited varying widths and depths. This is attributed to the position of the sintering pores on and below the surface as well as the sintering pore density. Therefore, a sample-dependent variance in the wear track depth and width within the same specimen is generally expected. Consequently, the different depths and widths of the wear tracks, from the tribological experiments conducted immediately after electropolishing and 24 h later, cannot be attributed to the aging time, including the presence of a native oxide layer after 24 h in air, which is reported by Platzman et al. [121] to be between 2.5 and 4.0 nm thick, and by León et al. [196] to be around 2 nm thick. However, it was generally observed that the width and depth of the wear tracks are greater in the vibropolished MBP specimen, as particles were more easily pressed into the larger sintering pores [122]. While the average depth of the wear tracks in the electropolished MSP specimen lied between that of the vibropolished MSP and MBP samples, their width was almost identical to that of the MBP sample. This could be due to the fact that the sintering pores were significantly enlarged during electropolishing compared to those in the vibropolished MSP sample, thus behaving more similarly to the MBP specimen.

In addition to the deformation, the dark grey zone (F1) immediately beneath the surface, visible in Figure 4.29b) and d), is of significance, representing the **tribo-oxidation** zone according to Rau et al. [90]. Due to the deformation-induced grain refinement (DL) shown in Figure 4.29a) and c), the tribological loading led to the formation of numerous new dislocations and grain boundaries through the rearrangement of dislocations during dynamic recovery, both serving as diffusion paths for oxygen [90, 197, 198]. Since the vibropolished MSP specimen exhibited only a very small tribologically induced subsurface deformation layer (DL), the tribo-oxidation zone (F1) was correspondingly less pronounced, reaching a depth of up to 0.1 µm, compared to the electropolished specimen, where the tribo-oxidation zone reached maximum depths of 1.6 and 0.8 µm.

During the tribological tests Kirkendall pores most likely formed between the tribo-oxide and copper because copper ions diffuse faster than oxide ions [90, 95]. With progressing oxidation, Rau et al. [90] observed the formation of pores along the diffusion paths, which led to cracks beneath the surface and eventually to surface delamination. This mechanism could also be responsible for the behavior observed in the electropolished MSP specimen. Other factors

contributing to delamination could include the higher hardness of copper oxide, which leads to a greater tendency for crack formation compared to copper, as well as dislocation pile-up at the copper–oxide interface, promoting the formation of voids and cracks [66, 69, 91]. Since the tribo-oxidation zone (F1) was significantly more pronounced in the electropolished MSP specimen compared to the vibropolished MSP sample, cracks (F2) within the tribo-oxide and delamination at the surface were observed in the wear tracks of the electropolished specimen, as visible in Figure 4.29b) and d). Both the depth of subsurface deformation (DL) and the development of the tribo-oxidation zone (F1), along with cracks (F2) beneath the surface, were similar in the electropolished MSP and the vibropolished FSP specimens, as evident in Figure 4.16 and Figure 4.18.

The spots, visible in Figure 4.26, are likely due to **the effects of the electrolyte**. According to Jurin's law, the capillary force is inversely proportional to the diameter of the capillary tube [199]. Therefore, a high capillary force is expected in very small craters, as observed in Figure 4.26c). Neither rinsing with water nor the ultrasonic cleaning with isopropanol could probably flush out the electrolyte from the small cavities. After drying the surface, a subsequent pressure difference between the outside and the inside of the small craters could cause the liquid to rise within the small craters and eventually emerge at the surface over time. This phenomenon of rising liquid was observed a few minutes after drying the MSP specimen, which had been previously cleaned with isopropanol. The electrolyte consisted of ethanol, propan-1-ol, and phosphoric acid. As ethanol and propan-1-ol could evaporate at the surface, the concentration of phosphoric acid increased, leading to supersaturation, which most probably resulted in crystallization around the craters, forming round spots visible in Figure 4.26 [200, 201]. Furthermore, in combination with water, phosphoric acid can form crystalline hemihydrates at room temperature [201–203]. In addition to crystallization due to supersaturation, crystallization could also occur due to reactions with water, with which the specimen was rinsed to stop the reaction after electropolishing, or with humid air during the tribological tests. During the experiment after a 24 h exposure in air, the proportion of crystallization spots was likely significantly higher than in the first experiment, directly after electropolishing, where crystallization likely occurred mainly during the tribological test. Additionally, as shown in Figure 4.26a) and b), the number of these spots varied across the surface. Even if the sapphire sphere was probably not only in contact with copper or its oxides

in these areas, but also with crystallized phosphoric acid, among other substances, this likely had no significant influence on the tribological behavior.

The differences in the evolution of the **coefficients of friction** between the experiment conducted immediately after electropolishing and the one performed 24 h later, as shown in Figure 4.27, were likely not caused by the native oxide layer present in the latter. It has already been shown that even with the same exposure time to air before the tribological experiment and under identical experimental conditions, different running-in behaviors of the coefficients of friction could be observed, with the steady-state coefficients of friction sometimes only being reached after 500 cycles [204, 205]. It was also demonstrated that different exposure times to air, up to 56 h, have no influence on the steady-state coefficient of friction [205]. Whether the crystallization of phosphoric acid on the surface has an impact on the coefficient of friction would need to be investigated; however, it seems to have no influence. The progression of the coefficient of friction over 1000 cycles for the different specimens indicates that due to the electropolishing of the MSP sample and the associated phenomena, the coefficient of friction increased by a factor of 2 to 3 compared to the vibropolished MSP specimen.

Upon examining these findings, it can be concluded that a pronounced subsurface deformation, which was observed in both the vibropolished specimens with few sintering pores and the electropolished MSP sample, could accelerate tribo-oxidation and thus the formation of pores, cracks, and delamination at the surface. These energy dissipation mechanisms were associated with an increased coefficient of friction.

With these results, the second research question can be addressed: Do pore size and overall porosity affect the tribological behavior, and to what extent does surface porosity influence this behavior? It was found that in contrast to pore size, porosity had a significant influence on the coefficient of friction. A pronounced subsurface deformation, which was observed in both the specimens with few sintering pores and the electropolished MSP, could accelerate tribo-oxidation and thus the formation of pores, cracks, and delamination at the surface, features that are known to contribute to an increased coefficient of friction. Consequently, specimens with a high porosity exhibited a coefficient of friction of 0.3 after 1000 cycles,

which was less than half that of specimens with low porosity. In terms of wear behavior, high-porosity samples showed deeper and wider wear tracks than those of low-porosity ones. However, higher material loss is unlikely, as particles are assumed to be pressed into subsurface sintering pores during sliding. Since this differing behavior between specimens with many and few sintering pores could be attributed to a varying degree of subsurface deformation, it was then tested whether, even with minimal subsurface deformation in vibropolished high-porosity samples, the tribo-oxidation could progress with an increase in the cycle number from 1000 to 5000, to the extent that the tribological behavior would resemble that of vibropolished low-porosity specimens. After 5000 cycles, no changes were observed in the vibropolished MSP and MBP specimens, either on or beneath the surface, aside from the progression of tribo-oxidation. However, an increase in cycles led to cracks in the tribo-oxide and delamination at the surface of the vibropolished FSP sample, which shows that, with increasing tribo-oxidation, these phenomena eventually emerge. For specimens with many sintering pores, a significant increase in cycles would likely be necessary for this to occur.

Concerning the question of how surface porosity influences tribological performance, it was found that electropolishing the surface before tribological testing destroyed the friction-reducing effect of the sintering pores. Electropolishing induced a pronounced enlargement of the sintering pores, which altered the surface topography significantly. This change resulted in higher stresses at the surface during the tribological experiments than those in the vibropolished samples. This caused greater plastic subsurface deformation, which in turn led to an expanded tribo-oxidation zone, in which cracks formed, resulting in delamination at the surface. Consequently, the electropolished specimen showed a tribological behavior and trend in coefficient of friction similar to those of vibropolished specimens with few sintering pores. In summary, vibropolished surfaces of MSP specimens are the most beneficial of all tested porous specimen types for unlubricated tribological performance under mild tribological loading conditions.

After separately analyzing the gradient nano-grained and porous microstructures, a comparison with coarse-grained microstructures is necessary to identify which one influenced tribological behavior more strongly.

5.3 Comparative Analysis of Varying Sample Types

The insights gained enable a comparative analysis of the tribological behavior of the different sample types, as presented in Table 5.4. The GNG2-10 sample was selected as the representative of the gradient nano-grained (GNG) specimens, and the sample with many small pores (MSP) as the representative of the porous specimens, since both demonstrated the greatest reduction in the coefficient of friction under mild tribological loading conditions compared to the other samples of their respective types. Notably, porosity could reduce the coefficient of friction by about half compared to the coarse-grained (CG) and GNG samples.

Table 5.4: Overview of the tribological behavior of coarse-grained (CG), gradient nano-grained (GNG), and porous copper samples. The tribological tests on CG specimens were conducted with a stroke of 12 mm under a normal load of 1.5 N and otherwise identical conditions as those used in this study, which are considered mild tribological loading conditions. Unless otherwise noted, the results for CG were taken from Rau et al. [70].

	CG	**GNG**	**Porous**
Coefficient of friction (1000^{th} cycle)	0.55	0.53	0.26
Topographical deformation	Height: -1.3 µm Wear track width: 553 µm	Height: +0.6 µm Wear track width: 175 µm	Height: -1.6 µm Wear track width: 275 µm
Subsurface deformation	Depth: 17 µm	Depth: 4.4 µm	Depth: 0.5 µm
Wear mechanisms:			
- **Plowing**	✓	✓	✓
- **Microplowing**	✓	✓	✓
- **Tribo-oxidation**	Depth: 0.3 µm [94]	Depth: 1.8 µm	Depth: 0.1 µm
- **Cracking**	✗	✓	✗
- **Delamination**	✗	✓	✗

Regarding the wear track characteristics, the measured wear track width was influenced by the presence of pile-ups. When neglecting these pile-ups, the wear track of the CG sample was approximately 200 µm wide. The porous sample exhibited a greater wear track depth and width due to its lower surface microhardness of 0.5 GPa compared to the GNG specimen. Conversely, the GNG sample, with a microhardness of 3.0 GPa, showed an increased surface height attributed to delamination and volume expansion from tribo-oxide formation, in comparison to both the CG and porous samples [99].

Plowing was identified as a wear mechanism across all sample types. In the CG specimen, this resulted in clearly visible pile-ups at the edges of the wear tracks, reaching heights of approximately 0.75 µm [99]. In contrast, the smaller pile-ups in the GNG sample were difficult to differentiate from delamination. The porous sample, however, showed no formation of pile-ups, likely as it is assumed that the particles were pressed into the subsurface sintering pores, preventing material pile-ups at the edges. Furthermore, all surfaces exhibited grooves to varying extents, which can be attributed to microplowing by harder asperities of the counterbody.

Subsurface deformation was comparable between CG and GNG samples, although in the case of GNG, it largely depended on the size of the surface grains. In porous samples, however, subsurface deformation was about an order of magnitude smaller than in the other two specimen types.

The tribo-oxidation depth was significantly greater in GNG than in the other two sample types, which also explains the occurrence of subsurface cracking and surface delamination associated with a thick tribo-oxide layer [94]. Due to the stroke in the CG sample being twice as long as in the GNG and the porous samples, the longer test duration likely led to a further progression of tribo-oxidation. In CG samples subsurface cracking and surface delamination did not occur during 1000 sliding cycles but could be detected after 5000 cycles with increasing tribo-oxide thickness [94]. However, the porous sample showed neither cracking nor delamination after 1000 or 5000 cycles as the tribo-oxidation was very limited.

In summary, porous samples led to a significant reduction in the coefficient of friction and exhibited minimal subsurface deformation and tribo-oxidation but showed greater

topographical deformation compared to CG and GNG samples, yet without displaying any increase in overall wear. In contrast, GNG samples did not achieve a significant reduction in the coefficient of friction relative to CG but resulted in reduced topographical deformation. However, the GNG sample underwent substantially more pronounced tribo-oxidation, which was associated with the occurrence of cracking and delamination.

Overall, the results demonstrate that vibropolished high-porosity copper samples with small pores exhibit the most advantageous performance under mild tribological loading conditions. Compared to electropolished porous, CG and GNG specimens, as well as vibropolished samples with few pores and many big pores, vibropolished specimens with many small pores not only exhibit the lowest coefficient of friction but also show the least subsurface deformation and tribo-oxidation. Although porosity leads to greater topographical deformation, it stabilizes at a certain depth over the sliding cycles, and no porosity-related increase in wear occurs. The topographical deformation in high-porosity samples can be reduced by decreasing the pore size. Thus, vibropolished high-porosity specimens with small sintering pores exhibit superior tribological performance compared to those with big sintering pores, and, apart from topographical deformation, they also outperform low-porosity, CG, and GNG specimens.

6 Summary & Outlook

This study investigated the hypothesis that gradient nano-grained (GNG) microstructures influence the tribological behavior of copper more significantly and reduce the coefficient of friction more effectively than porosity under mild tribological loading conditions. To evaluate this, the tribological behavior of GNG microstructures with different layer depths and surface grain sizes, as well as porous samples with varying pore sizes and porosities were first analyzed and then compared with each other. The investigation also considered the impact of sliding duration and surface finishing methods, specifically chemical-mechanical vibropolishing and electropolishing, on the tribological behavior of porous samples.

Previous research has demonstrated that GNG structures significantly reduce friction under severe tribological conditions (high loads, high sliding speeds) and short strokes. However, this study revealed that under mild tribological conditions and longer strokes GNG structures exhibited high coefficients of friction regardless of GNG layer thickness or surface grain size. Sliding speed and test duration predominantly governed the tribological performance rather than the initial GNG microstructure. Extended test duration and lower sliding speeds promoted pronounced tribo-oxidation and enhanced plastic deformation at the surface, leading to grain coarsening, surface roughening, subsurface cracking and delamination, and a transition to higher friction. The low normal force most likely had no significant effect on the increase in the coefficient of friction. If the load was sufficiently low for the stress distribution to be confined to the uppermost NG layer, tribo-oxidation occurring at low sliding speeds likely prevented the formation of an ultrafine-grained surface layer, which could reduce friction in tests conducted in dry nitrogen at low speeds. Although the depth of the tribologically induced subsurface deformation was influenced by the surface grain size, the overall wear behavior remained similar under identical tribological testing conditions.

A high porosity in copper components, on the other hand, reduced the coefficient of friction by over 50 % compared to low-porosity samples and GNG microstructures. Low-porosity specimens showed pronounced subsurface deformation characterized by grain refinement, thicker tribo-oxide layers, and subsurface cracks. This crack formation is attributed to the higher hardness of the oxide, Kirkendall pore accumulation, and dislocation pile-ups at the

copper-oxide interface, leading to surface delamination. Additional cold isostatic pressing further increased dislocation density, promoting dislocation pile-up and crack formation. In contrast, high-porosity specimens exhibited limited subsurface deformation resulting in minimal tribo-oxidation due to reduced Hertzian contact pressure, a slightly larger real contact area, and a reduced depth of the high-stress regions within the material. Moreover, topographical deformation differed: In low-porosity specimens, material pile-ups and pronounced grooves were formed, while high-porosity ones showed sintering particles embedded within sintering pores, along with minimal grooving, material transfer, and wear debris. Variations in wear track depths were attributed to distinct plowing mechanisms and greater oxidation-related volume expansion in low-porosity specimens. Finally, the increased plastic subsurface deformation observed in low-porosity samples likely correlated with a reduction in electron work function, which may enhance adhesion and thereby increase friction. Concerning pore size, larger sintering pores promoted greater grain refinement and tribo-oxidation due to higher surface stresses in low-porosity samples and reduced Hall-Petch strengthening in high-porosity specimens, resulting in additional diffusion paths for oxygen. Furthermore, the lower hardness of specimens with large sintering pores led to deeper wear tracks. In samples with many big sintering pores, this indicates that particle embedding occurred more easily within the larger pores.

The long-term behavior of high-porosity specimens showed no significant changes apart from a slight increase in tribo-oxidation depth. In contrast, samples with few small sintering pores showed cracks in the tribo-oxide and surface delamination, revealing damage from advancing tribo-oxidation. Similar effects in high-porosity specimens likely require many more cycles.

Different surface treatments of high-porosity samples revealed that electropolishing enlarged sintering pores, yielding a nearly 15-fold higher surface roughness than vibropolishing. This reduced the contact area, raised local stresses, and caused stronger plastic deformation at and beneath the surface, evident from deeper wear tracks, more grooves along the sliding direction, smeared or removed sintering pores, and enhanced subsurface grain refinement. The electropolished sample also exhibited stronger tribo-oxidation, attributed to numerous new oxygen diffusion paths via dislocations and grain boundaries. Unlike the vibropolished one, cracks formed from pores within the tribo-oxide layer, leading to surface delamination. The plowing mechanism also differed: In the vibropolished specimen, sintered particles were

pressed into subsurface sintering pores, whereas in the electropolished one, material was smeared into surface sintering pores. The electropolished high-porosity sample behaved similarly to vibropolished low-porosity ones, indicating that deformation, tribo-oxidation, cracking, and delamination are linked to high friction.

Based on these findings, the initial hypothesis can be disproved. Porous samples significantly reduce the coefficient of friction and show minimal subsurface deformation and tribo-oxidation, but greater topographical deformation due to deeper wear tracks than coarse-grained (CG) and GNG samples. GNG specimens do not reduce friction compared to CG; although they exhibit less topographical deformation, they show increased tribo-oxidation linked to cracking and delamination, a behavior also observed in CG copper at longer test durations. Thus, porosity not only influences the tribological behavior of copper more significantly under mild loading conditions but can also reduce the coefficient of friction by more than half.

The insight into the long-term stable low friction of vibropolished porous copper surfaces highlights their potential for aerospace, automotive, and railway components. Porous copper may become relevant in lightweight, high-conductivity, and tribologically reliable applications by lowering energy use, fuel consumption, and emissions. This study further emphasizes the importance of surface treatments tailored to the manufacturing process. As the influence of porosity on tribological behavior is likely not unique to copper, these findings may also apply to other metals. The results are particularly relevant for manufacturing processes where residual porosity is unavoidable and usually considered a drawback. In additive manufacturing, such as laser powder bed fusion, porosity and the ability to deliberately control it via process parameters can instead turn into advantages for tribological performance.

Future research could examine pore gradients, different pore types (e.g., keyhole or lack-of-fusion pores), various pore shapes, and their potential anisotropic effects on friction in copper. The tribological behavior of porous copper should also be studied under different environmental conditions, for example by comparing vibropolished and electropolished surfaces under lubrication. Moreover, the present findings are limited to mild tribological

loading conditions and an inert counter-body. Therefore, future work should investigate the effect of porosity in metal–metal contacts as well as under severe tribological loading conditions, including higher loads and sliding speeds in combination with shorter test durations, under which GNG samples exhibit a low coefficient of friction. A direct comparison between GNG and porous copper samples, as well as an investigation into the effect of pore size on friction and wear under these severe testing conditions, would be highly interesting. Additionally, the behavior of GNG structures under mild tribological loading conditions requires further study to identify the test conditions at which the transition from low to high friction occurs. To this end, the same sample should be tested under both severe and mild tribological conditions to avoid microstructural variations between experiments. It also remains to be explored whether mild tribological conditions in nitrogen, in contrast to air, allow the formation of an ultrafine-grained surface layer in GNG samples and whether such a layer would reduce friction.

7 Literature

[1] H. Czichos, K.-H. Habig, Tribologie-Handbuch: Tribometrie, Tribomaterialien, Tribotechnik, third ed., Springer-Verlag, Wiesbaden, 2015.

[2] P. Stoyanov, R. R. Chromik, Scaling Effects on Materials Tribology: From Macro to Micro Scale, Materials 10 (2017), 550. DOI: 10.3390/ma10050550.

[3] B. Bhushan, Principles and Applications of Tribology, second ed., John Wiley & Sons, Ohio, 2013.

[4] H. Czichos, Tribology: A Systems Approach to the Science and Technology of Friction, Lubrication, and Wear, Elsevier, Amsterdam, 1978.

[5] K. Holmberg, A. Erdemir, Influence of tribology on global energy consumption, costs and emissions, Friction 5 (2017), 263–284. DOI: 10.1007/s40544-017-0183-5.

[6] M. Woydt, The importance of tribology for reducing CO_2 emissions and for sustainability, Wear 474–475 (2021), 203768. DOI: 10.1016/j.wear.2021.203768.

[7] M. Woydt, T. Gradt, T. Hosenfeldt, R. Luther, A. Rienäcker, F. J. Wetzel, C. Wincierz, Tribologie in Deutschland-Querschnittstechnologie zur Minderung von CO2-Emissionen und zur Ressourcenschonung, expert study by Gesellschaft für Tribologie eV, 2019. https://www.gft-ev.de/wp-content/uploads/GfT-Studie-Tribologie-in-Deutschland.pdf (accessed 2025-08-18).

[8] M. L. Rahaman, E. Bernal, M. Spiryagin, C. Cole, R. Buckley, Q. Wu, A review on frictional torque reduction approaches for energy efficient roller bearings, Advances in Mechanical Engineering 17 (2025), 1–22. DOI: 10.1177/16878132251340233.

[9] C. Vincent, J. F. Silvain, J. M. Heintz, N. Chandra, Effect of porosity on the thermal conductivity of copper processed by powder metallurgy, Journal of Physics and Chemistry of Solids 73 (2012), 499–504. DOI: 10.1016/j.jpcs.2011.11.033.

[10] G. Singh, S. Singh, J. Singh, P. M. Pandey, Parameters effect on electrical conductivity of copper fabricated by rapid manufacturing, Materials and Manufacturing Processes 35 (2020), 1769–1780. DOI: 10.1080/10426914.2020.1784937.

[11] C. Greiner, Z. Liu, L. Strassberger, P. Gumbsch, Sequence of Stages in the Microstructure Evolution in Copper under Mild Reciprocating Tribological Loading, ACS Applied Materials & Interfaces 8 (2016), 15809–15819. DOI: 10.1021/acsami.6b04035.

[12] X. Chen, Z. Han, K. Lu, Friction and Wear Reduction in Copper with a Gradient Nano-grained Surface Layer, ACS Applied Materials & Interfaces 10 (2018), 13829–13838. DOI: 10.1021/acsami.8b01205.

[13] X. Chen, Z. Han, A low-to-high friction transition in gradient nano-grained Cu and Cu-Ag alloys, Friction 9 (2021), 1558–1567. DOI: 10.1007/s40544-020-0440-x.

[14] W. L. Li, N. R. Tao, Z. Han, K. Lu, Comparisons of dry sliding tribological behaviors between coarse-grained and nanocrystalline copper, Wear 274–275 (2012), 306–312. DOI: 10.1016/j.wear.2011.09.010.

[15] B. Wu, Microstructure characterization and mechanical properties of gradient nanostructured copper generated by ultra-precision machining, Ph.D. Thesis, The Hong Kong Polytechnic University, Hong Kong, 2022.

[16] H. Z. Hassan, N. M. Saeed, Advancements and applications of lightweight structures: a comprehensive review, Discover Civil Engineering 1 (2024), 47. DOI: 10.1007/s44290-024-00049-z.
[17] J.-J. Chen, H. Xie, L.-Z. Liu, H. Guan, Z. You, L. Zou, L. Zou, H.-J. Jin, Strengthening gold with dispersed nanovoids, Science 385 (2024), 629-633. DOI: 10.1126/science.abo7579.
[18] A. Candela, G. Sandrini, M. Gadola, D. Chindamo, P. Magri, Lightweighting in the automotive industry as a measure for energy efficiency: Review of the main materials and methods, Heliyon 10.8 (2024). DOI: 10.1016/j.heliyon.2024.e29728.
[19] Y. Liu, Y. Li, L. Miao, Impact of lightweight materials substitution on material stock and carbon emission of private vehicles in China, Environment, Development and Sustainability (2024), 1-24. DOI: 10.1007/s10668-024-04762-8.
[20] F. Imani, A. Gaikwad, M. Montazeri, P. Rao, H. Yang, E. Reutzel, Process Mapping and In-Process Monitoring of Porosity in Laser Powder Bed Fusion Using Layerwise Optical Imaging, Journal of Manufacturing Science and Engineering 140 (2018), 101009. DOI: 10.1115/1.4040615.
[21] W. Wang, J. Ning, S. Y. Liang, Analytical prediction of keyhole porosity in laser powder bed fusion, The International Journal of Advanced Manufacturing Technology 119 (2022), 6995–7002. DOI: 10.1007/s00170-021-08276-9.
[22] O. Guillon, J. Gonzalez-Julian, B. Dargatz, T. Kessel, G. Schierning, J. Räthel, M. Herrmann, Field-Assisted Sintering Technology/Spark Plasma Sintering: Mechanisms, Materials, and Technology Developments, Advanced Engineering Materials 16 (2014), 830–849. DOI: 10.1002/adem.201300409.
[23] S.-J. L. Kang, What We Should Consider for Full Densification when Sintering, Materials 13 (2020), 3578. DOI: 10.3390/ma13163578.
[24] S. Ji, Q. Gu, B. Xia, Porosity dependence of mechanical properties of solid materials, Journal of Materials Science 41 (2006), 1757–1768. DOI: 10.1007/s10853-006-2871-9.
[25] F. Martin, C. García, Y. Blanco, Influence of residual porosity on the dry and lubricated sliding wear of a powder metallurgy austenitic stainless steel, Wear 328–329 (2015), 1–7. DOI: 10.1016/j.wear.2015.01.025.
[26] A. Sinha, Z. Farhat, Effect of Surface Porosity on Tribological Properties of Sintered Pure Al and Al 6061, Materials Sciences and Applications 06 (2015), 549. DOI: 10.4236/msa.2015.66059.
[27] X. Li, U. Olofsson, A study on friction and wear reduction due to porosity in powder metallurgic gear materials, Tribology International 110 (2017), 86–95. DOI: 10.1016/j.triboint.2017.02.008.
[28] X. Peng, L. Kong, J. Y. H. Fuh, H. Wang, A Review of Post-Processing Technologies in Additive Manufacturing, Journal of Manufacturing and Materials Processing 5 (2021), 38. DOI: 10.3390/jmmp5020038.
[29] X. Chen, Z. Han, X. Li, K. Lu, Lowering coefficient of friction in Cu alloys with stable gradient nanostructures. Science advances 2.12 (2016). DOI: 10.1126/sciadv.1601942.
[30] W. L. Li, N. R. Tao, K. Lu, Fabrication of a gradient nano-micro-structured surface layer on bulk copper by means of a surface mechanical grinding treatment, Scripta Materialia 59 (2008), 546–549. DOI: 10.1016/j.scriptamat.2008.05.003.

[31] F. V. Lenel, Resistance Sintering Under Pressure, JOM 7 (1955), 158–167. DOI: 10.1007/BF03377473.
[32] N. Chawake, L. D. Pinto, A. K. Srivastav, K. Akkiraju, B. S. Murty, R. S. Kottada, On Joule heating during spark plasma sintering of metal powders, Scripta Materialia 93 (2014), 52–55. DOI: 10.1016/j.scriptamat.2014.09.003.
[33] J. R. Groza, M. Garcia, J. A. Schneider, Surface effects in field-assisted sintering, Journal of Materials Research 16 (2001), 286–292. DOI: 10.1557/JMR.2001.0043.
[34] J. R. Groza, A. Zavaliangos, Sintering activation by external electrical field, Materials Science and Engineering: A 287 (2000), 171–177. DOI: 10.1016/S0921-5093(00)00771-1.
[35] S. G. M. Carvalho, E. N. S. Muccillo, R. Muccillo, Electrical Behavior and Microstructural Features of Electric Field-Assisted and Conventionally Sintered 3 mol% Yttria-Stabilized Zirconia, Ceramics 1 (2018), 3–12. DOI: 10.3390/ceramics1010002.
[36] S. H. Chiu, T. L. Shao, C. Chen, D. J. Yao, C. Y. Hsu, Infrared microscopy of hot spots induced by Joule heating in flip-chip SnAg solder joints under accelerated electromigration, Applied Physics Letters 88 (2006), 022110. DOI: 10.1063/1.2151255.
[37] E. A. Olevsky, D. V. Dudina, Field-Assisted Sintering: Science and Applications, first ed., Springer International Publishing, Cham, 2018.
[38] E. Olevsky, I. Bogachev, A. Maximenko, Spark-plasma sintering efficiency control by inter-particle contact area growth: A viewpoint, Scripta Materialia 69 (2013), 112–116. DOI: 10.1016/j.scriptamat.2013.02.041.
[39] D. Landolt, Fundamental aspects of electropolishing, Electrochimica Acta 32 (1987), 1–11. DOI: 10.1016/0013-4686(87)87001-9.
[40] G. Yang, B. Wang, K. Tawfiq, H. Wei, S. Zhou, G. Chen, Electropolishing of surfaces: theory and applications, Surface Engineering 33 (2017), 149–166. DOI: 10.1080/02670844.2016.1198452.
[41] S. Zaki, N. Zhang, M. D. Gilchrist, Electropolishing and Shaping of Micro-Scale Metallic Features, Micromachines 13 (2022), 468. DOI: 10.3390/mi13030468.
[42] K. E. Herrera, Custom Cathode Optimization for Electropolishing Additively Manufactured 316L Stainless Steel, Master Thesis, The University of New Mexico Albuquerque, New Mexico, 2025.
[43] T. Hryniewicz, Concept of microsmoothing in the electropolishing process, Surface and Coatings Technology 64 (1994), 75–80. DOI: 10.1016/S0257-8972(09)90006-8.
[44] B. Chatterjee, Science and industry of electropolishing, Jahrb. Oberfl 71 (2015), 71–93.
[45] H. Hocheng, P. S. Pa, The application of a turning tool as the electrode in electropolishing, Journal of Materials Processing Technology 120 (2002), 6–12. DOI: 10.1016/S0924-0136(01)01061-5.
[46] M. Sun, Development of Novel Surface Finishing Processes for Additively Manufactured Metal Parts, Ph.D. Thesis, University of Waterloo, Waterloo, 2025.
[47] Y. Zhou, M. Chai, F. Yan, Z. Li, Effects of electrochemical polishing on the surface properties of laser-cut Ni–Ti alloy cardiovascular stents, International Journal of Electrochemical Science 20 (2025), 101101. DOI: 10.1016/j.ijoes.2025.101101.

[48] X. Zhao, S. Wang, L. Liu, Q. Li, J. Yu, G. Wang, C. Liang, Z. Wang, H. Hao, X. Xu, L. Zhang, Advance Chemical Mechanical Polishing Technique for Gallium Nitride Substrate, Advanced Materials Interfaces 12 (2025), 2301032. DOI: 10.1002/admi.202301032.

[49] X. Lei, Z. Zhang, H. Zhou, L. Chen, X. Deng, W. Liu, X. Zhuang, M. Wang, Y. Gu, Close atomic surface on aluminum alloy achieved by a near-neutral novel green chemical mechanical polishing method with high material removal rate, Nanoscale 17 (2025), 12684–12694. DOI: 10.1039/D5NR00132C.

[50] J. M. Steigerwald, S. P. Murarka, R. J. Gutmann, D. J. Duquette, Chemical processes in the chemical mechanical polishing of copper, Materials Chemistry and Physics 41 (1995), 217–228. DOI: 10.1016/0254-0584(95)01516-7.

[51] D. Zhao, X. Lu, Chemical mechanical polishing: Theory and experiment, Friction 1 (2013), 306–326. DOI: 10.1007/s40544-013-0035-x.

[52] U. Paik, J.-G. Park, Nanoparticle Engineering for Chemical-Mechanical Planarization: Fabrication of Next-Generation Nanodevices, first ed., Taylor & Francis, London, 2009.

[53] P. C. Brust, Surface improvement by vibratory cascade finishing process, Transactions of the North American Manufacturing Research Institute of SME (1997), 93-98.

[54] J. Domblesky, R. Evans, V. Cariapa, Material removal model for vibratory finishing, International Journal of Production Research 42 (2004), 1029–1041. DOI: 10.1080/00207540310001619641.

[55] M.-Y. Tsai, W.-Z. Yang, Combined ultrasonic vibration and chemical mechanical polishing of copper substrates, International Journal of Machine Tools and Manufacture 53 (2012), 69–76. DOI: 10.1016/j.ijmachtools.2011.09.009.

[56] H. Chen, D. Guo, G. Xie, G. Pan, Mechanical model of nanoparticles for material removal in chemical mechanical polishing process, Friction 4 (2016), 153–164. DOI: 10.1007/s40544-016-0112-z.

[57] K. Ahluwalia, R. Mediratta, S. H. Yeo, A novel approach to vibratory finishing: Double vibro-polishing, Materials and Manufacturing Processes 32 (2017), 998–1003. DOI: 10.1080/10426914.2016.1232812.

[58] R. Gohar, H. Rahnejat, Fundamentals Of Tribology, third ed., World Scientific, London, 2018.

[59] H. Czichos, Tribology and Its Many Facets: From Macroscopic to Microscopic and Nano-scale Phenomena, Meccanica 36 (2001), 605–615. DOI: 10.1023/A:1016388517893.

[60] F. P. Bowden, D. Tabor, The Friction and Lubrication of Solids, revised ed., Clarendon Press, Oxford, 2001.

[61] K.-H. Zum Gahr, Microstructure and Wear of Materials, first ed., Elsevier, Amsterdam, New York, 1987.

[62] G. Straffelini, Friction and wear, Springer Tracts in Mechanical Engineering, first ed., Cham, 2015.

[63] V. L. Popov, Verschleiß, in: V. L. Popov (Ed.), Kontaktmechanik und Reibung: Ein Lehr- und Anwendungsbuch von der Nanotribologie bis zur numerischen Simulation, Springer, Berlin, Heidelberg, 2009, pp. 263–276.

[64] K. H. Z. Gahr, Modelling of two-body abrasive wear, Wear 124 (1988), 87–103. DOI: 10.1016/0043-1648(88)90236-0.

[65] A. Zmitrowicz, Wear patterns and laws of wear – a review, Journal of Theoretical and Applied Mechanics 44 (2006), 219–253.
[66] N. P. Suh, The delamination theory of wear, Wear 25 (1973), 111–124. DOI: 10.1016/0043-1648(73)90125-7.
[67] J. R. Fleming, N. P. Suh, Mechanics of crack propagation in delamination wear, Wear 44 (1977), 39–56. DOI: 10.1016/0043-1648(77)90083-7.
[68] R. J. Wood, Tribo-corrosion of coatings: a review, Journal of Physics D: Applied Physics 40 (2007), 5502. DOI: 10.1088/0022-3727/40/18/S10.
[69] J. S. Lehmann, R. Schwaiger, M. Rinke, C. Greiner, How Tribo-Oxidation Alters the Tribological Properties of Copper and Its Oxides, Advanced Materials Interfaces 8 (2021), 2001673. DOI: 10.1002/admi.202001673.
[70] J. S. Rau, O. Schmidt, R. Schneider, R. Debastiani, C. Greiner, Three Regimes in the Tribo-Oxidation of High Purity Copper at Temperatures of up to 150 °C, Advanced Engineering Materials 24.11 (2022), 2200518. DOI: 10.1002/adem.202200518.
[71] W. Tysoe, On Stress-Induced Tribochemical Reaction Rates, Tribology Letters 65 (2017), 48. DOI: 10.1007/s11249-017-0832-x.
[72] T. F. J. Quinn, The Effect of "Hot-Spot" Temperatures on the Unlubricated Wear of Steel, A S L E Transactions 10 (1967), 158–168. DOI: 10.1080/05698196708972175.
[73] T. Katayama, D. Sekiba, K. Mukai, Y. Yamashita, F. Komori, J. Yoshinobu, Adsorption States and Dissociation Processes of Oxygen Molecules on Cu(100) at Low Temperature, The Journal of Physical Chemistry C 111 (2007), 15059–15063. DOI: 10.1021/jp0747407.
[74] J. Glascott, F. H. Stott, G. C. Wood, The effectiveness of oxides in reducing sliding wear of alloys, Oxidation of Metals 24 (1985), 99–114. DOI: 10.1007/BF00664227.
[75] J. E. Wilson, F. H. Stott, G. C. Wood, D. Tabor, The development of wear-protective oxides and their influence on sliding friction, Proceedings of the Royal Society of London. A. Mathematical and Physical Sciences 369 (1980), 557–574. DOI: 10.1098/rspa.1980.0016.
[76] S. Raumel, K. Barienti, H.-T. Luu, N. Merkert, F. Dencker, F. Nürnberger, H. J. Maier, M. C. Wurz, Characterization of the tribologically relevant cover layers formed on copper in oxygen and oxygen-free conditions, Friction 11 (2023), 1505–1521. DOI: 10.1007/s40544-022-0695-5.
[77] T. F. J. Quinn, Review of oxidational wear: Part I: The origins of oxidational wear, Tribology International 16 (1983), 257–271. DOI: 10.1016/0301-679X(83)90086-5.
[78] D. A. Rigney, X. Y. Fu, J. E. Hammerberg, B. L. Holian, M. L. Falk, Examples of structural evolution during sliding and shear of ductile materials, Scripta Materialia 49 (2003), 977–983. DOI: 10.1016/S1359-6462(03)00472-X.
[79] T. J. Rupert, C. A. Schuh, Sliding wear of nanocrystalline Ni–W: Structural evolution and the apparent breakdown of Archard scaling, Acta Materialia 58 (2010), 4137–4148. DOI: 10.1016/j.actamat.2010.04.005.
[80] A. V. Chumaevsky, D. V. Lychagin, S. Yu. Tarasov, A. Melnikov, Fragmentation, Texturing and Plastic Flow in the Subsurface of Friction-Processed Copper Single Crystal, Advanced Materials Research 872 (2013), 30–35. DOI: 10.4028/www.scientific.net/AMR.872.30.

[81] X. Chen, Z. Han, K. Lu, Wear mechanism transition dominated by subsurface recrystallization structure in Cu–Al alloys, Wear 320 (2014), 41–50. DOI: 10.1016/j.wear.2014.08.010.
[82] D. A. Rigney, J. E. Hammerberg, Unlubricated Sliding Behavior of Metals, MRS Bulletin 23 (1998), 32–36. DOI: 10.1557/S0883769400030608.
[83] X. Y. Li, K. N. Tandon, Mechanical mixing induced by sliding wear of an Al–Si alloy against M2 steel, Wear 225–229 (1999), 640–648. DOI: 10.1016/S0043-1648(99)00021-6.
[84] S. V. Prasad, C. C. Battaile, P. G. Kotula, Friction transitions in nanocrystalline nickel, Scripta Materialia 64 (2011), 729–732. DOI: 10.1016/j.scriptamat.2010.12.027.
[85] C. Greiner, Z. Liu, R. Schneider, L. Pastewka, P. Gumbsch, The origin of surface microstructure evolution in sliding friction, Scripta Materialia 153 (2018), 63–67. DOI: 10.1016/j.scriptamat.2018.04.048.
[86] D. A. Rigney, M. G. S. Naylor, R. Divakar, L. K. Ives, Low energy dislocation structures caused by sliding and by particle impact, Materials Science and Engineering 81 (1986), 409–425. DOI: 10.1016/0025-5416(86)90279-X.
[87] D. A. Hughes, N. Hansen, Graded Nanostructures Produced by Sliding and Exhibiting Universal Behavior, Physical Review Letters 87 (2001), 135503. DOI: 10.1103/PhysRevLett.87.135503.
[88] N. Argibay, M. Chandross, S. Cheng, J. R. Michael, Linking microstructural evolution and macro-scale friction behavior in metals, Journal of Materials Science 52 (2017), 2780–2799. DOI: 10.1007/s10853-016-0569-1.
[89] J. S. Dunn, W. Rosenhain, The low temperature oxidation of copper, Proceedings of the Royal Society of London. Series A, Containing Papers of a Mathematical and Physical Character 111 (1926), 210–219. DOI: 10.1098/rspa.1926.0063.
[90] J. S. Rau, S. Balachandran, R. Schneider, P. Gumbsch, B. Gault, C. Greiner, High diffusivity pathways govern massively enhanced oxidation during tribological sliding, Acta Materialia 221 (2021), 117353. DOI: 10.1016/j.actamat.2021.117353.
[91] Z. Liu, C. Patzig, S. Selle, T. Höche, P. Gumbsch, C. Greiner, Stages in the tribologically-induced oxidation of high-purity copper, Scripta Materialia 153 (2018), 114–117. DOI: 10.1016/j.scriptamat.2018.05.008.
[92] Z. Liu, Microstructure evolution under tribological loading and its elementary mechanisms, Ph.D. Thesis, Karlsruhe Institute of Technology, Karlsruhe, 2018.
[93] S.-K. Lee, H.-C. Hsu, W.-H. Tuan, Oxidation Behavior of Copper at a Temperature below 300 °C and the Methodology for Passivation, Materials Research 19 (2016), 51–56. DOI: 10.1590/1980-5373-MR-2015-0139.
[94] J. S. Rau, Mechanismen tribologisch-induzierter Oxidation in hochreinem Kupfer, Ph.D. Thesis, Karlsruhe Institute of Technology, Karlsruhe, 2021.
[95] J. Li, J. W. Mayer, E. G. Colgan, Oxidation and protection in copper and copper alloy thin films, Journal of applied physics 70 (1991), 2820–2827. DOI: 10.1063/1.349344.
[96] L. Frazer, K. B. Chang, K. R. Poeppelmeier, J. B. Ketterson, Cupric oxide inclusions in cuprous oxide crystals grown by the floating zone method, Science and Technology of Advanced Materials 16 (2015), 034901. DOI: 10.1088/1468-6996/16/3/034901.
[97] C. Gattinoni, A. Michaelides, Atomistic details of oxide surfaces and surface oxidation: the example of copper and its oxides, Surface Science Reports 70 (2015), 424–447. DOI: 10.1016/j.surfrep.2015.07.001.

[98] S. J. Kim, S. Kim, J. Lee, Y. Jo, Y.-S. Seo, M. Lee, Y. Lee, C. R. Cho, J. Kim, M. Cheon, J. Hwang, Y. I. Kim, Y.-H. Kim, Y.-M. Kim, A. Soon, M. Choi, W. S. Choi, S.-Y. Jeong, Y. H. Lee, Color of Copper/Copper Oxide, Advanced Materials 33 (2021), 2007345. DOI: 10.1002/adma.202007345.

[99] Y. Unutulmazsoy, C. Cancellieri, L. Lin, L. P. H. Jeurgens, Reduction of thermally grown single-phase CuO and Cu2O thin films by in-situ time-resolved XRD, Applied Surface Science 588 (2022), 152896. DOI: 10.1016/j.apsusc.2022.152896.

[100] H. A. Miley, Copper Oxide Films, Journal of the American Chemical Society 59 (1937), 2626–2629. DOI: 10.1021/ja01291a043.

[101] M. F. C. Ordoñez, D. L. Rodrigues, A. P. Tschiptschin, R. M. Souza, Effect of porosity on surface deformation and subsurface layer produced by scratch tests of sintered low-alloy steel, Tribology International 209 (2025), 110674. DOI: 10.1016/j.triboint.2025.110674.

[102] R. A. Al-Samarai, K. R. A. Haftirman, Y. Al-Douri, The influence of roughness on the wear and friction coefficient under dry and lubricated sliding, Int. J. Sci. Eng. Res 3.4 (2012), 1-6.

[103] K. J. Kubiak, T. W. Liskiewicz, T. G. Mathia, Surface morphology in engineering applications: Influence of roughness on sliding and wear in dry fretting, Tribology International 44 (2011), 1427–1432. DOI: 10.1016/j.triboint.2011.04.020.

[104] G. Liang, S. Schmauder, M. Lyu, Y. Schneider, C. Zhang, Y. Han, An Investigation of the Influence of Initial Roughness on the Friction and Wear Behavior of Ground Surfaces, Materials 11 (2018), 237. DOI: 10.3390/ma11020237.

[105] T. H. Fang, W. L. Li, N. R. Tao, K. Lu, Revealing extraordinary intrinsic tensile plasticity in gradient nano-grained copper, science, 331.6024 (2011), 1587-1590. DOI: 10.1126/science.1200177.

[106] ISO 80004-1:2023, Nanotechnologies - Vocabulary - Part 1: Core vocabulary, https://www.iso.org/obp/ui/en/#iso:std:iso:80004:-1:ed-1:v1:en.

[107] W. Zhao, N. Tao, J. Guo, Q. Lu, K. Lu, High density nano-scale twins in Cu induced by dynamic plastic deformation, Scripta Materialia 53 (2005), 745–749. DOI: 10.1016/j.scriptamat.2005.05.022.

[108] G. Gottstein, Physikalische Grundlagen der Materialkunde, Springer-Verlag, Berlin, Heidelberg, 1998.

[109] Z. B. Wang, K. Lu, G. Wilde, S. V. Divinski, Interfacial diffusion in Cu with a gradient nanostructured surface layer, Acta Materialia 58 (2010), 2376–2386. DOI: 10.1016/j.actamat.2009.12.024.

[110] W. Chen, Z. S. You, N. R. Tao, Z. H. Jin, L. Lu, Mechanically-induced grain coarsening in gradient nano-grained copper, Acta Materialia 125 (2017), 255–264. DOI: 10.1016/j.actamat.2016.12.006.

[111] X. Chen, R. Schneider, P. Gumbsch, C. Greiner, Microstructure evolution and deformation mechanisms during high rate and cryogenic sliding of copper, Acta Materialia 161 (2018), 138–149. DOI: 10.1016/j.actamat.2018.09.016.

[112] H. A. Padilla, B. L. Boyce, C. C. Battaile, S. V. Prasad, Frictional performance and near-surface evolution of nanocrystalline Ni–Fe as governed by contact stress and sliding velocity, Wear 297 (2013), 860–871. DOI: 10.1016/j.wear.2012.10.018.

[113] Q. Wei, S. Cheng, K. T. Ramesh, E. Ma, Effect of nanocrystalline and ultrafine grain sizes on the strain rate sensitivity and activation volume: fcc versus bcc metals,

Materials Science and Engineering: A 381 (2004), 71–79. DOI: 10.1016/j.msea.2004.03.064.
[114] C. Haug, Tribologisch induzierte Verformungsmechanismen und Reibung in Abhängigkeit von der Kristallorientierung in Kupfer, Ph.D. Thesis, Karlsruhe Institute of Technology, Karlsruhe, 2022.
[115] M. Li, S. J. Zinkle, Physical and Mechanical Properties of Copper and Copper Alloys, in: R. M. J. Konings (Ed.), Comprehensive Nuclear Materials, first ed., Elsevier, Amsterdam, 2012, Ch. 4.
[116] D. E. Baker, J. P. Senft, Kupfer, in: Schwermetalle in Böden: Analytik, Konzentration, Wechselwirkungen, B. J. Alloway (Ed.), Springer, Berlin, Heidelberg, 1999, pp. 211–239.
[117] Q. Mao, Y. Liu, Y. Zhao, A review on copper alloys with high strength and high electrical conductivity, Journal of Alloys and Compounds 990 (2024), 174456. DOI: 10.1016/j.jallcom.2024.174456.
[118] G. Zhou, Y. Qiao, Study on Heat Transfer of Copper Foam Microstructure in Phase Change Materials, Sustainability 17 (2025), 1681. DOI: 10.3390/su17041681.
[119] Y. Xu, G. Zhao, Q. Wang, Y. Zhan, B. Chen, Study on material removal mechanism of sapphire wafer with CeO2 coated diamond composite abrasives via green polishing, Journal of Manufacturing Processes 92 (2023), 412–421. DOI: 10.1016/j.jmapro.2023.02.062.
[120] W. K. Kim, D. Xi, B. H. Kim, Nanoscale indentation and scratching tests of single crystal sapphire using molecular dynamics simulation, Computational Materials Science 170 (2019), 109195. DOI: 10.1016/j.commatsci.2019.109195.
[121] I. Platzman, R. Brener, H. Haick, R. Tannenbaum, Oxidation of Polycrystalline Copper Thin Films at Ambient Conditions, The Journal of Physical Chemistry C 112 (2008), 1101–1108.
[122] R. Lung, K. G. Schell, C. Greiner, Porosity Matters: Exploring its Impact on the Unlubricated Tribological Behavior of Copper, under consideration (2025). DOI: 10.35097/q9q7nbnb7ggazf4m.
[123] T. E. Fischer, Z. Zhu, H. Kim, D. S. Shin, Genesis and role of wear debris in sliding wear of ceramics, Wear 245 (2000), 53–60. DOI: 10.1016/S0043-1648(00)00465-8.
[124] R. S. Gates, M. Hsu, E. E. Klaus, Tribochemical Mechanism of Alumina With Water, Tribology Transactions 32 (1989), 357–363. DOI: 10.1080/10402008908981900.
[125] S. J. Bull, N. Moharrami, S. V. Hainsworth, T. F. Page, The origins of chemomechanical effects in the low-load indentation hardness and tribology of ceramic materials, Journal of Materials Science 51 (2016), 107–125. DOI: 10.1007/s10853-015-9412-3.
[126] E. Macherauch, H.-W. Zoch, V11 Korngrößenermittlung, in: Praktikum in Werkstoffkunde: 95 ausführliche Versuche aus wichtigen Gebieten der Werkstofftechnik, E. Macherauch, H.-W. Zoch (Eds.), Springer Fachmedien, Wiesbaden, 2014, pp. 93–100.
[127] W. F. Koch, R. S. Davis, V. E. Bower, Direct Determination of Air Density in a Balance Through Artifacts Characterized in an Evacuated Weighing Chamber., Journal of Research of the National Bureau of Standards 83 (1978), 407–413. DOI: 10.6028/jres.083.026.

[128] ISO 15212-1:1998, Oscillation-type density meters - Part 1: Laboratory instruments, https://www.mt.com/de/de/home/library/operating-instructions/laboratory-weighing/NC_density_OI.html (accessed 2025-09-30).
[129] N. A. Lange, Lange's Handbook of Chemistry, J. A. Dean (Ed.), 15. ed., McGraw-Hill handbooks, New York, 1999.
[130] R. Hielscher, H. Schaeben, A novel pole figure inversion method: specification of the MTEX algorithm, Journal of Applied Crystallography 41 (2008), 1024–1037. DOI: 10.1107/S0021889808030112.
[131] ISO 21920-2:2022, Geometrical product specifications (GPS) - Surface texture: Profile - Part 2: Terms, definitions and surface texture parameters, https://www.nautos.de/OJG/search/item-detail/DE30091970 (accessed 2025-08-18).
[132] ISO 4288:1996, Geometrical Product Specifications (GPS) - Surface texture: Profile method - Rules and procedures for the assessment of surface texture, https://www.nautos.de/OJG/search/item-detail/DE19015460 (accessed 2025-08-18).
[133] ISO 25178-2:2021, Geometrical product specifications (GPS) - Surface texture: Areal - Part 2: Terms, definitions and surface texture parameters, https://www.iso.org/obp/ui/#iso:std:iso:25178:-2:ed-2:v1:en (accessed 2025-08-18).
[134] D.-C. Serbanoiu, A.-C. Vartolomei, D.-V. Ghiga, S. I. Pop, I. Panainte, M. Moldovan, C. Sarosi, I. Petean, M.-J. Boileau, M. Pacurar, Comparative Evaluation of Dental Enamel Microhardness Following Various Methods of Interproximal Reduction: A Vickers Hardness Tester Investigation, Biomedicines 12 (2024), 1132. DOI: 10.3390/biomedicines12051132.
[135] R. Lung, K. G. Schell, C. Greiner, How Surface Treatment of Porous Copper Samples Dictates Dry Friction and Wear, Materials & Design (2025), 114584. DOI: 10.1016/j.matdes.2025.114584.
[136] I. Green, Poisson Ratio Effects and Critical Values in Spherical and Cylindrical Hertzian Contacts, Applied Mechanics and Engineering 10.3 (2005), 451–462.
[137] A. Karambakhsh, A. Afshar, P. Malekinejad, Corrosion Resistance and Color Properties of Anodized Ti-6Al-4V, Journal of Materials Engineering and Performance 21 (2012), 121–127. DOI: 10.1007/s11665-010-9791-1.
[138] V. Popov, Das Coulombsche Reibungsgesetz, in: V. L. Popov (Ed.), Kontaktmechanik und Reibung: Von der Nanotribologie bis zur Erdbebendynamik, Springer, Berlin, Heidelberg, 2010, pp. 137–159.
[139] W. Chen, Z. S. You, N. R. Tao, Z. H. Jin, L. Lu, Mechanically-induced grain coarsening in gradient nano-grained copper, Acta Materialia 125 (2017), 255–264. DOI: 10.1016/j.actamat.2016.12.006.
[140] Y. Li, A. J. Bushby, D. J. Dunstan, The Hall–Petch effect as a manifestation of the general size effect, Proceedings of the Royal Society A: Mathematical, Physical and Engineering Sciences 472 (2016), 20150890. DOI: 10.1098/rspa.2015.0890.
[141] S. N. Naik, S. M. Walley, The Hall–Petch and inverse Hall–Petch relations and the hardness of nanocrystalline metals, Journal of Materials Science 55 (2020), 2661–2681. DOI: 10.1007/s10853-019-04160-w.
[142] G. M. Hamilton, Explicit Equations for the Stresses beneath a Sliding Spherical Contact, Proceedings of the Institution of Mechanical Engineers, Part C: Journal of Mechanical Engineering Science 197 (1983), 53–59. DOI: 10.1243/PIME_PROC_1983_197_076_02.

[143] C. Greiner, J. Gagel, P. Gumbsch, Solids Under Extreme Shear: Friction-Mediated Subsurface Structural Transformations, Advanced Materials 31 (2019), 1806705. DOI: 10.1002/adma.201806705.
[144] D. Shakhvorostov, K. Pöhlmann, M. Scherge, Structure and mechanical properties of tribologically induced nanolayers, Wear 260 (2006), 433–437. DOI: 10.1016/j.wear.2005.02.086.
[145] R. Mishra, B. Basu, R. Balasubramaniam, Effect of grain size on the tribological behavior of nanocrystalline nickel, Materials Science and Engineering: A 373 (2004), 370–373. DOI: 10.1016/j.msea.2003.09.107.
[146] S. Prasad, J. Michael, C. Battaile, B. Majumdar, On the Evolution of Friction-Induced Microstructures in Single Crystal Nickel, Microscopy and Microanalysis 14 (2008), 906–907. DOI: 10.1017/S1431927608083852.
[147] M. Chandross, N. Argibay, Friction of Metals: A Review of Microstructural Evolution and Nanoscale Phenomena in Shearing Contacts, Tribology Letters 69 (2021), 119. DOI: 10.1007/s11249-021-01477-z.
[148] P. A. Romero, T. T. Järvi, N. Beckmann, M. Mrovec, M. Moseler, Coarse Graining and Localized Plasticity between Sliding Nanocrystalline Metals, Physical Review Letters 113 (2014), 036101. DOI: 10.1103/PhysRevLett.113.036101.
[149] M. Shafiei, A. T. Alpas, Friction and Wear Mechanisms of Nanocrystalline Nickel in Ambient and Inert Atmospheres, Metallurgical and Materials Transactions A 38 (2007), 1621–1631. DOI: 10.1007/s11661-007-9157-y.
[150] S. Karthikeyan, H. J. Kim, D. A. Rigney, Velocity and Strain-Rate Profiles in Materials Subjected to Unlubricated Sliding, Physical Review Letters 95 (2005), 106001. DOI: 10.1103/PhysRevLett.95.106001.
[151] Y. Wei, A. F. Bower, H. Gao, Enhanced strain-rate sensitivity in fcc nanocrystals due to grain-boundary diffusion and sliding, Acta Materialia 56 (2008), 1741–1752. DOI: 10.1016/j.actamat.2007.12.028.
[152] D. S. Gianola, D. H. Warner, J. F. Molinari, K. J. Hemker, Increased strain rate sensitivity due to stress-coupled grain growth in nanocrystalline Al, Scripta Materialia 55 (2006), 649–652. DOI: 10.1016/j.scriptamat.2006.06.002.
[153] N. Argibay, M. Chandross, S. Cheng, J. R. Michael, Linking microstructural evolution and macro-scale friction behavior in metals, Journal of Materials Science 52 (2017), 2780–2799. DOI: 10.1007/s10853-016-0569-1.
[154] Z. Jiang, X. Liu, G. Li, Q. Jiang, J. Lian, Strain rate sensitivity of a nanocrystalline Cu synthesized by electric brush plating, Applied Physics Letters 88 (2006), 143115. DOI: 10.1063/1.2193467.
[155] H. M. Hering: Tribologische Eigenschaften nanoskaliger Kupfergefüge, Master Thesis, Karlsruhe Institute of Technology, Karlsruhe, 2025.
[156] K. Janerka, J. Jezierski, M. Stawarz, J. Szajnar, Method for Resistivity Measurement of Grainy Carbon and Graphite Materials, Materials 12 (2019), 648. DOI: 10.3390/ma12040648.
[157] R. A. Matula, Electrical resistivity of copper, gold, palladium, and silver, Journal of Physical and Chemical Reference Data 8 (1979), 1147–1298. DOI: 10.1063/1.555614.
[158] T. F. J. Quinn, Review of oxidational wear: Part I: The origins of oxidational wear, Tribology International 16.5 (1983), 257-271. DOI: 10.1016/0301-679X(83)90086-5.

[159] A. N. Stroh, The formation of cracks in plastic flow. II, Proceedings of the Royal Society of London. A. Mathematical and Physical Sciences 232 (1955), 548–560. DOI: 10.1098/rspa.1955.0238.
[160] A. T. Alpas, H. Hu, J. Zhang, Plastic deformation and damage accumulation below the worn surfaces, Wear 162–164 (1993), 188–195. DOI: 10.1016/0043-1648(93)90500-L.
[161] D. M. Bailey, R. S. Sayles, Effect of Roughness and Sliding Friction on Contact Stresses, Journal of Tribology 113 (1991), 729–738. DOI: 10.1115/1.2920686.
[162] P. J. James, Particle Deformation During Cold Isostatic Pressing of Metal Powders, Powder Metallurgy 20 (1977), 199–204. DOI: 10.1179/pom.1977.20.4.199.
[163] C. G. Ribbing, A. Roos, Copper Oxides (Cu2O, CuO), in: Handbook of Optical Constants of Solids, E. D. Palik (Ed.), first ed., Academic Press, Burlington, 1997, pp. 875–882.
[164] H. M. Cao, X. Zhou, X. Y. Li, K. Lu, Friction mechanism in the running-in stage of copper: From plastic deformation to delamination and oxidation, Tribology International 115 (2017), 3–7. DOI: 10.1016/j.triboint.2017.05.027.
[165] A. Buch, S. Goldschmidt, Influence of porosity on elastic moduli of sintered materials, Materials Science and Engineering 5 (1970), 111–118. DOI: 10.1016/0025-5416(70)90040-6.
[166] H. M. Ledbetter, E. R. Naimon, Elastic Properties of Metals and Alloys. II. Copper, Journal of Physical and Chemical Reference Data 3 (1974), 897–935. DOI: 10.1063/1.3253150.
[167] J. Musil, F. Kunc, H. Zeman, H. Poláková, Relationships between hardness, Young's modulus and elastic recovery in hard nanocomposite coatings, Surface and Coatings Technology 154 (2002), 304–313. DOI: 10.1016/S0257-8972(01)01714-5.
[168] E. R. Dobrovinskaya, L. A. Lytvynov, V. Pishchik, Properties of Sapphire, in: Sapphire; Springer US, Boston, MA, 2009, pp 55–176.
[169] K. Komvopoulos, D.-H. Choi, Elastic Finite Element Analysis of Multi-Asperity Contacts, Journal of Tribology 114 (1992), 823–831. DOI: 10.1115/1.2920955.
[170] A. Dollmann, A. Kauffmann, M. Heilmaier, C. Haug, C. Greiner, Microstructural changes in CoCrFeMnNi under mild tribological load, Journal of Materials Science 55 (2020), 12353–12372. DOI: 10.1007/s10853-020-04806-0.
[171] D. Kuhlmann-Wilsdorf, Flash temperatures due to friction and Joule heat at asperity contacts, Wear 105 (1985), 187–198. DOI: 10.1016/0043-1648(85)90067-5.
[172] B. Yao, Z. Han, Y. S. Li, N. R. Tao, K. Lu, Dry sliding tribological properties of nanostructured copper subjected to dynamic plastic deformation, Wear 271 (2011), 1609–1616. DOI: 10.1016/j.wear.2010.12.020.
[173] A. J. Perez-Unzueta, J. H. Beynon, M. G. Gee, Effects of surrounding atmosphere on the wear of sintered alumina, Wear 146 (1991), 179–196. DOI: 10.1016/0043-1648(91)90233-K.
[174] M. G. Gee, N. M. Jennett, High resolution characterisation of tribochemical films on alumina, Wear 193 (1996), 133–145. DOI: 10.1016/0043-1648(95)06612-8.
[175] H. T. Angus, The significance of hardness, Wear 54.1 (1979), 33–78. DOI: 10.1016/0043-1648(79)90046-2.

[176] A. V. Fedotov, A. V. Gvozdev, A. V. Dunaev, I. A. Pekhalsky, The use of boehmite in tribology, IOP Conference Series: Materials Science and Engineering 996 (2020), 012012. DOI: 10.1088/1757-899X/996/1/012012.
[177] F. J. Wilkins, E. K. Rideal, T. M. Lowry, The kinetics of the oxidation of copper. Part I. -The initial oxidation of copper at low pressures, Proceedings of the Royal Society of London. Series A, Containing Papers of a Mathematical and Physical Character 128 (1930), 394–406. DOI: 10.1098/rspa.1930.0117.
[178] S. Lafaye, C. Gauthier, R. Schirrer, The ploughing friction: analytical model with elastic recovery for a conical tip with a blunted spherical extremity, Tribology Letters 21 (2006), 95–99. DOI: 10.1007/s11249-006-9018-7.
[179] F. P. Bowden, D. Tabor, Friction, lubrication and wear: a survey of work during the last decade, British Journal of Applied Physics 17 (1966), 1521. DOI: 10.1088/0508-3443/17/12/301.
[180] F. P. Bowden, A. J. W. Moore, D. Tabor, The Ploughing and Adhesion of Sliding Metals, Journal of Applied Physics 14 (1943), 80–91. DOI: 10.1063/1.1714954.
[181] P. A. Korzhavyi, B. Johansson, Literature review on the properties of cuprous oxide Cu2O and the process of copper oxidation, technical report SKB, 2011, https://skb.se/upload/publications/pdf/TR-11-08.pdf (accessed 2025-08-18).
[182] M. Spreckels, Einfluss der Temperaturverteilung auf das tribologische Verhalten von Synchronisierungen, Ph.D. Thesis, University Hannover, Hannover, 2001.
[183] A. R. Savkoor, Models of Friction, in: J. Lemaitre (Ed.), Handbook of Materials Behavior Models, first ed., Academic Press, Sand Diego, 2001, Ch. 8.3.
[184] S. Ciraci, A. Buldum, Atomic-scale study of friction and energy dissipation, Wear 254 (2003), 911–916. DOI: 10.1016/S0043-1648(03)00246-1.
[185] A. L. Zharin, E. I. Fishbejn, N. A. Shipitsa, Effect of contact deformation upon surface electron work function, Journal of Friction and Wear 16.3 (1995), 66-78.
[186] Li, Y. Investigation of the relationship between the electron work function (EWF), adhesion and friction, Ph.D. Thesis, University of Alberta, Alberta, 2008.
[187] L. C. Pauling, A resonating-valence-bond theory of metals and intermetallic compounds, Proceedings of the Royal Society of London. Series A. Mathematical and Physical Sciences 196 (1949), 343–362. DOI: 10.1098/rspa.1949.0032.
[188] K. Miyoshi, D. H. Buckley, Adhesion and friction of transition metals in contact with non-metallic hard materials, Wear 77 (1982), 253–264. DOI: 10.1016/0043-1648(82)90109-0.
[189] D. H. Buckley, K. Miyoshi, Friction and wear of ceramics, Wear 100 (1984), 333–353. DOI: 10.1016/0043-1648(84)90020-6.
[190] K. Miyoshi, D. H. Buckley, Friction and wear of single-crystal manganese-zinc ferrite, Wear 66 (1981), 157–173. DOI: 10.1016/0043-1648(81)90111-3.
[191] G. T. Beilby, Aggregation and Flow of Solids: Being the Records of an Experimental Study of the Micro-structure and Physical Properties of Solids in Various States of Aggregation, 1900-1921, first ed., Macmillan and Company, London, 1921.
[192] T. P. Hoar, J. A. S. Mowat, Mechanism of Electropolishing, Nature 165 (1950), 64–65. DOI: 10.1038/165064a0.
[193] M. Fellah, N. Hezil, D. Bouras, A. Obrosov, A. S. Mohammed, A. Montagne, A. Abd-Elmonem, S. M El Din, S. Weiß, Structural, mechanical and tribological performance of a nano structured biomaterial Co–Cr–Mo alloy synthesized via mechanical alloying,

Journal of Materials Research and Technology 25 (2023), 2152–2165. DOI: 10.1016/j.jmrt.2023.06.031.
[194] A. Charvátová Campbell, V. Buršíková, J. Martinek, P. Klapetek, Modeling the influence of roughness on nanoindentation data using finite element analysis, International Journal of Mechanical Sciences 161–162 (2019), 105015. DOI: 10.1016/j.ijmecsci.2019.105015.
[195] V. L. Popov, Rigorose Behandlung des Kontaktproblems – Hertzscher Kontakt, in: V. L. Popov (Ed.), Kontaktmechanik und Reibung: Von der Nanotribologie bis zur Erdbebendynamik, Springer, Berlin, Heidelberg, 2010, pp. 59–74.
[196] J. J. D. León, D. M. Fryauf, R. D. Cormia, N. P. Kobayashi, Study of the formation of native oxide on copper at room temperature, Low-Dimensional Materials and Devices 2016, 9924 (2016), 63–69. DOI: 10.1117/12.2238745.
[197] D. Hull, D. J. Bacon, Strength of Crystalline Solids, in: D. Hull, D. J. Bacon (Eds.), Introduction to Dislocations, fifth ed., Butterworth-Heinemann, Oxford, 2011, Ch. 10.
[198] H. Magnusson, K. Frisk, Self-diffusion and impurity diffusion of hydrogen, oxygen, sulphur and phosphorus in copper, technical report SKB, 2013. https://www.skb.se/publication/2477839/TR-13-24.pdf (accessed 2025-08-18).
[199] A. Ponomarenko, D. Quéré, C. Clanet, A universal law for capillary rise in corners, Journal of Fluid Mechanics 666 (2011), 146–154. DOI: 10.1017/S0022112010005276.
[200] Wm. H. Ross, R. M. Jones, C. B. Durgin, The Purification of Phosphoric Acid by Crystallization., Industrial & Engineering Chemistry 17 (1925), 1081–1083. DOI: 10.1021/ie50190a031.
[201] M. M. S. H. Tang, Purification of phosphoric acid by melt crystallization, Ph.D. Thesis, Martin-Luther-Universität Halle-Wittenberg, Halle, 1988.
[202] H. R. Corti, F. J. Nores-Pondal, C. Austen Angell, Heat capacity and glass transition in P2O5–H2O solutions: support for Mishima's conjecture on solvent water at low temperature, Physical Chemistry Chemical Physics 13 (2011), 19741–19748. DOI: 10.1039/c1cp22185j.
[203] Z. Bakher, M. Kaddami, Liquid–Liquid–Solid Equilibria in the Ternary System Water–Phosphoric Acid–Cyclohexane at 25 and 35 °C: Stability Domain of Hemihydrate and Anhydrous Phosphoric Acid, Journal of Chemical & Engineering Data 64 (2019), 161–168. DOI: 10.1021/acs.jced.8b00666.
[204] B. M. H. Gorenflo, Plastic deformation of copper under variable tribological load, Master Thesis, Karlsruhe Institute of Technology, Karlsruhe, 2021.
[205] M. L. Flachmann, Copper tribology under a variety of loading conditions and oxidation regimes: the case for efficient analysis via FAIR data, Master Thesis, Karlsruhe Institute of Technology, Karlsruhe, 2023.
[206] B. X. Beichert, Initiierung der Kristallrotation unter tribologischer Last, Master Thesis, Karlsruhe Institute of Technology, Karlsruhe, 2024.

A Appendix

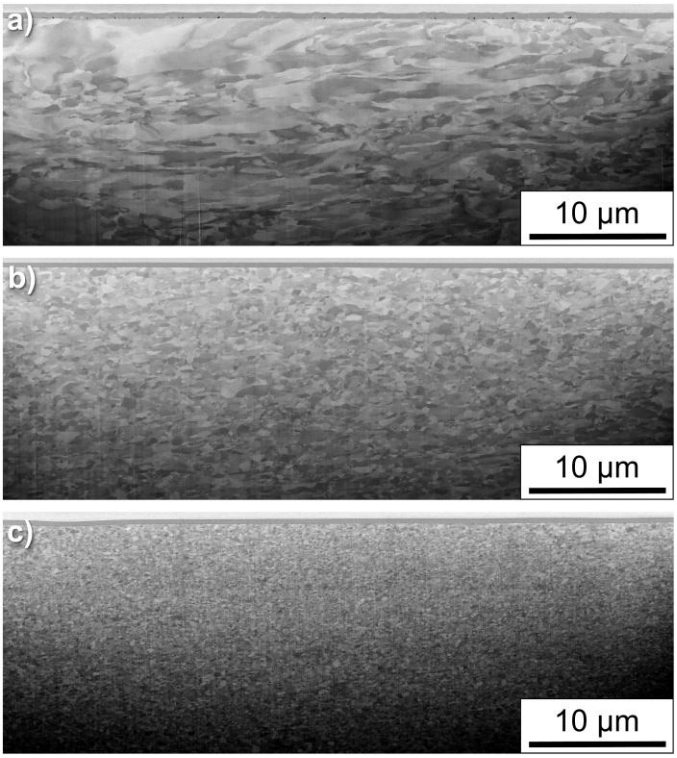

Figure A.1: SEM cross-sectional images of the electropolished surfaces of a) GNG1-60, b) GNG2-160, and c) GNG2-10 prior to tribological experiments. The value following the hyphen in the specimen's name represents the amount of surface removal after SMGT.

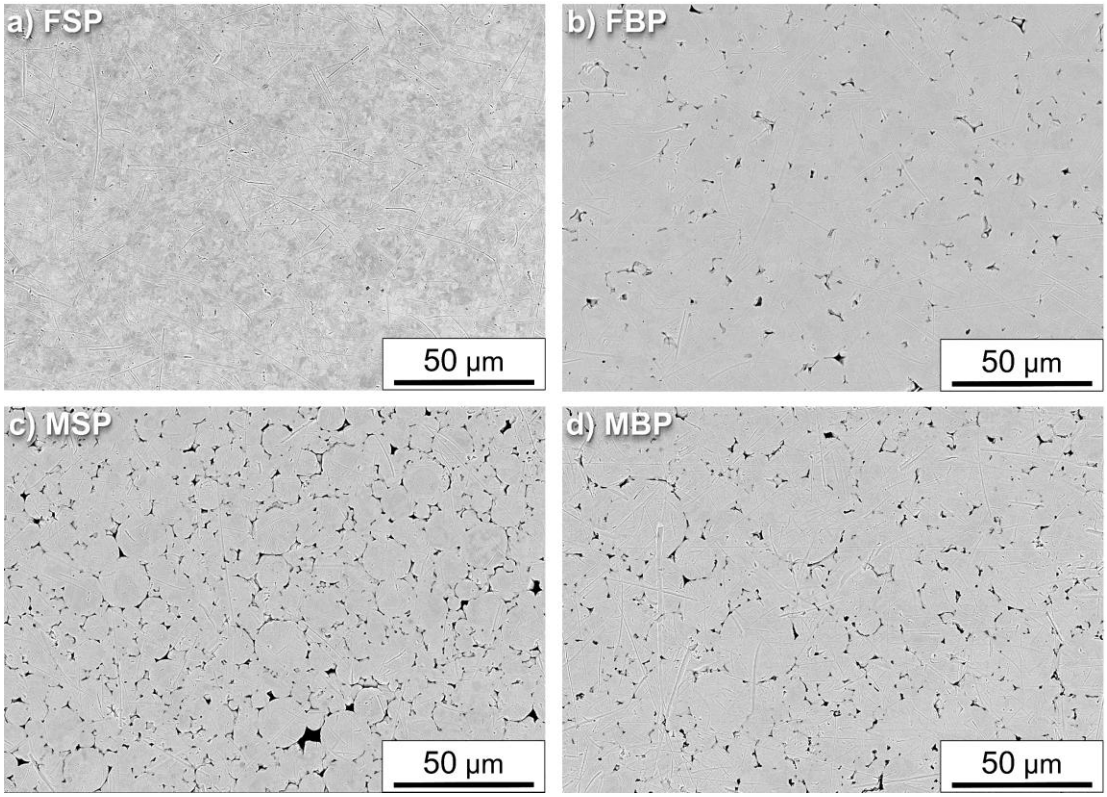

Figure A.2: SEM images of the vibropolished surfaces of the samples with a) few small pores (FSP), b) few big pores (FBP), c) many small pores (MSP), and d) many big pores (MBP) [122].

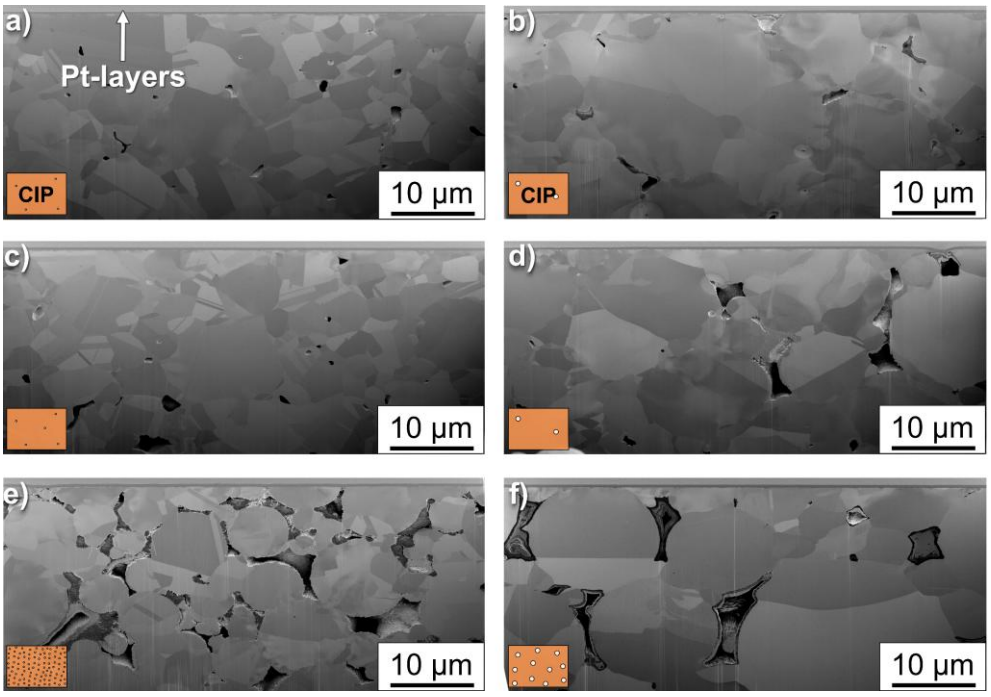

Figure A.3: SEM cross-sectional images of a) FSPC, b) FBPC, c) FSP, d) FBP, e) MSP, and f) MBP microstructures [122]. Variations in pore size and number, along with whether the specimen was additionally cold isostatically pressed (CIP), are indicated by the symbols.

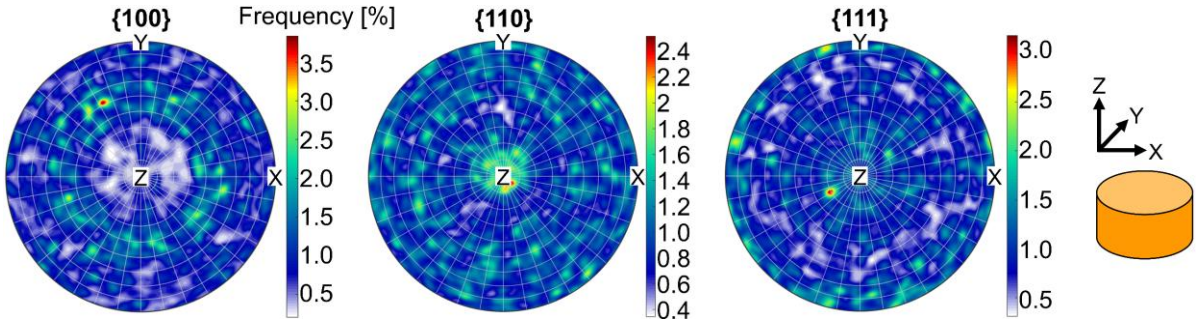

Figure A.4: Orientation distribution functions derived from pole figures, showing the frequency of surface grain orientations for specimen with few big pores in the {100}, {110}, and {111} crystal orientations, with the X and Y directions lying within the specimen surface plane, and the Z direction oriented perpendicular to it [122].

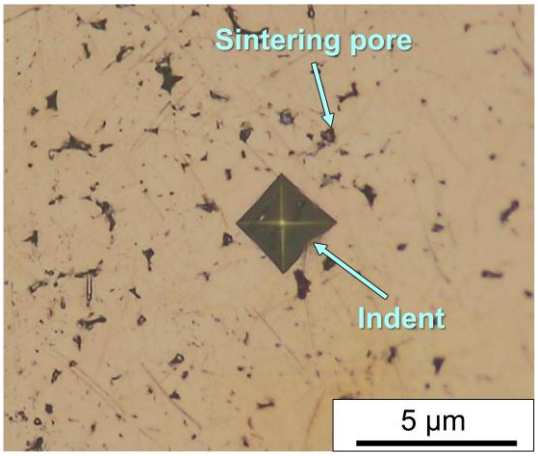

Figure A.5: Light microscopy image of the vibropolished specimen surface with few big pores showing the indent from a microhardness measurement.

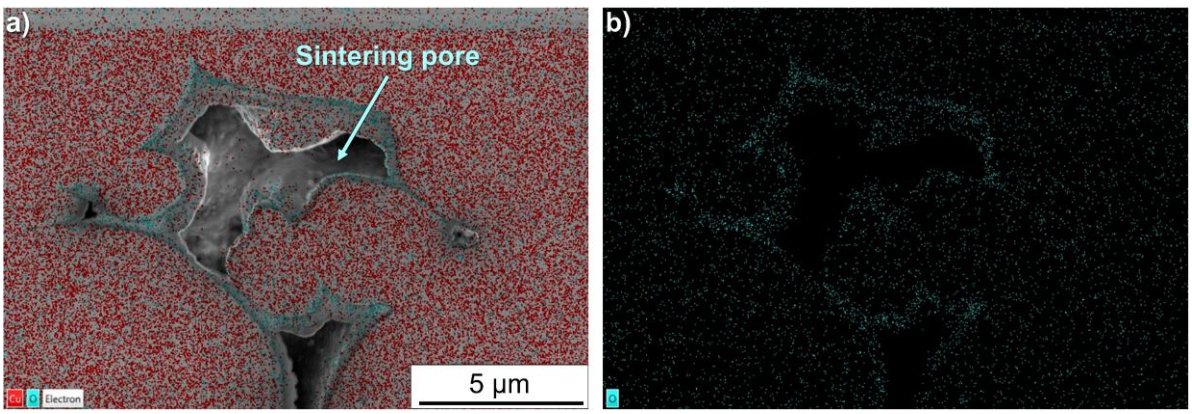

Figure A.6: EDS mapping at an accelerating voltage of 2 kV of a sample with many big pores beneath the surface of sintered copper particles and a sintering pore, where a) shows the SEM image along with the distribution of copper and oxygen, and b) shows only the oxygen distribution.

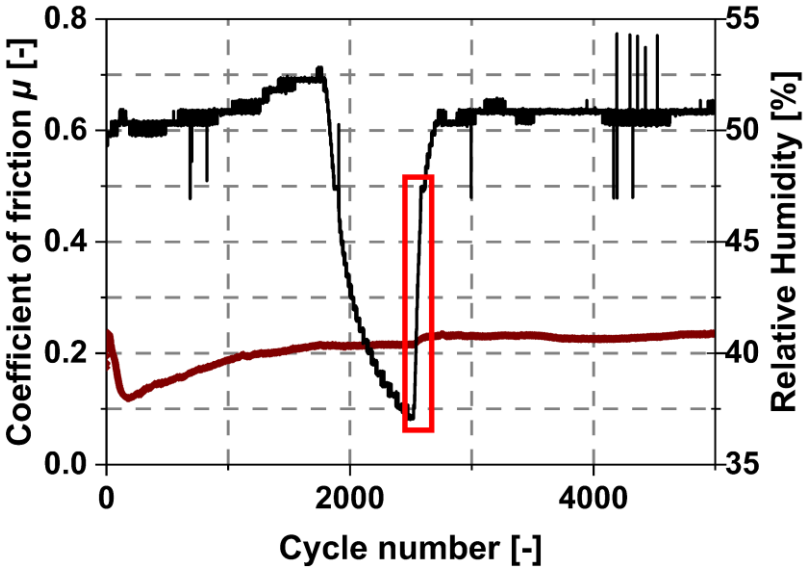

Figure A.7: Increase in the coefficient of friction of sample with many small pores after approximately 2500 cycles due to an increase in relative humidity [135]. The corresponding area is highlighted by a red rectangle.

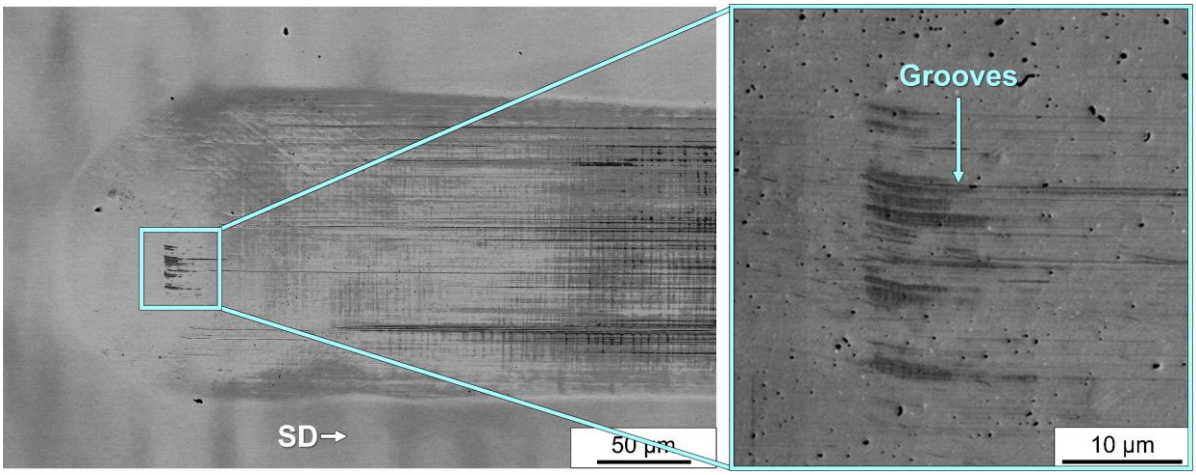

Figure A.8: SEM image of the initial part of a single trace wear track on single-crystal copper, just after the indent, showing grooves parallel to the sliding direction (SD), adapted from Beichert [206].

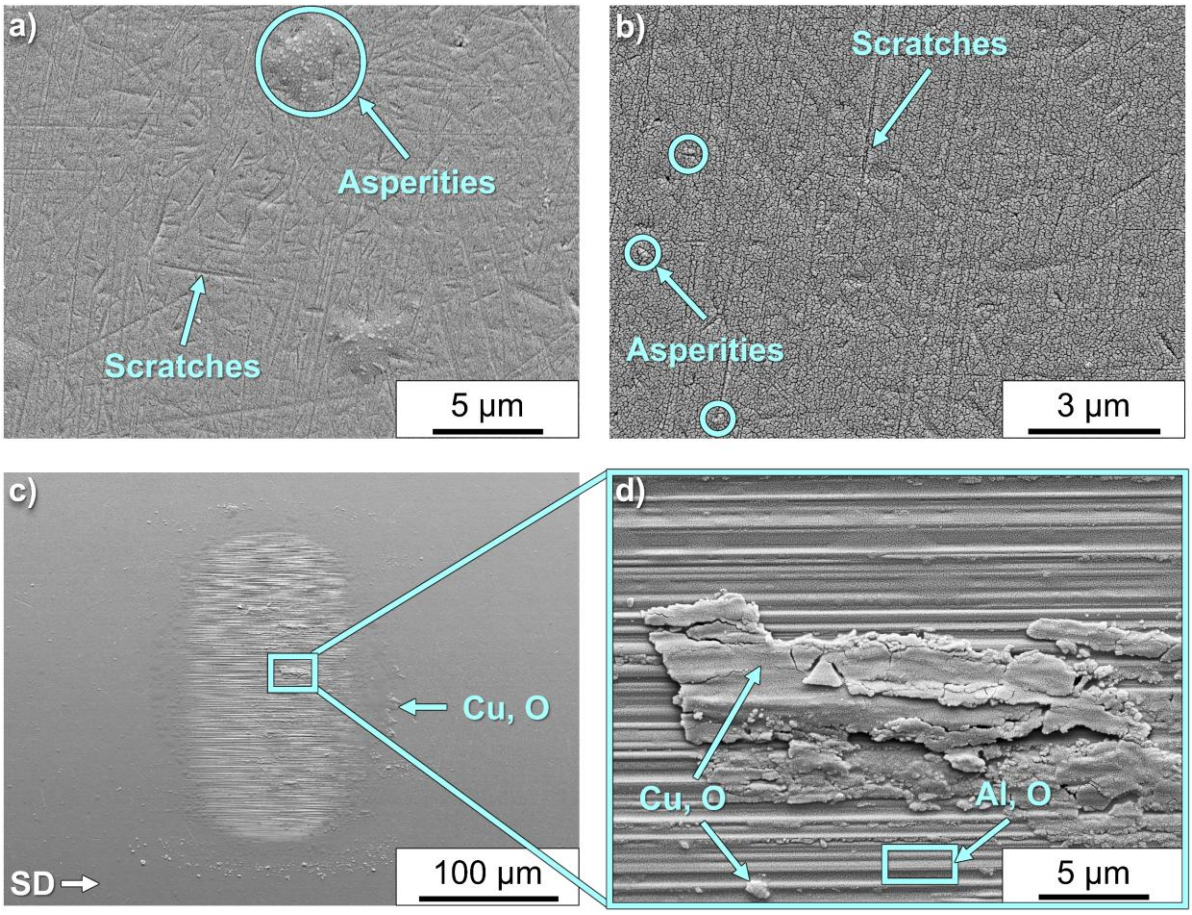

Figure A.9: SE images of a sapphire sphere in a) and b) and of its wear track after 1000 cycles in sliding direction (SD) on a sample with few small pores in c) and d) (adapted from [122]). EDS analysis at the indicated positions provide the local elemental composition. The sphere surface was sputtered with a thin gold layer prior to imaging, which is apparent in b) from the small cracks. The exemplarily marked asperities and scratches are features of the sphere.

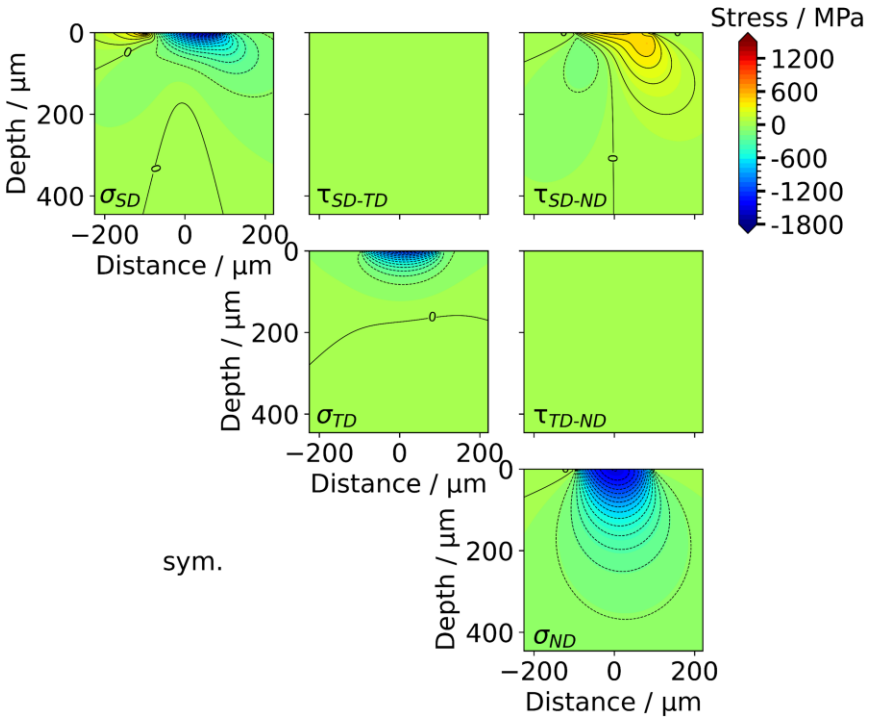

Figure A.10: Stress tensor of the stress field according to Hamilton, calculated using a normal force of 30 N, the elastic constants of copper and WC-Co as the counterbody, and a coefficient of friction of 0.37, as observed for GNG-0(Chen) over 6000 sliding cycles. Continuous lines indicate positive stress, dashed ones represent negative stress, both in increments of 100 MPa.

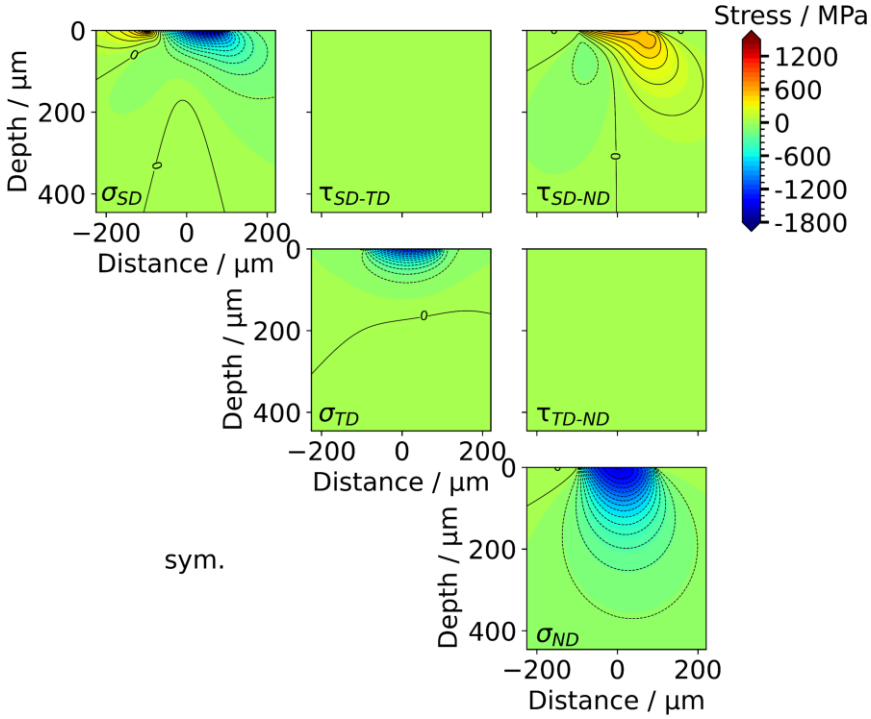

Figure A.11: Stress tensor of the Hamilton stress field, calculated for a normal force of 30 N, using the elastic constants of copper and WC-Co as the counterbody, and a coefficient of friction of 0.50, representing the state of GNG-30(Chen) and GNG1-60 after 6000 sliding cycles. Continuous lines indicate positive stress, dashed ones represent negative stress, both in increments of 100 MPa.

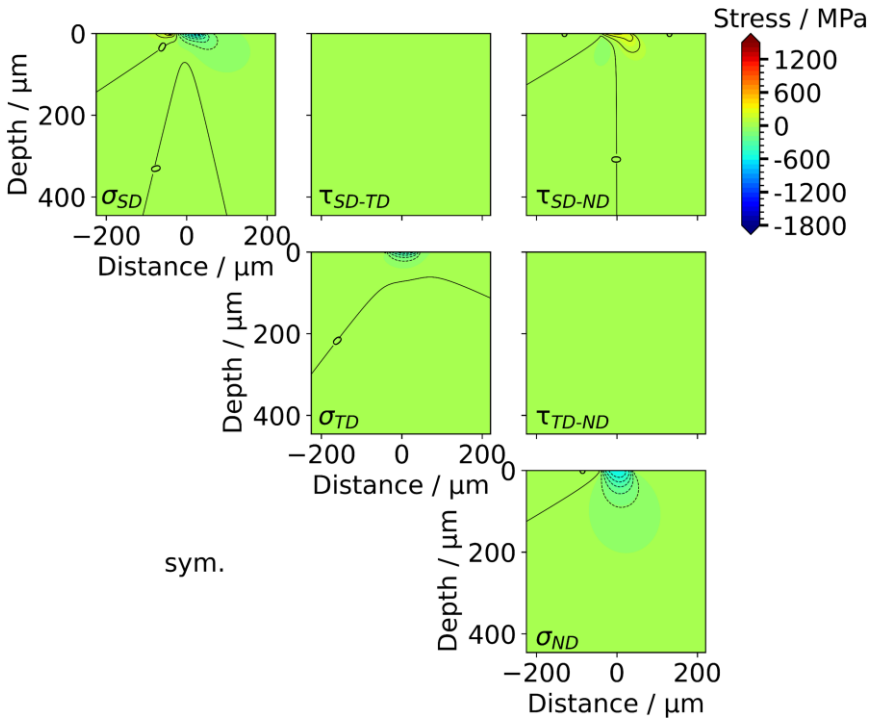

Figure A.12: Stress tensor of the Hamilton stress field, calculated for a normal force of 2 N, using the elastic constants of copper and sapphire as the counterbody, and a coefficient of friction of 0.57, as observed for GNG2-160 and GNG2-10 after 1000 sliding cycles. Continuous lines indicate positive stress, dashed ones represent negative stress, both in increments of 100 MPa.

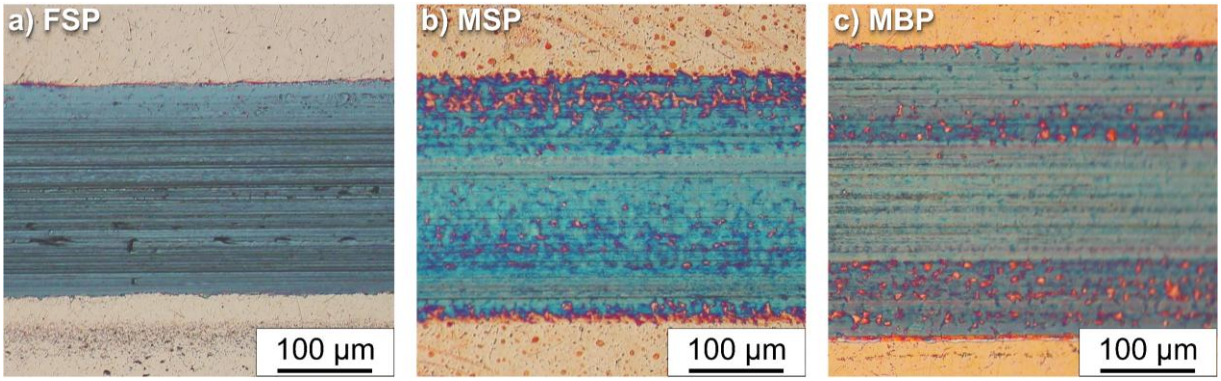

Figure A.13: Light microscope images of the wear tracks of a) few small pores (FSP), b) many small pores (MSP), and c) many big pores (MBP) after 5000 cycles (adapted from [135]).

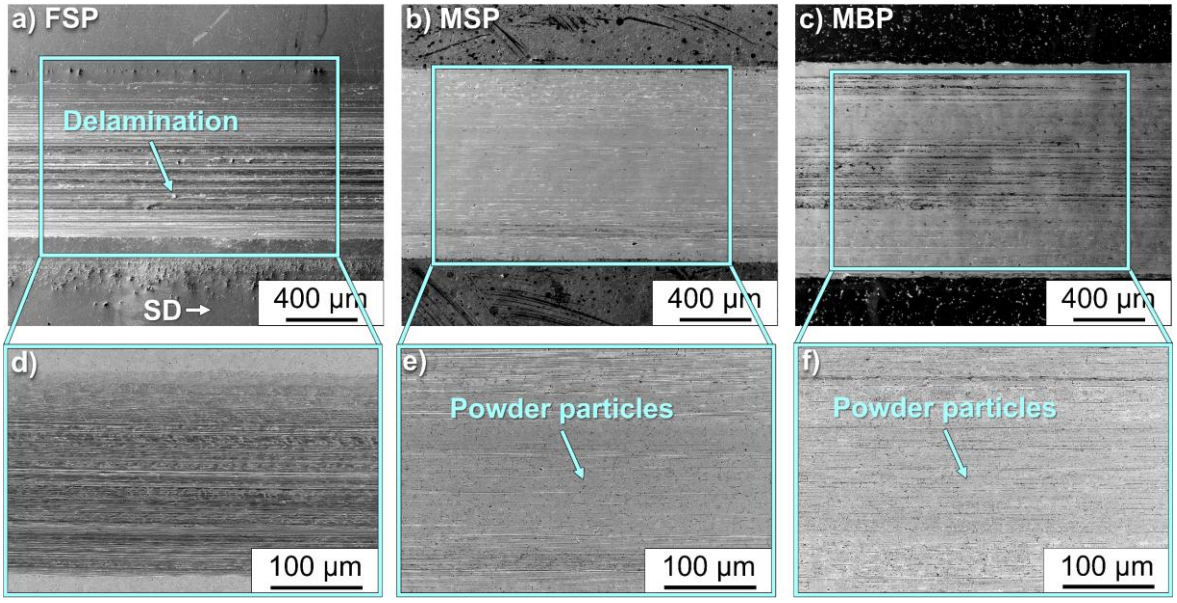

Figure A.14: SE images of the wear tracks of a) few small pores (FSP), b) many small pores (MSP), c) many big pores (MBP), and BSE images of d) FSP, e) MSP, and f) MBP after 5000 cycles (adapted from [135]). The sliding direction (SD) in a) applies to all images.

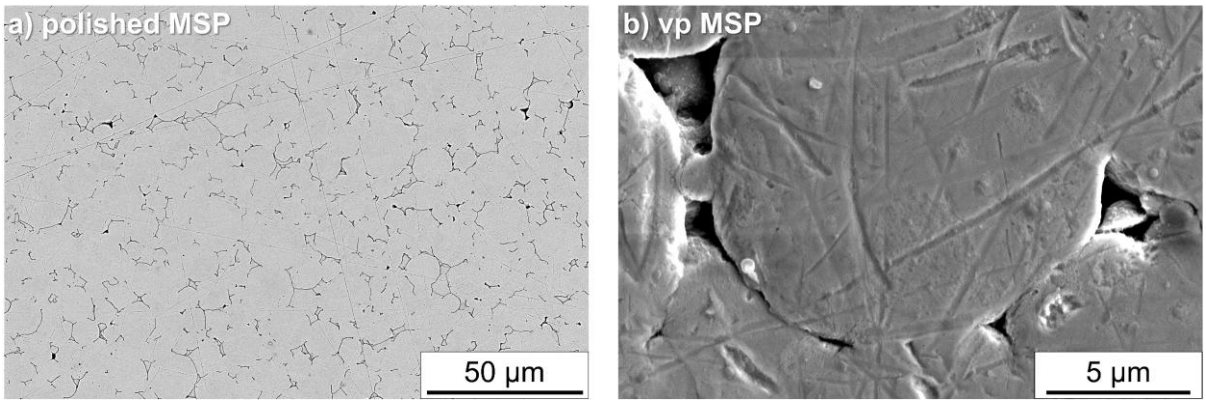

Figure A.15: SEM images of the sample surface with many small pores: a) after being polished to 1 µm (BSE image), showing smeared sintering pores, and b) after being vibropolished (SE image), with small particles in the sintering pores (adapted from [135]).